Fabrication and characterization of periodically-poled KTP and Rb-doped KTP for applications in the visible and UV

Shunhua Wang

Doctoral Thesis

Laser Physics Division, Department of Physics
Royal Institute of Technology
Stockholm, Sweden 2005

Laser Physics Division, Department of Physics
Royal Institute of Technology
Albanova
Roslagstullsbacken 21
SE-106 91 Stockholm, Sweden

Akademisk avhandling som med tillstånd Kungliga Tekniska Högskolan framlägges till offentlig granskning för avläggande av teknisk doktorsexamen i fysik, fredagen den 25 november 2005, kl 10 sal FB53, Albanova, Roslagstullsbacken 21, Stockholm. Avhandling kommer att försvaras på engelska.

TRITA-FYS 2005:50
ISSN 0280-316X
ISRN KTH/FYS/--05:50--SE

ISBN 91-7178-153-6

Cover picture: Chemical selective etching of a PPKTP on original c^- face of a KTP

Fabrication and characterization of periodically-poled KTP and Rb-doped KTP for
applications in the visible and UV

To Daniel and Zhenlei

Shunhua Wang
Fabrication and characterization of periodically-poled KTP and Rb-doped KTP for applications in the visible and UV
Laser Physics Division, Department of Physics, Royal Institute of Technology, Stockholm, Sweden. TRITA-FYS 2005:50

Abstract

This thesis deals with the fabrication and the characterization of periodically-poled crystals for use in lasers to generate visible and UV radiation by second-harmonic generation (SHG) through quasi-phasematching (QPM). Such lasers are of practical importance in many applications like high-density optical storage, biomedical instrumentation, colour printing, and for laser displays.

The main goals of this work were: (1) to develop effective monitoring methods for poling of crystals from the $KTiOPO_4$ (KTP) family, (2) to develop useful non-destructive domain characterization techniques, (3) to try to find alternative crystals to KTP for easier, periodic poling, (4) to investigate the physical mechanisms responsible for optical damage in KTP. The work shows that the in-situ SHG technique used together with electro-optic monitoring, makes it possible to obtain reliable, real-time information regarding the poling quality over the whole crystal aperture during the electric-field poling process. Using this combined monitoring method, both KTP and Rb-doped KTP (RKTP) crystals were successfully poled. By comparing these two crystals, we found that a low-doped KTP has a substantially reduced ionic conductivity and, thus, a high-quality periodic poling can be obtained without otherwise affecting the properties of the crystal. RKTP is a good alternative candidate to KTP for poling purpose. We have also shown that Atomic Force Microscopy (AFM) is an informative tool for investigating domain nucleation, growth, and merging. Furthermore, we have demonstrated a simple technique for 3D characterization of QPM samples. It utilizes a group-velocity mismatched, type-II SHG of femtosecond pulses for layer-by-layer monitoring of the effective nonlinearity along the propagation direction of the beam. The quality of these crystals was finally reflected in a number of SHG experiments with a variety of laser sources. High energies and high efficiencies were thus demonstrated using CW, mode-locked and Q-switched lasers. Gratings with pitches smaller than 3 μm, were demonstrated for first-order UV generation. Type-II QPM SHG was demonstrated as a technique for reducing the fabrication constraints.

High intensity light in the visible and the UV leads to modification of the material properties and, eventually, to optical damage. In KTP and its isomorphs, the first sign of material change is an optically-induced absorption. We have used thermal-lens spectroscopy with a common-path interferometer for high-sensitivity measurements of green light-induced infrared absorption dynamics in single-domain and periodically-poled KTP (PPKTP). The saturated, green light-induced absorption has been shown to be consistently higher in periodically-poled crystals, and is attributed to the creation of stoichiometric and interstitial defects in the crystals during the poling process. Finally, irreversible bulk damage thresholds in PPKTP have been determined for pulsed frequency converters. As the characteristics of optical damage are closely related to the material quality, this investigation can provide useful information for crystal manufactures and will help to optimise the crystal growth conditions.

Keywords: Nonlinear optics, second-harmonic generation, quasi-phasematching, type-I QPM SHG, type-II QPM SHG, KTP, RKTP, periodic electric-field poling, optical damage threshold, grey tracking, green-induced infrared absorption.

List of publications

Publications included in the thesis:

Paper I:
V. Pasiskevicius, S. Wang, J. A. Tellefsen, F. Laurell, and H. Karlsson "Efficient Nd:YAG laser frequency doubling with periodically poled KTP", Appl. Opt. **37**, 7116 (1998).

Paper II:
S. Wang, V. Pasiskevicius, F. Laurell, and H. Karlsson "Ultraviolet generation by first-order frequency doubling in periodically poled $KTiOPO_4$", Opt. Lett. **23**, 1883 (1998).

Paper III:
S. Wang, V. Pasiskevicius, J. Hellström, F. Laurell, and H. Karlsson "First-order type II quasi-phase-matched UV generation in periodically poled KTP", Opt. Letts. **24**, 978 (1999).

Paper IV:
S. J. Holmgren, V. Pasiskevicius, S. Wang and F. Laurell, "Three-dimensional characterization of the effective second-order nonlinearity in periodically poled crystals", Opt. Lett. **28**, 1555 (2003).

Paper V:
S. Wang, V. Pasiskevicius and F. Laurell, "Dynamics of green light-induced infrared absorption in $KTiOPO_4$ and periodically poled $KTiOPO_4$", J. Appl. Phys. **96**, 2023 (2004).

Paper VI:
C. Canalias, S. Wang, V. Pasiskevicius, and F. Laurell, "Nucleation and growth of periodic domains during electric field poling in flux-grown $KTiOPO_4$ observed by atomic force microscopy", (submitted to Appl. Phys. Lett.).

Paper VII:
S. Wang, V. Pasiskevicius and F. Laurell, "High efficiency periodically poled Rd-doped $KTiOPO_4$ using in-situ monitoring", (submitted to J. Appl. Phys.).

Other publications related to, but not included in this thesis:

Paper A:
G. Hansson, H. Karlsson, S. Wang and F. Laurell, "Transmission measurements in KTP and isomorphic compounds", Appl. Opt. **39**, 5058 (2000).

Paper B:
S. Wang, V. Pasiskevicius and F. Laurell, "High-power and high-efficiency frequency doubling of Q-switched Nd:YAG lasers in periodically poled KTP", Technical Digest. Summaries of papers presented at the Conference on Laser and Electro-Optics.

Postconference Edition. CLEO'99. Conference on Lasers and Electro-Optics (IEEE Cat. No. 99CH37013), 445 (1999).

Paper C:
V. Pasiskevicius, S. J. Holmgren, S. Wang and F. Laurell, "Simultaneous second-harmonic generation with two orthogonal polarization states in periodically poled KTP", Opt. Lett. **27**, 1628 (2002).

Paper D:
E. U. Rafailov, W. Sibbett, A. Mooradian, J. G. McInerney, H. Karlsson, S. Wang and F. Laurell, "Efficient frequency doubling of a vertical-extended-cavity surface-emitting laser diode by use of a periodically poled KTP crystal", Opt. Lett. **28**, 2091 (2003).

Paper E:
D. B. S. Soh, C. Codemard, S. Wang, J. Nilsson, J. K. Sahu, F. Laurell, V. Philippov, Y. Jeong, C. Alegria and S. Baek, "A 980-nm Yb-doped fiber MOPA source and its frequency doubling", IEEE Photon. Technol. Lett. **16**, 1032 (2004).

Paper F:
B. Agate, E. U. Rafailov, W. Sibbett, S. M. Saltiel, K. Koynov, M. Tiihonen, S. Wang, F. Laurell, P. Battle, T. Fry, T. Roberts, E. Noonan, "Portable ultrafast blue light sources designed with frequency doubling in KTP and $KNbO_3$", IEEE J. Selected Topics in Quantum Electronics **10**, 1268 (2004).

Paper G:
S. Johansson, S. Spiekermann, S. Wang, V. Pasiskevicius, F. Laurell and K. Ekvall, "Generation of turquoise light by sum frequency mixing of a diode-pumped solid-state laser and a laser diode in periodically poled KTP", Optics Express **12**, 4935 (2004).

Paper H:
J. Janousek, S. Johansson, P. Tidemand-Lichtenberg, S. Wang**,** J. L. Mortensen, P. Buchhave and F. Laurell, "Efficient all solid-state continuous-wave yellow-orange light source", Optics Express **13,** 1188 (2005).

Paper I:
S. Wang, V. Pasiskevicius, F. Laurell, Y. Liao, J. Liu and R. J. D. Miller, "Intracavity frequency doubling of $Nd:YVO_4$ disk laser with periodically poled $KTiOPO_4$", Conference on Lasers and Electro-Optics (CLEO 2000). Technical Digest. Postconference Edition. TOPS **39**, (IEEE Cat. No. 00CH37088), 16 (2000).

Paper J:
A. Piskarskas, V. Smilgevicius, A. Stabinis, V. Jarutis, V. Pasiskevicius, S. Wang, J. Tellefsen, and F. Laurell, "Noncollinear second-harmonic generation in periodically poled $KTiOPO_4$ excited by a Bessel beam", Opt. Lett. **24**, 1053 (1999).

Paper K:
V. Smilgevicius, A. Stabinis, A Piskarskas, V. Pasiskevicius, J. Hellström, S. Wang and F. Laurell, "Noncollinear optical parametric oscillator with periodically poled KTP", Opt. Comm. **173**, 365 (2000).

Contents

1. Introduction

1.1. Aim and motivation

Compact lasers in the visible and the UV spectral regions can be used in a variety of applications, for example, for laser displays, bio-medical instruments, photo processing, in spectroscopy, and for semiconductor wafer inspection. Among these, laser displays and biomedical instruments are of particular interest as these areas have an enormous potential market.

The laser display can provide high brightness and a better choice of colours. The higher brightness will lead to improved image quality, whereas the free choice of colours would allow broader colour gamut and, hence, better colour saturation to be obtained which means that one would obtain a much better colour reproduction in the image. The primary colours required to fill the gamut should fall within the wavelength ranges of 450-470 nm for blue, 520-540 nm for green and 630-650 nm for the red source, respectively. More colours, such as turquoise can be used in the near future. The power required varies depending on the size of the screen. 1 W per colour for a 10-ft x16-ft screen, and approximately 20 mW per colour for a 16-in display[1]. How do we get these three primary colours? The red source is supposed to rely on laser diodes, which are reasonably well developed. For the blue source, diodes exists as well, but at 460 nm, the power is still too low for many applications and the green diodes are not yet commercially available due to problems with the semiconductor material.

In many biomedical applications, gas lasers such as argon and krypton lasers have been used to provide several discrete laser emission lines. Argon-ion lasers operating at 488 nm and 514 nm are typically used for flow cytometry and DNA sequencing, which is based on fluorescence excitation of dye molecules attached to the sample under investigation. Fluorescence excitation is also used in confocal microscopy where the fluorescent light is collected to build a 3D image of the sample. By tagging different molecules with different fluorophores, in combination with multi-wavelength laser excitation, considerably more information can be obtained in one single measurement. Krypton lasers at 568 nm are here often used as a green source together with the argon laser. The gas lasers although, functioning quite well in these instruments, they are still bulky and noisy and have a low efficiency. Hence, researchers and engineers are today trying to develop replacement and complementary compact lasers in the blue–green and yellow light regions for these applications.

In diode-pumped solid-state lasers (DPSSL), the light emitted from most rare-earth doped hosts appear in the near infrared part of the spectrum, while the applications just described are in the visible. To obtain the necessary visible laser light, one of the solutions will be to use nonlinear frequency conversion techniques to extend the use of these lasers.

In principle, arbitrary visible and near-UV wavelengths can be obtained by second-harmonic generation (SHG) and sum-frequency generation (SFG) of the output from available laser diodes, or DPSSLs, in many nonlinear optical materials. To do so, two criteria have to be fulfilled: 1) energy conservation and 2) momentum conservation.

Many of the demanded wavelengths, like 473 nm, 488 nm, 491 nm, 532 nm, 561 nm, etc, can thus be obtained by properly mixing of the emission from commonly available lasers. Table 1.1 lists the wavelengths from some of the most common and important DPSSLs and diode sources.

Nd:YAG	**Nd: YLF**	**Nd: YVO_4**	**Nd:$GdVO_4$**	**Er-Yr glass**	**Laser diode**
1319 nm	1053 nm	1340 nm	1063 nm	1555 nm	760 nm, 808 nm
1064 nm	1047 nm	1064 nm	913 nm	2900 nm	910 nm, 940 nm
946 nm	908 nm	914 nm			975 nm, 980 nm

Table 1.1 Example of some laser emission lines from DPSSLs and laser diodes.

Traditionally, birefringent phasematching (BPM) has been used to obtain the momentum conservation. However, it is not possible to cover the whole spectrum from UV to IR by this technique in one single material. Instead, quasi-phasematching (QPM) in periodically-poled (PP) materials should be utilized. QPM relies on an artificial wave vector to compensate for the accumulated phase mismatch between the interacting waves and makes it possible to generate any wanted wavelengths in the transparency range of the nonlinear material. As the artificial grating vector in QPM assures momentum conservation, a high conversion efficiency for frequency mixing can be obtained. So far, the most successful technique for making QPM devices is by periodic poling of ferroelectric crystals. One of the topics of this thesis is devoted to the engineering of artificial domain structures in potassium titanyl phosphate, $KTiOPO_4$ (KTP), a nonlinear material which has higher optical damage threshold than most alternative ferroelectrics.

As an example of how periodic poling of KTP has been exploited, together with an innovative laser design, the Cobolt AB dual Calypso laser[2] can be mentioned. It is simultaneously running on two wavelengths, namely 491 and 532 nm, but emitted in one single beam. It utilizes two QPM gratings, with different periods in the same KTP substrate, as the frequency converter. The 491 nm wavelength is generated from SFG of the 914 nm output from a Nd: YVO_4 laser and the 1064 nm output from a Nd:YAG laser, while the green 532 nm output from the Calypso laser is generated from the remaining 1064 nm radiation by intra-cavity frequency doubling. This dual-line laser is claimed to be the first true blue-green Ar-laser replacement. Fig. 1.1 shows the drawing of the laser. It is, of course, possible to add another blue line at 457 nm to this laser by adding a frequency doubling grating for the 914 nm line, too.

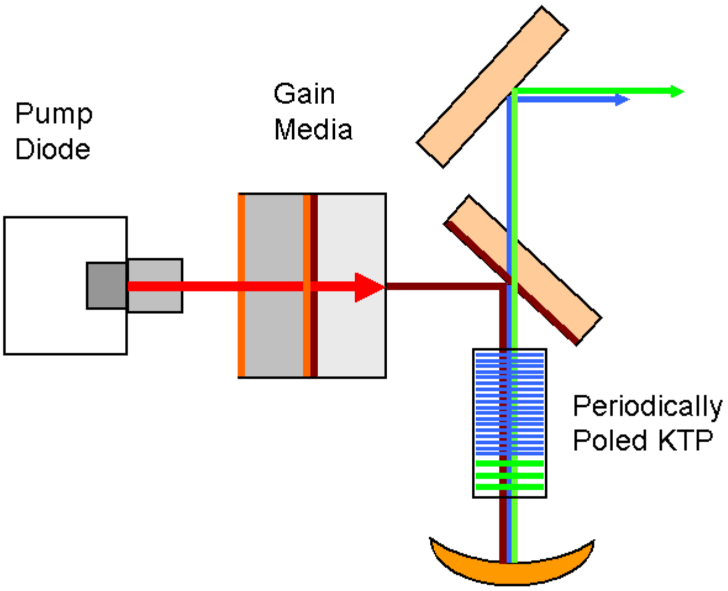

Fig. 1.1 A Dual line, 491 nm and 532 nm laser using one PPKTP having two consecutive gratings for frequency conversion. The fundamental beams are emitted from two independent gain media, Nd:YAG and Nd: YVO_4, pumped by one laser diode[2].

In the same fashion, the three primary colours, blue, green, and red for laser displays can be generated simultaneously in a single laser unit, by proper design of the grating for the QPM and the choice of laser gain media. For instance, by frequency doubling the 914 nm output from the Nd: YVO_4 laser, and the 1064 nm and the 1319 nm output from the Nd:YAG laser, we can achieve a compact RGB unit.

At this point, it should be clear that PP crystals have a potential to become a key component in the design of many solid-state lasers in the future. However, a lot of issues remain to be solved in order to obtain a simple and reliable fabrication process for PP crystals with high yield and high quality.

One of the primary demands on a laser display projector is that the employed lasers should be compact, efficient, of high output power and have a long lifetime. This, in turn, requires that the nonlinear material should have a large nonlinearity and a high damage threshold level. KTP is known to be comparatively resistant to optical damage in the visible part of spectrum and it is hence one of the most attractive candidates for making the QPM devices. However, this has not been quantified to any larger extent. Damage effects such as grey tracking, as well as photorefractive damage, have all been observed for KTP when used at high powers. It would therefore be necessary to describe and to quantify these effects under various laser operating conditions.

The aim of the work contained in this thesis has been to study KTP under electric-field poling and to try to develop practical procedures for the poling in order to get high-quality QPM crystals in a controllable manner. Furthermore, I have demonstrated different types of QPM in KTP and studied the performance of QPM crystals generating both visible and UV radiation in general. I have also tried to understand the mechanisms of laser-induced damage and eventually define the damage threshold levels. This work should lead to an improved understanding of how the material should be employed in nonlinear frequency conversion applications. Finally, I have also studied the physical properties of the recently synthesized crystal, Rb-doped KTP (RKTP), and investigated its applicability for electric-field poling. The efforts made in this thesis work should contribute to a better understanding of both KTP and RKTP and could, in part, be used in the commercialisation steps of QPM devices.

1.2. Outline of the thesis

The purpose of the present thesis is to constitute the basis for the discussion of the original research work presented in the publications. In Chapter 2, the basic theory of nonlinear optics, particularly the second-order nonlinear processes, is reviewed. Quasi-phasematching theory is paid a special attention to and, in Chapter 3, how to implement QPM is addressed. Following this, the second-harmonic generation based on QPM is introduced theoretically, accompanied with experiment results in Chapter 4. In Chapter 5, one can find the answer to why I have focused my work on KTP and RKTP but not on the other ferroelectrics. After this, the material related properties are discussed. In Chapter 6, the emphasise is on the fabrication issues for periodically-poled KTP (PPKTP) and for PPRKTP, as well as on the different techniques for evaluating the poled material. SHG, results from PPKTP and PPRKTP are also compared. It is worth noting that an improved control method for the poling of KTP and its isomorphs, i.e., the in-situ SHG was developed in this work. It is well known that KTP suffers from photochromic damage at high input power level in the visible spectrum. For this reason, in Chapter 7, the mechanisms of laser-induced damages in KTP is reviewed. The common path interferometer technique was developed in order to measure the green-induced infrared absorption. With this setup, the small absorption level both in KTP and in PPKTP is measurable. In Chapter 8, the original research work is summarized and the contribution of the candidate is presented. Finally, my main conclusions are given in Chapter 9.

References of Chapter 1

[1] W. P. Risk, T. R. Gosnell and A.V. Nurmikko, “Compact Blue-Green Laser”, Cambridge University Press (2003).

[2] J. Nordborg and H. Karlsson, Euro Photonics **June/July**, 28 (2004).

2. Basic principles of nonlinear optics

2.1. *The nature of the nonlinear polarization*

Soon after the invention of the laser, Franken and co-workers demonstrated frequency doubling of a ruby laser using a quartz crystal in 1961[1]. This was the first experiment on optical frequency conversion and, hence, an important milestone of the investigation of the nonlinear optical properties of matter.

In an optical medium, the valence electrons are displaced from their normal orbits by the oscillating electric field, $\boldsymbol{E}$**,** of an incident light wave. Hence, the electrons and the remaining ions form oscillating dipoles and will emit photons. The macroscopic manifestation of the oscillating dipoles is the oscillating polarization, $\boldsymbol{P}$. Therefore, the induced polarization will radiate a new field at the frequency of oscillation. The induced polarization can be either linear (displacement is small) or significantly nonlinear depending on the magnitude of the applied electric field. In the linear case, where the strength of the applied field is small, the emitted radiation has the same frequency as the incident light. However, if an intense field is applied to the optical medium, the relationship between the induced polarization and the applied electric field is nonlinear. The radiated field, will oscillate with harmonics, starting from the double frequency and then continuing with the triple one, etc. Fig. 2.1 shows the dependence of the induced polarization on the applied electric field.

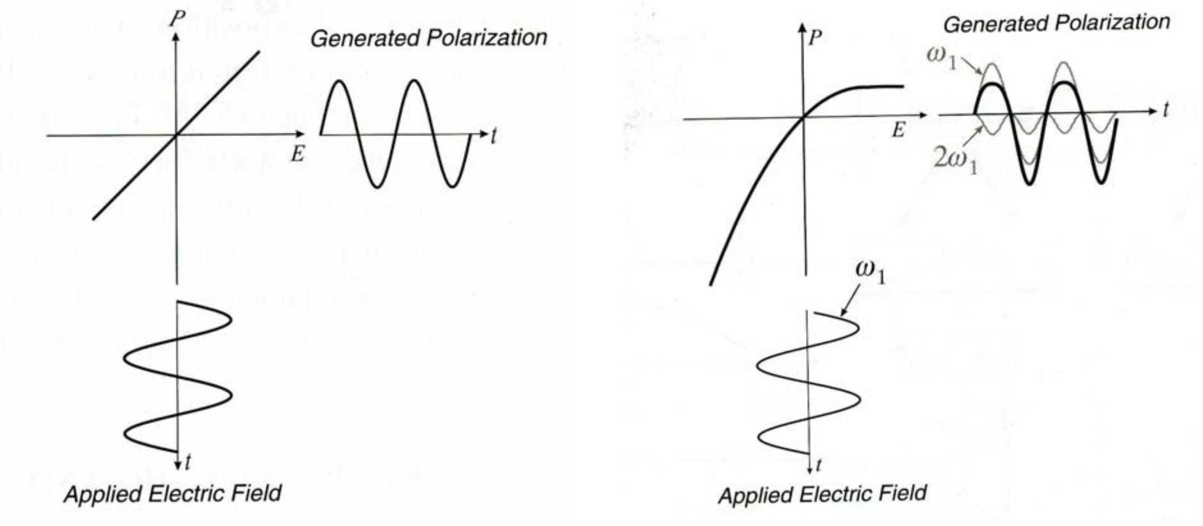

(*a*) **(*b*)**

Fig. 2.1 The relationship between the induced polarization and the applied electric field. (a): Linear dependence holds for a low input field strength.(b):At a large field strength, the polarization has been distorted and will contain harmonic frequency components. In this example, a second-harmonic of the applied frequency shows up[2].

The relation between the induced polarization and the applied electric field is given by the expression:

$$P = \varepsilon_0 \chi^{(1)} E_1 + \varepsilon_0 \chi^{(2)} E_1 E_2 + \varepsilon_0 \chi^{(3)} E_1 E_2 E_3 + ... \qquad (2\text{-}1)$$

where ε_0 is the dielectric constant in vacuum and $\chi^{(i)}$ is the susceptibility tensor of the i^{th} order. The term $\varepsilon_0 \chi^{(1)} E_1$ is responsible for the conventional linear optics such as the index of refraction, while the first nonlinear term, the second order one, $\varepsilon_0 \chi^{(2)} E_1 E_2$, is responsible for the second-harmonic generation, the sum- or difference-frequency generation, optical parametric oscillation, optical rectification and the Pockels effect. The third term, $\varepsilon_0 \chi^{(3)} E_1 E_2 E_3$, gives rise to effects such as the third-harmonic generation, intensity-dependent refractive index, and Brillouin scattering. This thesis will mainly deal with the second order effects utilizing the $\chi^{(2)}$ component, for example for second-harmonic generation.

2.2. Second-order nonlinear processes and the d-coefficient

Among the second-order nonlinear processes, probably the most important ones in an application perspective, are the second-harmonic generation, the sum-frequency generation, the difference-frequency generation (DFG) and the optical parametric generation (OPG). The first condition for such processes to appear is the photon energy conservation. Two waves, at frequency ω_1 and ω_2, incident on a nonlinear medium, can combine in different ways. For SFG, the photon energies are added to create a new photon with higher energy, $\omega_3 = \omega_1 + \omega_2$. SHG is a special case of SFG when the two photons have the same frequency and come from the same laser mode, i.e., $\omega_3 = 2\omega_1 = 2\omega_2$. In the case of DFG, a photon with low energy is created by subtraction of the lower energy from the higher, i.e., $\omega_3 = \omega_1 - \omega_2$. In OPG, a pump photon is split into two lower energy photons, called the signal photon of frequency ω_s and the idler photon of frequency ω_i, respectively. To keep the energy conservation, $\omega_p = \omega_s + \omega_i$. If the OPG is put into a resonator, an optical parametric oscillator (OPO) is constructed. Fig. 2.2 illustrates theses processes schematically.

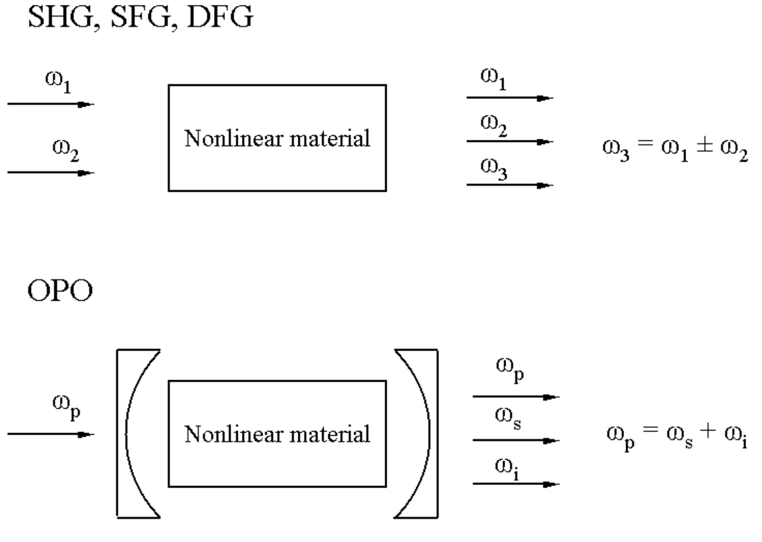

Fig. 2.2 Schematic illustrations of the second-order frequency conversion processes.

Second-order nonlinear processes can only happen in materials without inversion centre. In practice, the nonlinear coefficient, *d,* is more frequently used than $\chi^{(2)}$ and they are interrelated by the expression:

$$d_{il} \equiv \frac{1}{2}\chi_{ijk}^{(2)} \tag{2-2}$$

where, *i, j, k* are the Cartesian indices of the different frequency components polarization. Altogether, there are $3x3x3 = 27$ such components. Under intrinsic permutation symmetry, the *j and k* indices indexing $\chi_{ijk}^{(2)}$ are interchangeable. Hence, a contracted notation can be introduced where *j and k* together are replaced by the index *l* and can take on the following values:

$$\begin{array}{llllllll} jk: & 11 & 22 & 33 & 23{,}32 & 13{,}31 & 12{,}21 \\ l: & 1 & 2 & 3 & 4 & 5 & 6 \end{array} \tag{2-3}$$

The number of independent elements are thereby reduced from 27 to 18 and the second-order polarization in *d*-matrix notation now gets the form:

$$\begin{bmatrix} (P_x)_{\omega_3}^{(2)} \\ (P_y)_{\omega_3}^{(2)} \\ (P_z)_{\omega_3}^{(2)} \end{bmatrix} = 2\varepsilon_0 K(\omega_3;\omega_1,\omega_2) \begin{bmatrix} d_{11} & d_{12} & d_{13} & d_{14} & d_{15} & d_{16} \\ d_{21} & d_{22} & d_{23} & d_{24} & d_{25} & d_{26} \\ d_{31} & d_{32} & d_{33} & d_{34} & d_{35} & d_{36} \end{bmatrix} \begin{bmatrix} (E_x)_{\omega_1}(E_x)_{\omega_2} \\ (E_y)_{\omega_1}(E_y)_{\omega_2} \\ (E_z)_{\omega_1}(E_z)_{\omega_2} \\ (E_y)_{\omega_1}(E_z)_{\omega_2} + (E_z)_{\omega_1}(E_y)_{\omega_2} \\ (E_x)_{\omega_1}(E_z)_{\omega_2} + (E_z)_{\omega_1}(E_x)_{\omega_2} \\ (E_x)_{\omega_1}(E_y)_{\omega_2} + (E_y)_{\omega_1}(E_x)_{\omega_2} \end{bmatrix} \tag{2-4}$$

where $K(\omega_3;\omega_1,\omega_2)$, the degeneracy factor, is equal to ½ when $\omega_1 = \omega_2$, and equal to 1 if $\omega_1 \neq \omega_2$.

The number of independent components of d_{il} will further decrease from 18 to 10 when the Kleinmann symmetry conditions are valid. It applies to the cases of when all the frequencies involved in the interaction are far away from any resonance frequencies of the nonlinear material[3]. In this case, $d_{21} = d_{16}$; $d_{24} = d_{32}$; $d_{31} = d_{15}$; $d_{13} = d_{35}$; $d_{12} = d_{26}$; $d_{32} = d_{24}$; $d_{14} = d_{36} = d_{25}$.

2.3. The nonlinear wave propagation and coupled wave equation

The propagation of light in a nonlinear, nonmagnetic medium is governed by the nonlinear wave equation:

$$\nabla \times \nabla \times \boldsymbol{E} + \mu_0 \sigma \frac{\partial E}{\partial t} + \frac{1}{\varepsilon_0 c^2}\frac{\partial^2}{\partial t^2}\boldsymbol{D} = -\frac{1}{\varepsilon_0 c^2}\frac{\partial^2}{\partial t^2}\boldsymbol{P}^{NL} \tag{2-5}$$

where μ_0 is the permeability of vacuum and σ is the conductivity of the material. The polarization ***P*** is split into its linear and nonlinear parts, viz:

$$\boldsymbol{P} = \boldsymbol{P}^L + \boldsymbol{P}^{NL} \tag{2-6}$$

D is the linear displacement field and is defined in the following way

$$\boldsymbol{D} = \varepsilon_0 \boldsymbol{E} + \boldsymbol{P}^L \tag{2-7}$$

Using the vector relations $\nabla x \nabla x \boldsymbol{E} \equiv \nabla(\nabla \boldsymbol{E}) - \nabla^2 \boldsymbol{E}$ and $\nabla(\nabla \boldsymbol{E}) = 0$, Eq (2-5) now changes into the form given by:

$$\nabla^2 \boldsymbol{E} = \mu_0 \sigma \frac{\partial \boldsymbol{E}}{\partial t} + \varepsilon_0 \mu_0 \frac{\partial^2 \boldsymbol{E}}{\partial t^2} + \mu_0 \frac{\partial^2 \boldsymbol{P}^L}{\partial t^2} + \mu_0 \frac{\partial^2 \boldsymbol{P}^{NL}}{\partial t^2} \tag{2-8}$$

To solve this equation analytically, several assumptions can be made to simplify the solution. First, let the electromagnetic waves be quasi-monochromatic plane waves and propagate along the x-axis. The electric field and polarization can then be written as:

$$\boldsymbol{E}(x,t) = \frac{1}{2}\left(\boldsymbol{E}(x,\omega) e^{i(\omega t - kx)} + c.c\right)$$

and (2-9)

$$\boldsymbol{P}(x,t) = \frac{1}{2}\left(\boldsymbol{P}(x,\omega) e^{i(\omega t - kx)} + c.c\right)$$

We also assume that the envelope of the plane waves changes slowly with distance. Then, the second-order derivatives with respect to distance and time can be neglected. This is called the slowly-varying envelope approximation, or SVEA:

$$\begin{gathered} \left|\frac{\partial^2 \mathrm{E}(x,\omega)}{\partial x^2}\right| << \left|k \frac{\partial E(x,\omega)}{\partial x}\right| \\ \left|\frac{\partial^2 E(x,\omega)}{\partial t^2}\right| << \left|\omega \frac{\partial E(x,\omega)}{\partial t}\right| \\ \left|\frac{\partial^2 P(x,\omega)}{\partial t^2}\right| << \left|\omega \frac{\partial P(x,\omega)}{\partial t}\right| << \omega^2 P(x,\omega) \end{gathered} \tag{2-10}$$

where *k* is the wave vector and *n* is the refractive index ,

$$k = \frac{n\omega}{c}, \qquad n = \sqrt{\varepsilon(\omega)} \tag{2-11}$$

By inserting Eq (2-9) into Eq (2-8) and taking the SVEA approximation into account, Eq (2-8) can be simplified to a first-order differential equation:

$$\frac{\partial \mathbf{E}}{\partial x} = -\alpha \mathbf{E} + \frac{i\mu_0 c\omega}{2n} \boldsymbol{P}^{NL} \tag{2-12}$$

where $\alpha = \mu_0 \sigma c/2$ is the loss coefficient in the material.

In a second-order nonlinear process, the induced polarizations, expressed in Eq (2-4), couple the three waves to each other. Substituting Eq (2-4) into Eq (2-12) and identifying relating terms, we can obtain a group of three coupled equations, viz:

$$\begin{aligned}
\frac{\partial E_1}{\partial x} &= -\alpha_1 E_1 + \frac{i\omega_1 d_{eff}}{n_1 c} E_3 E_2^* e^{-i(k_3-k_2-k_1)x} \\
\frac{\partial E_2}{\partial x} &= -\alpha_2 E_2 + \frac{i\omega_2 d_{eff}}{n_2 c} E_3 E_1^* e^{-i(k_3-k_2-k_1)x} \\
\frac{\partial E_3}{\partial x} &= -\alpha_3 E_3 + \frac{i\omega_3 d_{eff}}{n_3 c} E_1 E_2 e^{-i(k_1+k_2-k_3)x}
\end{aligned} \tag{2-13}$$

Here $k_3 - k_2 - k_1 = \Delta k$ is the phase mismatch between the three interacting waves and d_{eff} is the effective nonlinear coefficient originating from the *d*-matrix, expressed in Eq (2-4). The resulting values of d_{eff} will depend on the polarization directions of the incident fields and on the phasematching conditions.

2.4. Second-harmonic generation

2.4.1. Second-harmonic generation with plane waves

Second-harmonic generation is the special case of three-wave mixing where frequencies have been chosen to be $\omega_{SH} = \omega_F + \omega_F$, where $\omega_F = \omega_1 = \omega_2$ is the fundamental frequency of the incoming wave. Considering the momentum conservation criteria, $\Delta k = k_{SH} - 2k_F$, where $k_{SH} = k_3$ and $k_F = k_1 = k_2$. For lossless materials, for which $\alpha = 0$, the solution to the nonlinear, coupled-wave equations is simplified to:

$$\frac{\partial E_{SH}}{\partial x} = \frac{i\omega\, d_{eff}}{n_{SH} c} E_F E_F e^{(i\Delta k x)} \tag{2-14a}$$

$$\frac{\partial E_F}{\partial x} = \frac{i\omega\, d_{eff}}{n_F c} E_{SH} E_F^* e^{(-i\Delta k x)} \tag{2-14b}$$

At the low-conversion limit, where pump depletion is neglected, i.e., when $\partial E_F / \partial x = 0$, the intensity of the SHG is obtained by integrating Eq (2-14a) and its complex conjugate over the whole nonlinear crystal length *L*. Taking into account that the input intensity at the fundamental frequency ω_F is given by $I_F = \frac{1}{2}\varepsilon_0 n_F c E_F E_F^*$, we may express the intensity of the SHG in the following way:

$$I_{SH}(L) = \frac{2\omega^2 d_{eff}^2 L^2 I_F^2}{\varepsilon_0 c^3 n_{SH} n_F^2} \sin c^2 (\frac{\Delta kL}{2}) \tag{2-15}$$

Eq (2-15) tells us that, the SHG output has a quadratic dependence on the fundamental intensity, as well as on the length of the nonlinear crystal in the case of plane waves. The SHG output follows a *sinc*^{2}-curve accordingly, and reaches a maximum when the mismatch $\Delta k = 0$, as shown in Fig. 2.3.

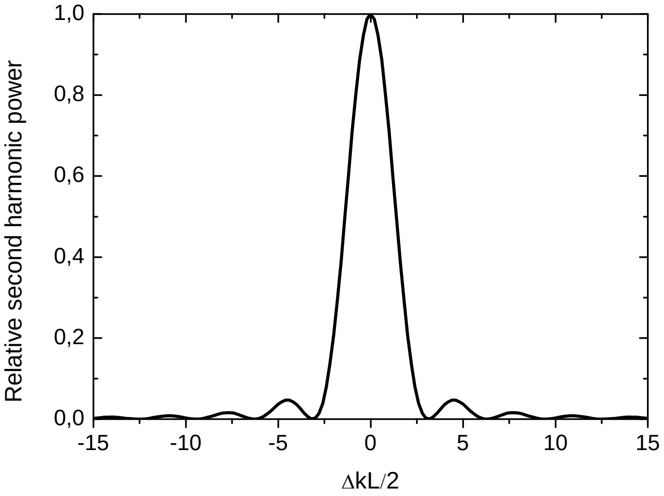

Fig. 2.3 Normalized second-harmonic generation as a function of ΔkL.

2.4.2. Second-harmonic generation with Gaussian beams

Gaussian beams are the most commonly used with lasers and in nonlinear interaction studies. Boyd and Kleinman[4] solved the problem of deriving the conversion efficiency with Gaussian beams. For a focused fundamental Gaussian beam with beam cross-section $A = \pi\omega_0^2$, where ω_0 is the beam waist radius, and with an interaction length *L*, we can get the second-harmonic generation power, taking into account that $P = IA$, as follows:

$$P_{SH} = \left(\frac{2\omega_F^2 d_{eff}^2 k_F P_F^2}{\pi n_F^2 n_{SH} \varepsilon_0 c^3} \right) Lh(B,\xi) \tag{2-16}$$

where ω_F and k_F are the fundamental frequency and wave vector, respectively, *c* is the speed of light in vacuum, and ε_0 is the permittivity of free space. *h(B,ξ)* is the Boyd and Kleinman focusing factor. $\xi = L/b$, where $b = 2\pi n_F \omega_0^2 / \lambda$, is the confocal parameter for a beam waist radius ω_0. *B* is double refraction parameter. For so-called noncritical (90°) phasematching, there is no walk-off and $B = 0$, as shown in Fig. 2.4. $h(B,\xi)$ is maximized for a value of $\xi = 2.84$, which then gives the optimum focusing condition.

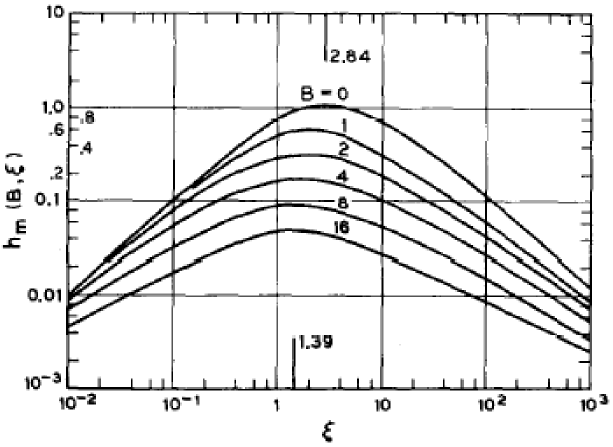

Fig. 2.4 Plot of the focusing factor $h(B,\xi)$ as a function of the focusing parameter ξ for various values of double refraction parameter B.

From Eq (2-16), we note that under optimum focusing conditions, the SHG power increases linearly with the crystal length rather than quadratically as in the plane wave solution, Eq (2-15).

2.5. Phasematching using birefringence

When the phase mismatch factor, $\Delta k = 0$, exact phasematching is reached. Unfortunately, due to material dispersion, e.g. that $n_{SH} \neq n_F$, this condition is not often fulfilled, i.e. $\Delta k \neq 0$. Fig. 2.5 shows how the refractive indices of flux-grown KTP change monotonously with the wavelength[5].

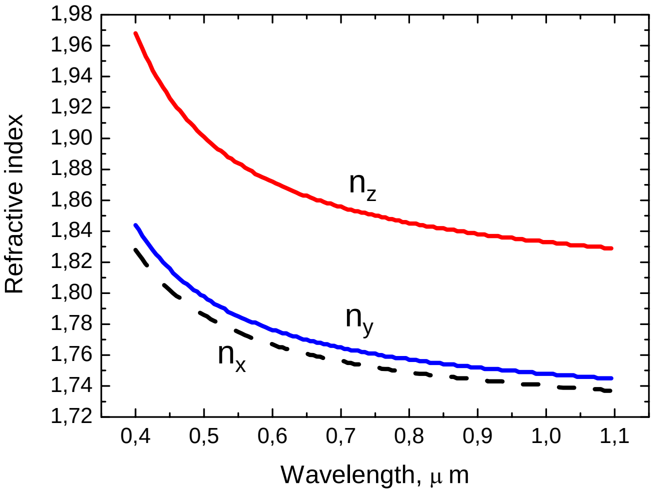

Fig. 2.5 The dispersion curves of flux-grown KTP. n_x, n_y and n_z are the refractive indices in x, y and z direction of KTP, respectively.

For a fixed amount of Δk, the SHG power varies as a function of the crystal length with a period of $L = 2\pi / \Delta k$ along the crystal. Half of this distance is called the coherence length L_c, which is the distance from the crystal entrance to the point at which the SHG power reached its maximum. Over this characteristic distance, a phase difference of π is accumulated between the two interacting waves.

$$L_c = \frac{\pi}{\Delta k} \tag{2-17}$$

So, if the crystal is not perfectly phasematched, the maximum SHG power will be generated at one coherence length from the entrance, followed by a decrease in SHG power. The power will then oscillate back and forth between the harmonic and the fundamental waves with the coherence length. Typically the coherence length is limited to about 10 μm, which is, of course, much shorter than the useful length of the crystal which is of the order of 1 cm for efficient conversion. Therefore, phasematching is essential to achieve a practically useful frequency-converted powers.

There are two main types of phasematching, depending on the two possible orientations of the linear polarization vectors of the incident beams. In the type-I SHG process, both of the fundamental polarization vectors are parallel, whereas in the type-II SHG process, the polarization vectors are orthogonal. These two types of processes will be described in more detail in Chapter 4.

The conventional method of obtaining phasematching is by utilizing the birefringence of the nonlinear crystals. The birefringence is defined as the difference between the refractive indices of the ordinary and extraordinary wave on the principle axes of the crystal, $n^o - n^e$. The refractive index of the extraordinary wave, n^e, is in general a function of the polar angle, defined as θ in Fig. 2.6, between the optical axis and the wave vector[6], expressed as:

$$n^e(\theta) = n^o \sqrt{\frac{1+\tan^2(\theta)}{1+(n^o/n^e)^2 \tan^2(\theta)}} \tag{2-18}$$

To explain how birefringent phasematcing (BPM) works in a simple manner, we will use a negative uniaxial birefringent crystal ($n^o > n^e$) as an example. The dependences of the refractive indices of the direction of light propagation inside the crystal, as shown in Fig. 2.6, is a combination of a sphere with radius n^o for the ordinary beam and an ellipsoid of rotation with semiaxes n^o and n^e for the extraordinary beam.

In the case when the phasematching is achieved at an angle θ, point A in Fig. 2.6 [$n_F^o = n_{SH}^e(\theta)$] other than for $\theta = 90^o$, with respect to the optic axis of a uniaxial crystal, the direction of power flow (pointing vectors shown as $\boldsymbol{S_F}$ and $\boldsymbol{S_{SH}}$ in Fig. 2.6) of the fundamental and the second harmonics will not be completely collinear. The latter will be rotated by a walk-off angle, called ρ, from the former. For a negative uniaxial crystal and type-I phasematching, this angle is given by[7]:

$$\tan\rho = \frac{(n_F^o)^2}{2}\left[\frac{1}{(n_{SH}^e)^2} - \frac{1}{(n_{SH}^o)^2}\right]\sin 2\theta \tag{2-19}$$

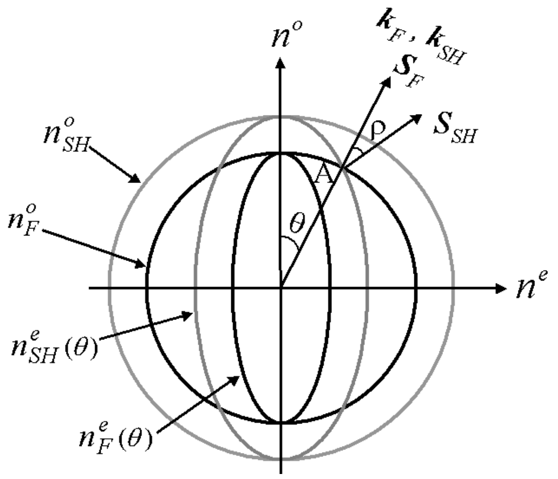

Fig. 2.6 Dependence of the refractive index on light propagation direction and polarization in negative uniaxial crystals. Phasematching is achieved at point A[7]*.*

Walk-off reduces the spatial overlap between the two interacting waves, which limits the interaction length. The distance at which the beams completely separate is called the aperture length and is given by the expression:

$$L_a = a / \rho \tag{2-20}$$

where a is the beam diameter. Obviously, the walk-off limits the ability to focus tightly, hence lowering the conversion efficiency.

It is sometimes possible to allow both the fundamental and the second-harmonic waves to propagate collinearly along the optic axis of the crystal, i.e., $\theta = 90^o$. This is called noncritical phasematching (NCPM), and this will eliminate the walk-off. Furthermore, the angular tolerance of NCPM is increased because the dependence of Δk on the angular misalignment, $\delta\theta$, is due to a much smaller quadratic term, instead of a linear relationship as is the case of critical phase matching. NCPM can be realized through temperature tuning or by modifying the chemical composition of the crystal.

For bixial crystals, the dependence of light propagation on the crystalline properties in birefringent phasematching is more complicated than in the case of uniaxial crystals, but the methodology is the same. More details on this topic can be found from the reference[6].

Although birefringent phasematching is convenient, it has severe disadvantage. The phasematching range is restricted by the birefringence and the dispersive properties of the nonlinear material. For instance, in KTP, the shortest wavelength for type-II noncritical phasematching is 0.993 μm which hinders blue light to be generated by frequency doubling[5]. Due to a too small birefrigence, the same is also true for $LiNbO_3$[8]. Moreover, the effective nonlinear coefficients vary depending on both the propagation and the polarization direction of the interacting beams. Furthermore, it is worth noting that the largest nonlinear coefficients for two-wave mixing, the d_{33} coefficient, cannot be used in BPM.

One way to go around the problems with birefringent phasematching is to use quasi-phasematching, which will be discussed in the next chapter.

References of Chapter 2

[1] P. A. Franken, A. E. Hill, C. W. Peters and G. Weinreich, Phys. Rev. Lett. **7**, 118 (1961).

[2] W. P. Risk, T. R. Gosnell and A. V. Nurmikko, “Compact Blue-Green Laser”, Cambridge University Press (2003).

[3] D. A. Kleinman, Phys. Rev. **126**, 1977 (1962).

[4] G. D. Boyd and D. A. Kleinman, J. Appl. Phys. **39**, 3597(1968).

[5] T. Y. Fan, C. E. Huang, B. Q. Hu, R. C. Eckardt, Y. X. Fan, R. L. Byer and R. S. Feigelson, Appl. Opt. **26**, 2390 (1987).

[6] V. G Dmitriev, G. G. Gurzadyan and D. N. Nikogosyan, “Handbook of Nonlinear Optical Crystals”, Springer-Verlag Berlin, Heidelberg, New York, Third Revised Edition (1999).

[7] W. Koechner, “Solid-State Laser Engineering”, Springer-Verlag Berlin, Heidelberg, New York, Fifth Revised and Updated Edition (1999).

[8] M. Houe and P. D. Townsend, J. Appl. Phys. **28**, 1747 (1995).

3. Quasi-phasematching

3.1. *Theory*

Quasi-phasematching is a technique for compensation of the phase-velocity differences between the interacting waves in a nonlinear frequency conversion process. In QPM, the accumulation of phase mismatch is prevented through a spatial modulation of the sign of the nonlinear susceptibility. Thus, the nonlinear medium is physically altered in a periodic fashion along the length of the crystal to prevent the flow of energy away from the generated wave. In a ferroelectric crystal, this is obtained by changing the domain orientation of the material periodically, thereby introducing an extra grating vector, $\boldsymbol{k_Q}$. Fig. 3.1 illustrates how the artificial wave vector compensates the wave-vector mismatch for SHG.

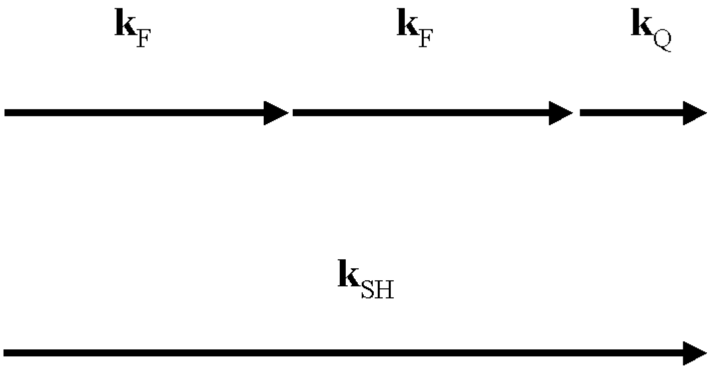

Fig. 3.1 Grating vector, $\boldsymbol{k_Q}$ *is used to compensate the mismatch between the fundamental wave vector* $\boldsymbol{k_F}$ *and the SH wave vector* $\boldsymbol{k_{SH}}$ *.*

This technique was first proposed by Armstrong *et al*[1] in 1962. Mathematically, we can consider the change of sign as being equivalent to a π phase shift ($e^{i\pi} = -1$). From an engineering point of view, in a SHG process, each layer length is chosen, or fabricated, such that the $-\pi$ phase shift obtained by the domain reversal is matching the phase shift obtained between the driving fundamental wave and the generated SH wave. The overall phase mismatch for each period is thus returned to zero, ensuring efficient, second-harmonic generation. Although the QPM interaction reduces the effective nonlinear coefficient by a factor of $2/\pi$, the overall conversion efficiency can still be several times larger than with BPM, because in this case, the largest nonlinear coefficient, d_{33}, can be utilized. Then, all the waves are polarized along the polar axis, which is impossible in BPM. The highest second-harmonic conversion efficiency is obtained for first-order QPM which is obtained when the sign of the nonlinear coefficient is reversed every coherence length, L_c. When the sign of the nonlinear coefficient is reversed every three coherence lengths, it is named third-order QPM. Fig. 3.2 shows the different cases of phasematching for a typical nonlinear crystal. The QPM period, i.e., $\Lambda = 2L_c$, can be designed for phase matching at any desired temperature.

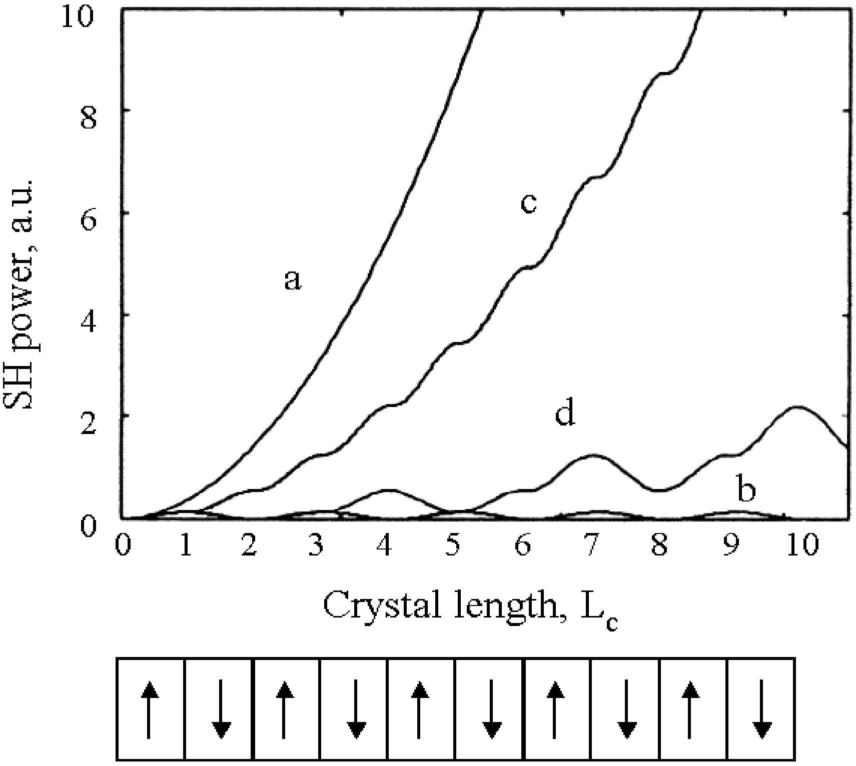

Fig. 3.2 The effect of different kinds of phasematching on the growth of the SH signal with distance in a nonlinear crystal: Curve a: Perfectly phasematched; curve b: Periodic growth and decay of the SHG for a non-phasematched process; curve c: First order QPM; curve d: Third-order QPM[2].

3.2. High-order QPM and the effect of the duty cycle

In a QPM, structure, an artificially engineered spatial modulation of the nonlinear coefficient *d* is used to compensate for the phase-velocity mismatch between the interacting waves. By a Fourier expansion of the spatial distribution of the *d*-coefficient, the periodic nonlinear coefficient for the QPM interaction can be written as[3]:

$$d(x) = d_{il} \sum_{m=\infty}^{\infty} G_m \exp(ik_{mQ}x) \qquad (3\text{-}1)$$

where d_{il} is the material nonlinear coefficient, G_m is the Fourier coefficient of the *mth* harmonic, and the *m*th-harmonic grating wave vector is defined as:

$$k_{mQ} = \frac{2\pi m}{\Lambda} \qquad m = 1, 2, 3... \qquad (3\text{-}2)$$

Here, Λ is the period of the modulated structure.

Then, the Fourier amplitude of the *m*th spatial harmonic of the distribution is given by:

$$d_{eff} = d_{il} G_m \qquad (3\text{-}3)$$

When the sign of the nonlinear coefficient is periodically modulated, the *mth* Fourier coefficient is equal to:

$$G_m = \frac{2}{m\pi}\sin(m\pi D) \tag{3-4}$$

where D is the duty cycle, which is determined by the ratio of the reversed domain length and the structure period Λ. At the optimum D, the sine factor is equal to unity, viz:

$$d_{eff} = \frac{2}{m\pi} d_{il} \tag{3-5}$$

If the duty cycle deviates from the optimum value, the effective nonlinear coefficient will decrease. Fig. 3.3 shows the dependence of the effective nonlinear coefficient on the duty cycle for m = 1, 2, 3.

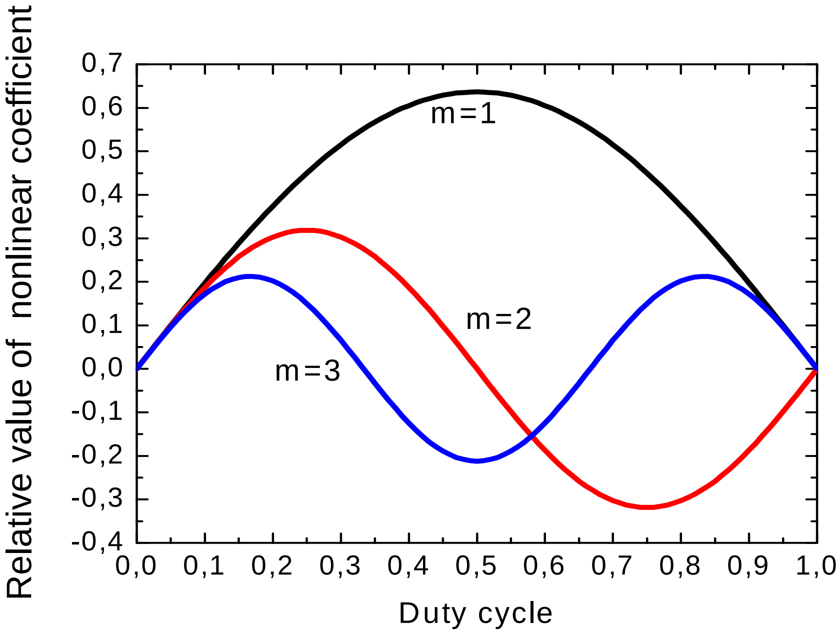

Fig. 3.3 The variation of the relative nonlinear coefficient as a function of the duty cycle, D, for a first-order (m = 1), a second-order (m = 2) and a third-order (m = 3) QPM interaction.

For the first-order QPM, the highest SH conversion is obtained for a duty cycle of 0.5, whereas for second-order QPM, it is found at $D = 0.25$. Of course, higher-order process are always less efficient and the conversion efficiency is more and more sensitive to the variation in the duty cycle, compared to the first-order, as can be seen in Fig. 3.3.

3.3. Fabrication methods of QPM structures

In principle, a QPM device can be achieved as long as one can flip the sign of the nonlinear coefficient in the neighbour ‘material slice’. This means, one does not have to bother if the material has a small or no birefringence at all. Instead, other material parameters, such as the transparency range, nonlinear coefficient, the optical damage threshold should be considered when making a QPM structure for high conversion efficiency and high power application.

In 1963, Franken and Ward[4] demonstrated for the first time QPM by stacking several quartz plates which were oriented in such a way that each consecutive plate was rotated 180° relative to the previous one thereby altering the sign of the nonlinearity. Gordon *et al*[5] used the same approach to double the frequency of a CO_2 laser, but employed a bonded stack of GaAs. This technique is successful for frequency doubling of long infrared wavelengths, where a rather long coherence length in the range of around 100 μm is needed. However, it has not been practical in order to make thinner plates to generate shorter wavelengths when the coherence lengths are in the few micrometer range. Recently, a QPM process for GaAs has been developed by using orientation patterning[6]. QPM-based DFG and OPO were demonstrated in the near infrared spectrum based on this technique.

Many attempts to engineer domains in ferroelectrics for QPM have been made during the last two decades. In the 1980's, Chinese researchers fabricated periodic ferroelectric domain structures in $LiNbO_3$ and $LiTaO_3$ during the Czochralski crystal growth. In their method, the spontaneous polarization was reversed by yttrium-doping[7,8,9]. Domain periods as small as 2 - 15 μm could be fabricated in this way[10]. The problem with this method is the temperature fluctuations during the crystal growth which make the domain size vary and, therefore, accumulated phase errors are grown into the structure which, in turn limits the effective structure length. Periodic domain structures were also produced in $LiNbO_3$ using a laser-heated pedestal growth technique. Domain structures down to 2 μm were obtained and used for blue-light generation at 407 nm[11]. The thermoelectric potential generated by the temperature gradients was responsible for the polarization reversal. However, this method also suffered from built-in phase errors and was mostly used for growing small-size crystals and, hence, a bit impractical.

For $LiNbO_3$, Miyazawa had observed that in the fabrication of Ti-indiffused waveguides, domain inversion could occur at the c^+-side of c-cut samples under special processing conditions[12]. It was believed that the domain inversion was due to the different composition gradient for the Ti-diffused and the pure regions in $LiNbO_3$ in combination with the heat treatment. Based on this observation, Webjörn *et al,* developed techniques to make periodic domain structures in the surface layer of $LiNbO_3$. They fabricated a periodically-poled domain-inverted channel waveguide in a 7 mm- long sample. It was used for first-order QPM SHG at 532 nm[13]. In a following experiment, they fabricated a first-order domain structure in $LiNbO_3$ for blue light generation[14]. Also, proton-exchange, in combination with heat treatment in $LiNbO_3$ and $LiTaO_3$, can induce the domain inversion. A 3.2 μm period grating was fabricated for first-order blue generation in $LiNbO_3$ and $LiTaO_3$[15]. In KTP, periodic polarization reversal was first demonstrated by ion exchange with Rb^+/Ba^{2+}. In this method, the KTP was immersed in a $RbNbO_3/Ba(NO_3)_2$ molten salt bath in which Rb^+ will replace K^+ at temperatures of 330-360°C for 45-90 minutes[16,17]. Waveguides with periodically inverted domains have been engineered on both hydrothermal and flux-grown KTP substrates[16,17] and relatively efficient blue light was generated[18,19].

Electron bombardment of $LiNbO_3$ and $LiTaO_3$ can also lead to a polarization reversal[20,21]. Therefore, electron beam writing was developed to write domain structures in $LiNbO_3$, $LiTaO_3$ and in KTP[22,23,24,25]. The problem with this technique is, however, an inhomogeneous distribution of the field strength in the crystal bulk which cause domain broadening.

Today, the most common technique to fabricate QPM structures is by electric-field poling. In this technique, a pulsed electric field of strength higher than the coercive field, is applied to a periodically patterned crystal. Yamada *et al.* was the first to demonstrate this method for poling of bulk $LiNbO_3$ at room temperature[26]. In this experiment, a 100 μm-thick crystal, was patterned with a metal electrode with a period of 2.8 μm. It was used for blue-light generation. Webjörn *et al* developed a liquid electrode method for poling of $LiNbO_{3,}$ where the electric contact was made with the electrolyte LiCl[27]. Miller *et al* adopted this method and poled a 53 mm-long, 0.5 mm-thick sample with a period of 6.5 μm for single-pass, CW frequency doubling of a 6.5 W Nd:YAG laser at 1064 nm. A maximum conversion efficiency of 42 % was achieved[28]. Many efforts have been made on poling of KTP and its isomorphs. For example, Chen and Risk developed an in-situ SHG monitoring method for poling hydrothermal KTP at approximately 2 kV/mm[29,30]. Flux-grown KTP is available in larger size and is considerably less expensive. However, it is more difficult to pole it due to a high ionic conductivity. To be able to pole flux-grown KTP in a controlled way, the conductivity has to be reduced. Two different methods for accomplishing this have been developed: In Karlsson and Laurell's method, KTP was exchanged in pure $RbNO_3$ to create a thin, low-conductive layer on the polar faces, followed by the electric-field poling at room temperature[31]. Rosenman used a low-temperature poling technique. Here, the mobile K^+ ions are frozen in the lattice[32]. Both of these techniques can give high quality periodic structures for efficient frequency doubling of Nd:YAG laser at 1064 nm[33] (Paper I). Poling of flux-grown RTP[34], RTA[35] and KTA[36] has also been investigated. However, since these materials have a lower commercial availability, fewer studies have been done.

In this thesis, flux-grown KTP has been the primary material for our studies. However, flux-grown RKTP was also investigated in one case (Paper VII). This new material clearly seems to be a potential alternative to KTP for making QPM structures at room temperature. Moreover, in my study, an in-situ SHG monitoring method was developed, which leads to a better control of the poling process which is important for crystals from the KTP family.

3.4. The advantages of QPM

The main advantage of QPM for SHG applications is that the phasematching can be achieved for any combination of input and output wavelengths in the transparency window of the material at any temperature by a correct choice of the period of the domain inversion. Hence, a QPM grating can be flexibly engineered for sophisticated structures such as chirped gratings for doubling of ultrashort pulses[37]; consecutive gratings for sequential processes or a combination of other mixing processes, such as SFG to generate multiple signals simultaneously[38]; multiple gratings which are placed beside each other[39] and, finally, the fan-out gratings[40] for the enhancement of the tuning range of an OPO.

QPM is unique because it allows a free choice of polarization of the interacting light waves, permitting efficient nonlinear interaction between waves that all have the same polarization using the largest diagonal component of the nonlinear susceptibility tensor. Furthermore, QPM is well suited for noncritical phasematching, and, thereby, spatial walk-off can be avoided which leads to better beam quality. The combination of a higher nonlinearity and a noncritical phasematching geometry results in very efficient crystals that can be used in a variety of applications. Type-II QPM has sometimes advantages despite that it utilizes the smaller nonlinear coefficient, for instance, to generate the orthogonally polarized signal and idler photons with a degenerate OPO for quantum optics investigations.

A periodic modulation of the nonlinear optical coefficients also leads to a periodic modulation of the electro-optic coefficients, which, among other things, reduces the sensitivity of the photorefractive effect, which is detrimental to the performance of nonlinear devices in general in terms of power, efficiency, and beam quality [41]. Moreover, it can be used in QPM electro-optic Bragg modulators where the Bragg reflectivity is electrically adjustable[42].

References of Chapter 3

[1] J. A. Armstrong, N. Bloembergen, J. Ducuing and P. S. Perhsan, Phys. Rev.**127**, 1918 (1962).

[2] F. Laurell, Optical material **11**, 235 (1999).

[3] M. M. Fejer, G. A. Magel, D. H. Jundt, and R. L. Byer, IEEE J. Quantum Electron. **28**, 2631 (1992).

[4] P. A. Franken and J. F. Ward, Rev. Mod. Phys. **35**, 23 (1963).

[5] L. Gordon, G. L. Woods, R. C. Eckardt, R. R. Route, R. S. Feigelson, M. M. Fejer and R. L. Byer, Electron. Lett. **29**, 1942 (1993).

[6] M. J. Angell, R. M. Emerson, J. L. Hoyt, J. F. Gibbons, L. A. Eyres, M. L. Bortz and M. M. Fejer, Appl. Phys. Lett. **64**, 3107, (1994) .

[7] D. Feng, N. B. Ming, J. F. Hong, J. S. Yang, J. S. Zhu, Z. Yang and Y. N. Wang, Appl. Phys. Lett. **37**, 607 (1980).

[8] N. B. Ming, J. F. Hong, and D. Feng, J. Mater. Sci. **17**, 1663 (1982).

[9] W. Wang, Q. Zhou, Z. Geng, and D. Feng, J. Crystal Growth **79**, 706 (1986).

[10] Y. L. Lu, L. Mao, S. D. Cheng, N. B. Ming, and T. Y. Lu, Appl. Phys. Lett. **59**, 516 (1996).

[11] G. A. Magel, M. M. Fejer and R L Byer, Appl. Phys. Lett. **56**, 208 (1990).

[12] S. Miyazawa, J. Appl. Phys. **50**, 4599 (1979).

[13] J. Webjörn, F. Laurell and G. Arvidsson, J. Lightwave Technol. **7**, 1597 (1989).

[14] J. Webjörn, F. Laurell and G. Arvidsson, IEEE Photon. Technol. Lett. **1**, 316 (1989).

[15] S. Makio, F. Nitanda, K. Ito and M. Sato, Appl. Phys. Lett. **61**, 3077 (1992).

[16] J. D. Bierlein, D. B. Laubacher, J. B. Brown, and C. J. van der Poel, Appl. Phys. Lett. **56**, 1725 (1990).

[17] C. J. van de Poel, J. D. Bierlein, J. B. Brown, and S. Colak, Appl. Phys. Lett. **57** 2074, (1990).

[18] F. Laurell, M. G. Roelsfs, W. Bindloss, H. Hsiung, A. Suna and J. D. Bierlein, J. Appl. Phys. **71**, 4664 (1992).

[19] D. Eger, M. Oron and M.Katz, J. Appl. Phys. **74**, 4298 (1993).

[20] R. W. Keys, A. Loni, R. M De La Rue, C. N. Ironside, J. H. Marsh, B. J. Luff, and P. D. Townsend, Electron Lett. **26**, 188 (1990).

[21] M. Yamada and K. Kishima, Electron. Lett. **28**, 721 (1992).

[22] H. Ito, C. Takyu and H. Inaba, Electron. Lett. **27**, 1221 (1991).

[23] Alan C. G. Nutt, V. Gopalan and M. Gupta, Appl. Phys. Lett. **60**, 2829 (1992).

[24] Wei-Yung Hsu and M. Gupta, Appl. Phys. Lett. **60**, 1 (1992).

[25] M. Gupta, W. P. Risk. Alan C. G. Nutt and S. D. Lau, Appl Phys. Lett. **63**, 1167 (1993).

[26] M. Yamada, N. Nada, M. Saitoh, and K. Watanabe, Appl Phys. Lett. **62**, 435 (1993).

[27] J. Webjörn, V. Pruneri, P. St. J. Russell, J. R. M. Barr, and D. C. Hanna, Electron. Lett. **30**, 894 (1994).

[28] G. D. Miller, R. G. Batchko, W. M. Tulloch, D. R. Weise, M. M. Fejer and R. L. Byer, Opt. Lett. **22**, 1834, (1997).

[29] Q. Chen and W. P. Risk, Electron. Lett. **30**, 1516 (1994).

[30] Q. Chen and W. P. Risk, Electron. Lett. **32**, 107 (1996).

[31] H. Karlsson and F. Laurell, Appl. Phys. Lett. **71**, 3474 (1997).

[32] G. Rosenman, S. Skliar, D. Eger, M. Oror, and M. Katz, Appl. Phys. Lett. **73**, 3650 (1998).

[33] A. Arie, G. Rosenman, V. Mahal, A. Skliar, M. Oron, M. Katz, and D. Eger, Optics Commun. **142**, 265 (1997).

[34] H. Karlsson and F. Laurell, Appl. Phys. Lett. **74**, 1519 (1999).

[35] H. Karlsson, M. Olson, G. Arvidsson, F. Laurell, U. Bäder, A. Borsutzky, R. Wallenstein, S. Wickström, M. Gustafsson, Opt. Lett. **24**, 330 (1999).

[36] G. Rosenman, A. Skliar, Y. Findling, P. Urenski, A. Englander, J. Phys. D: Appl. Phys. **32**, L49 (1999).

[37] B. Agate, E. U. Rafailov, W. Sibbett, S. M. Saltiel, K. Koynov, M. Tiihonen, S. Wang, F. Laurell, P. Battle, T. Fry, T. Roberts, E. Noonan, IEEE J. of Selected Topics in Quantum Electronics **10**, 1268 (2004).

[38] J. Nordborg and H. Karlsson, Euro Photonics **June/July**, 28 (2004).

[39] L. E. Myer, R. C. Eckardt, M. M. Fejer, R. L. Byer, and W. R. Bosenberg, Opt. Lett. **21**, 591 (1996).

[40] P. E. Powers, T. J. Kulp, and E. Bisson, Opt. Lett. **23**, 159 (1998).

[41] M. Taya, M. C. Bashaw, M. M. Fejer, Opt. Lett. **21**, 857 (1996).

[42] C. Canalias, V. Pasiskevicius, R. Clemens and F. Laurell, Appl. Phys. Lett. **82**, 4233 (2003).

4. Quasi-phasematched second-harmonic generator

4.1. Type-I and type-II quasi-phasematched second-harmonic generation

When all the wave vectors are collinear with the grating vector, the wave-vector mismatch for QPM SHG is:

$$\Delta k_Q = k_{SH} - 2k_F - k_{mQ} \tag{4-1}$$

where the *m*th-harmonic grating wave vector is $k_{mQ} = 2m\pi / \Lambda$, defined in Eq (3-2).

When the SH and the fundamental waves are quasi-phasematched, i.e., $\Delta k_Q = 0$, the grating period can be deduced as:

$$\Lambda = \frac{2m\pi}{k_{SH} - 2k_F} = \frac{m\lambda_F}{2(n_{SH} - n_F)} \qquad m = 1, 2, 3... \tag{4-2}$$

There are two types of quasi-phasematching in second-harmonic generation, depending on the two possible orientations for the linear polarization vectors of the incident beams. In the type-I process, both polarization vectors are parallel whereas in the type-II process, the polarization vectors are orthogonal.

In the type-I QPM SHG process, the largest nonlinear coefficient, d_{33} for KTP and its isomorphs, can be utilized when the polarization of the fundamental electric field is chosen to be parallel to the direction of the polar axis of the crystal (z-direction). Consequently, the polarization of the second-harmonic wave is also parallel to the polar axis. The process is then $E_F^z E_F^z \to E_{SH}^z$. The grating period for this type of quasi-phasematching for the *m*th order frequency doubling is given by:

$$\Lambda^I = \frac{m\lambda_F}{2(n_{SH}^z - n_F^z)} \tag{4-3}$$

Here, n_F^z and n_{SH}^z are the refractive indices along the z-axis of the crystal for the fundamental and the SH waves.

Type-II SHG in PPKTP is realized by employing the d_{24} nonlinear coefficient for a z-cut, x-propagation direction. Here, two orthogonal fundamental components are used to generate a second-harmonic wave that is polarized perpendicular to the polar axis (y-axis), i.e., the process is $E_F^y E_F^z \to E_{SH}^y$. In this case, the grating period is calculated by replacing n_F^z in Eq (4-3) by $(n_F^z + n_F^y)/2$, viz:

$$\Lambda^{II} = \frac{m\lambda_F}{(2n_{SH}^y - n_F^z - n_F^y)} \qquad (4\text{-}4)$$

Here, n_F^y and n_{SH}^y are the refractive indices along the y-axis of the crystal for the fundamental and the SH waves, respectively.

The grating periods for type-I and type-II of the first-order ($m = 1$) collinear QPM SHG, shown in Fig. 4.1, are calculated for flux-grown KTP by using the Sellmeier equation from Fan[1].

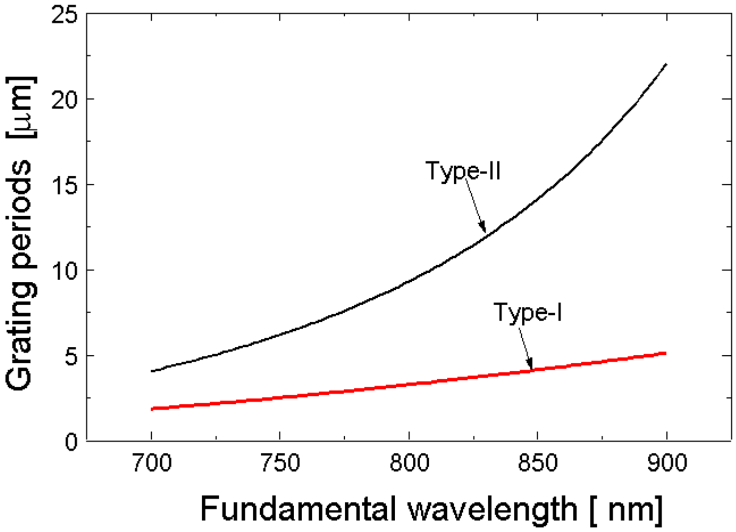

Fig. 4.1 First-order grating periods as a function of the fundamental wavelength for type-I and type-II QPM SHG.

In the UV region, the dispersion of the KTP material increases rapidly, which makes the first-order grating period very small for type-I QPM SHG, and thus brings on difficulties in fabricating components. On the other hand, we noted that in the fundamental spectral region from 700 nm to 900 nm, for the same order QPM at a fixed wavelength, the grating period for type-II QPM SHG is several times larger than for type-I QPM SHG. Obviously, we can conclude that one of the advantages of type-II QPM SHG over type-I QPM SHG is that the fabrication difficulties are considerably reduced in the short wavelength region due to that fact that the coherence length increases substantially in the type-II process. This has also been seen experimentally (Paper III).

In Paper III, we generated UV light at approximately the same wavelengths from two PPKTP crystals, having approximately 3-time the difference in the grating period, by utilizing type-I and type-II QPM SHG, respectively. Fig. 4.2a shows the homogeneity of the SH signal generated at 398.8 nm with the type-II configuration from PPKTP having a period of 9.01 μm. The SH signal was almost constant over the entire thickness of the crystals which is a sign of homogeneous poling. As a comparison, curve b is a vertical scan of the other PPKTP crystal with a 2.95 μm period used for first-order type-I generation at 390 nm. In this case, the SH power varied more than 50% within half the thickness of the crystal. The poor uniformity in this case has been attributed to the difficulty in fabricating narrow and deep domains.

However, we should realize that type-II QPM SHG is a much less efficient process compared to type-I since the d_{24} nonlinear coefficient is several times smaller than d_{33}. (For KTP, $d_{24} = 3.64\ pm/V$, $d_{33} = 16.9\ pm/V$)[2].

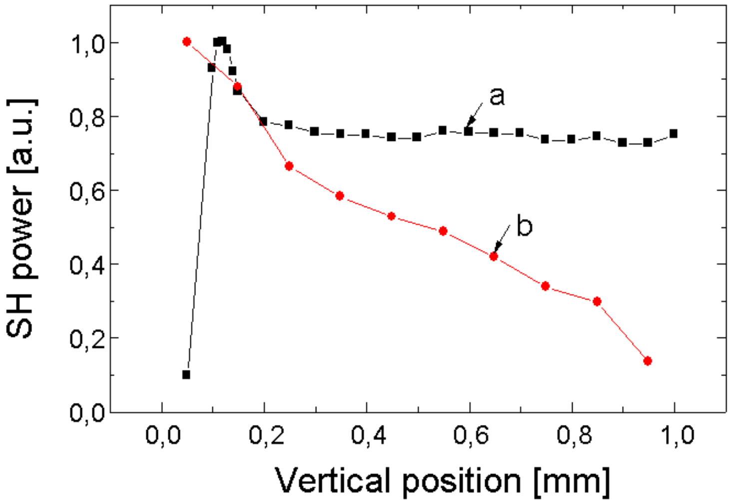

Fig. 4.2 Variation of the SH power with the vertical position for two PPKTP crystals used for UV generation. Curve a shows a 9.01 μm sample for first-order type-II UV generation at 398.8 nm. The first point is measured at the very top surface where the fundamental beam was cut and, therefore, a lower SHG power is measured. Curve b shows a 2.95 μm sample for first order type-I UV generation at 390 nm.

4.2. Phasematching tolerances

The phasematching is sensitive to many parameters, such as the wavelength, temperature and the polarization of the interacting waves. The phasematching tolerance, also called the acceptance bandwidth, is commonly defined as the relative change in the parameter that causes an output power to drop to half of the maximum value. For a device of total length L containing uniform periods, the phasematching factor is $\sin c^2(\Delta kL/2)$, which is given in Eq (2-15). The full width at half maximum acceptance bandwidth is then satisfied by the following expression:

$$\frac{\Delta kL}{2} = 0.4429\pi \tag{4-5}$$

Expanding Δk as a function of wavelength or temperature, and neglecting the second derivative terms, we can find the wavelength acceptance bandwidth and the temperature acceptance bandwidth, respectively, which will be shown below.

4.2.1. Wavelength acceptance bandwidth

The wavelength acceptance bandwidth for a nonlinear process is an important parameter because it gives us information on the linewidth limitation we will expect of the fundamental laser source. For a uniform grating, the wavelength acceptance bandwidth is given by[3]:

$$\Delta\lambda_{FWHM} = \frac{0.4429\lambda}{L}\left|\frac{n_{SH} - n_F}{\lambda} + \frac{\partial n_F}{\partial \lambda} - \frac{1}{2}\frac{\partial n_{SH}}{\partial \lambda}\right|^{-1} \tag{4-6}$$

The acceptance bandwidth for type-II QPM SHG is considerably wider than for type-I as can be seen in Fig. 4.3.

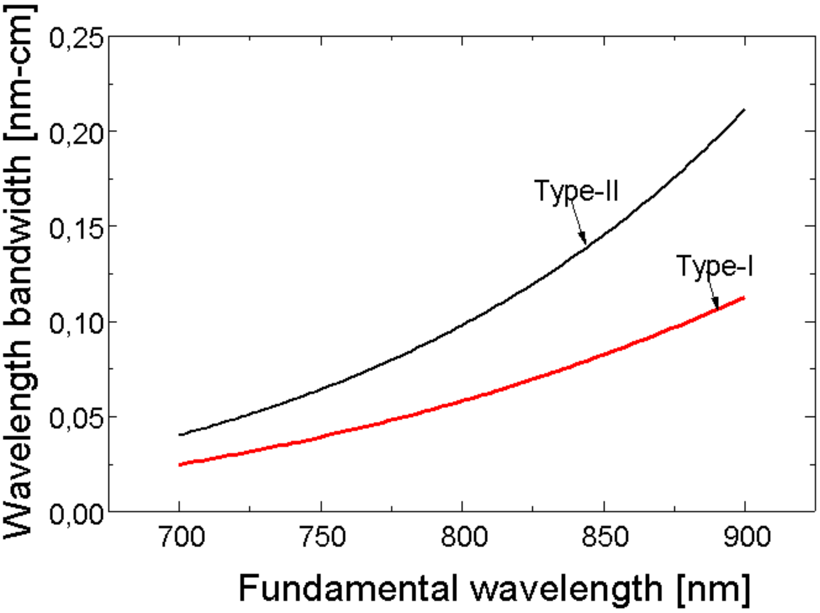

Fig. 4.3 Calculated wavelength bandwidth as a function of the fundamental wavelength for type-I and type-II QPM SHG.

4.2.2. Temperature acceptance bandwidth

The temperature tuning characteristics of the nonlinear interaction is very important too. First of all, the phasematching wavelength can be adjusted by changing the crystal temperature in order to match it to a light source with a fixed wavelength, such as one of the many solid-state lasers. Moreover, the temperature tuning characteristic for SHG can also provide information about the uniformity of the QPM structure, i.e., it serves as a quality measure for the poling process. For a fixed wavelength, the temperature bandwidth can be expressed as[3]:

$$\Delta T_{FWHM} = \frac{0.4429\lambda_F}{L}\left|\left.\frac{\partial n_{SH}}{\partial T}\right|_{T_0} - \left.\frac{\partial n_F}{\partial T}\right|_{T_0} + \alpha\left(n_{SH} - n_F\right)\right|^{-1} \tag{4-7}$$

where α is the thermal expansion coefficient. The value of α for KTP is given by Bierlein *et al*[4]. The derivatives of the refractive indices with temperature, at the fundamental and the SH wavelengths, are calculated for a particular phasematching temperature, T_0. The best fit function for the experimentally derived values for KTP has been given by Wiechmann[5]. The thermal bandwidths increase toward longer wavelengths, which is expected due to the lower material dispersion. As in the case of wavelength acceptance bandwidth, the temperature acceptance bandwidth is wider for type-II compared to type-I interactions in QPM SHG.

4.2.3. *Effective crystal length*

Missing domains is one of the most common defects to appear in QPM structures fabricated by electric-field poling. When it happens, the effective interaction length will be reduced. Eq (4-6) and Eq (4-7) tell that the effective crystal length of the PP crystals is reciprocal to the wavelength or the temperature acceptance bandwidth. By measuring the bandwidth, the effective crystal length, L_{eff} , can be estimated. A specific crystal is poled with expected good quality if the effective crystal length is comparable with the physical one.

4.3. *Single-pass SHG in the low conversion efficiency regime*

Single-pass CW SHG is the simplest nonlinear frequency conversion approach to generate UV and visible light from available laser sources. As an example, Fig. 4.4 shows the experimental set-up, in which the fundamental light is focused into a nonlinear crystal. The combination of the λ/2 wave plate and the polarizer has two functions: 1) it allows adjustment of the fundamental power and 2) it keeps the right polarization of the fundamental wave for proper quasi-phasematching.

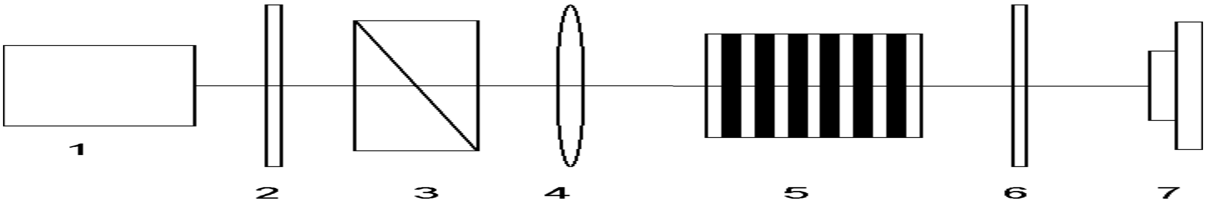

Fig. 4.4 Single-pass, second-harmonic generation set-up: 1: Pump laser; 2: Half-wave plate; 3: Polarizer; 4: Lens; 5: Nonlinear crystal; 6: Filter; and 7: Power/energy meter.

For a Gaussian beam, the conversion efficiency is obtained by rewriting Eq (2-16):

$$\eta = \frac{P_{SH}}{P_F} = \left(\frac{2\omega_F^2 d_{eff}^2 k_F P_F}{\pi n_F^2 n_{SH} \varepsilon_0 c^3} \right) L h(B, \xi) \qquad (4\text{-}8)$$

It can be seen that from this the conversion efficiency increases linearly with the fundamental power and the crystal length. In Fig. 4.5, we show the measured efficiency of frequency doubling of a CW Nd:YAG at 1064 nm, with a 9 mm-long PPKTP sample. The measured conversion efficiency fits very well with a linear function here in the low power regime.

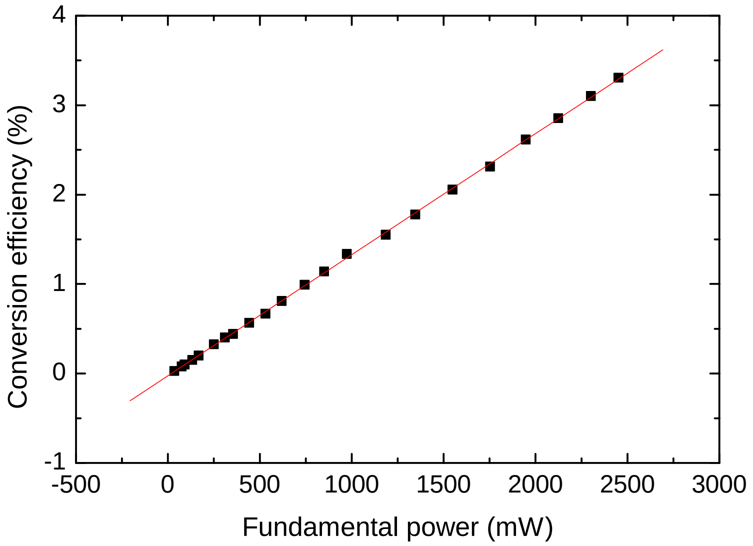

Fig. 4.5 The SHG conversion efficiency as a function of the fundamental power for a 9 mm-long PPKTP crystal with period of 9.01 μm. Solid square is the measured data and the line is a linear fit.

To be able to increase the conversion efficiency in QPM SHG, one might easily draw the straightforward conclusion from Eq (4-8) that a longer crystal in single-pass CW operation should be employed. However, there are reasons why this approach might not be valid or practical. Firstly, the crystals used have a limited length, which varies depending on the material and the growth technique. For flux-grown KTP z-plates, the typical size is 30 x 30-mm^2. It is even smaller for hydrothermal KTP. Secondly, it is still difficult to fabricate fine-pitch domain gratings of high qualities over very long lengths, at least in crystals from the KTP family. Moreover, as the crystal length increases, the SHG become more sensitive to the changes in temperature, wavelength and the refractive index variations over the substrate.

To be able to compare the conversion efficiency for different materials and experimental conditions, it has been common to compare the results with those of a standard crystal length and power. This normalized conversion efficiency refers to an input fundamental power of 1 Watt and a crystal length of 1 cm, with unit of, %/W·cm. It is written as:

$$\eta_{norm} = \frac{P_{SH}}{P_F^2 L} = \left(\frac{2\omega_F^2 d_{eff}^2 k_F}{\pi n_F^2 n_{SH} \varepsilon_0 c^3} \right) h(B,\xi) \tag{4-9}$$

For an optimal confocal focusing, $h(0, 2.84) = 1.07$, the theoretical normalized conversion efficiency is wavelength dependant for a given nonlinear material. In our single-pass, type-I CW SHG experiments, the maximum normalized conversion efficiency 1.7 %/(W·cm) and 2.5 %/(W·cm) were obtained for doubling a CW Nd:YAG at 1064 nm with PPKTP (Paper I) and a CW Ti:Sapphire at 908 nm with PPRKTP (Paper VII), respectively. These two figures are very close to the theoretical values.

Single-pass, type-II SHG was also studied in the low conversion regime using a Ti:Sapphire laser as the fundamental input source (Paper III). The d_{24} nonlinear coefficient was utilized for the interaction. The laser beam was launched along the crystal's x–axis and the polarization of the fundamental beam was adjusted to 45^o relative to the z-axis to give the type-II interaction. 0.44 mW of UV radiation (398.8 nm) was generated from 780 mW of input power with a 8.5 mm-long crystal, which corresponds to a normalized conversion efficiency of 0.09 %/(W·cm).

4.4. Single-pass SHG with pump depletion using pulsed lasers

In many applications, such as micro-machining and range-finding, pulsed lasers are needed. Then the laser's peak power is high even though the average power is low or moderately high. Thereby the conversion efficiency is enhanced considerably. In this case, the pump depletion needs to be taken into account even for a single-pass configuration.

Let us assume that we have phasematching, i.e., $\Delta k_Q = 0$, and quasi-monochromatic fields, then the second-harmonic generation efficiency for a depleted fundamental wave is given by[6]:

$$\eta_{SH} = \frac{\overline{P}_{SH}}{\overline{P}_F} = \tanh^2\left[\left(\gamma'_{SH}\overline{P}_F\right)^{1/2}\right] \tag{4-10}$$

where $\overline{P}_{SH}$ and $\overline{P}_F$ are the average power of the second-harmonic and the fundamental waves, respectively, and γ'_{SH} is the nonlinear coefficient for a train of short pulses.

In the case of SHG with nanosecond or picosecond pulses, we can assume that the group-velocity dispersion (GVD) and the self-phase modulation (SPM) within the crystal can be neglected. Then, for a temporally Gaussian shape pulse, γ'_{SH}, is given by:[7]

$$\gamma'_{SH} = \gamma_{SH}\left[\left(\frac{2\ln 2}{\pi}\right)^{1/2}\right]\frac{1}{\tau f} \tag{4-11}$$

where τ is the full-width at half maximum (FWHM) pulse duration and f is the pulse repetition rate. $\gamma_{SH} = \eta_{norm}L$, is the coefficient for the CW case without pump depletion [see Eq (4-9)].

We should note that in Eq (4-11), only the fundamental pump depletion is considered. However, for KTP, absorption in the visible is a non-negligible effect and, at high conversion rates, a considerable amount of the SH radiation is absorbed which lowers the conversion efficiency. This was observed in our experiments. Therefore, the maximum efficiency predicted in theory can only be achieved in a perfectly non-absorbing crystal.

In our investigation, high conversion-efficiency experiments were conducted with a mode-locked and Q-switched Nd:YAG laser using PPKTP for 532 nm generation. Fig. 4.6 shows the dependence of the conversion efficiency on the average fundamental power for the case of 100 ps-long pulses at a repetition rate of 100 MHz. The crystal length was 9 mm. A maximum average SH power of 1.34 W and a conversion efficiency of 63 % were obtained (Paper I). The solid line is the theoretical conversion efficiency in which the depletion of the fundamental wave was taken into account. At lower fundamental power, the theoretical simulation fits well with the measured data, whereas at a fundamental average power higher than about 1.5 W, the saturation of the conversion efficiency, due to the absorption of the SH radiation, was observed.

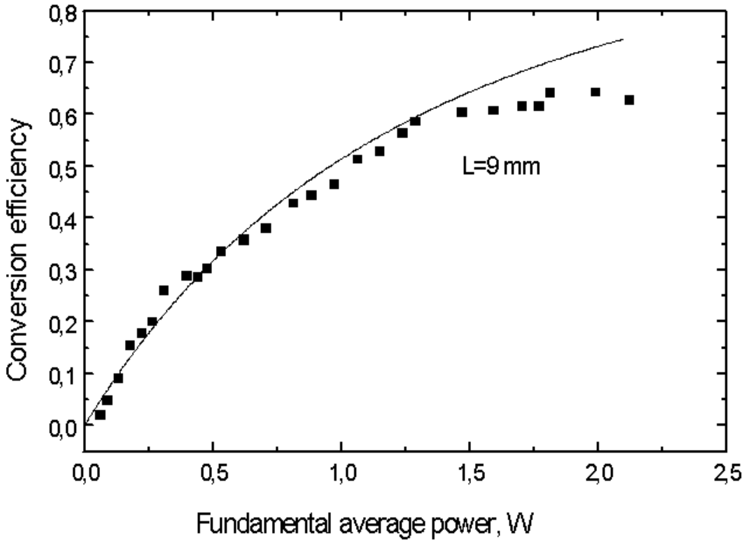

Fig. 4.6 The conversion efficiency as a function of the average fundamental power for a mode-locked Nd:YAG laser. The solid line is a theoretical fit calculated by taking the fundamental beam depletion into account (Paper I).

For frequency doubling of Q-switched Nd:YAG lasers, different repetition rates and pulse lengths in the ns regime have been used for efficiency measurements on two different samples. As shown in Fig. 4.7, the highest efficiency obtained was 74 % in a 3 mm-long PPKTP at a 20 Hz repetition rate and with 5 ns long pulses (Paper B).

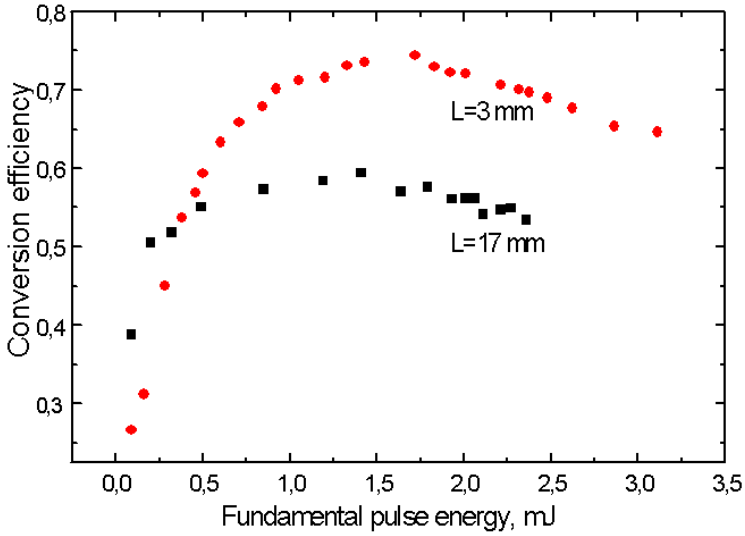

Fig. 4.7 Frequency doubling efficiency at two different crystal lengths as a function of the fundamental pulse energy of a Q-switched Nd:YAG laser with a 5 ns-long pulse and a 20 Hz repetition rate (Paper B).

A strong saturation effect and, actually, a decrease in the conversion efficiency was observed for an increase of the input energy. This cannot be explained by the depletion of the fundamental power only. However, it may quantitatively be explained by the absorption in the rear part of the crystal where the SH power has built up to a higher value than in the rest of the crystal. This absorption leads to heating of the crystal and, consequently, a detuning from phasematching. Fig. 4.7 shows the conversion efficiency as a function of the pulse energy for a 5 ns-long pulse at 20 Hz for two different crystal lengths. The higher efficiency obtained for the shorter crystal demonstrates clearly that the thermal effect caused by the absorption of the SH signal is much stronger in the longer crystal. The absorption of the generated green light in the crystal leads to thermal gradients as well as to thermally-induced stress. We will discuss thermal contribution to the optical damage in more detail in Chapter 7.

4.5. SHG using ultrashort pulses

Here, we discuss the second-harmonic generation with femtosecond pulses because this temporal regime has several properties different from those of the SHG with picosecond or nanosecond pulses. Specifically, we have to consider the group–velocity mismatch (GVM) and the group-velocity dispersion (GVD) in this process.

In principle, the GVM limits the effective interaction length in the nonlinear crystal. The group velocity of a pulse is generally different from the phase velocity. Therefore, even if the interaction is phasematched, i.e., $\Delta k = 0$, the fundamental and the harmonic pulses propagate with different group velocities. This leads to a spatial walk-off as they propagate through the nonlinear crystal. The group-velocity mismatch factor γ, is expressed as[8]:

$$\gamma = \frac{1}{c}\left(n_{SH} - n_F - \lambda_{SH}\frac{\partial n_{SH}}{\partial \lambda_{SH}} + \lambda_F \frac{\partial n_F}{\partial \lambda_F} \right) \qquad (4\text{-}12)$$

The influence of the group-velocity mismatch on the SHG efficiency depends on the ratio of the interaction length and the walk-off length, L_w, which is defined as:

$$L_w = \left(|\gamma| \Delta\omega_F \right)^{-1} \qquad (4\text{-}13)$$

where $\Delta\omega_F$ is the spectral width of the fundamental pulse. For a transform-limited fundamental pulse with duration τ_F, we have that

$$\tau_F \Delta\omega_F \approx 1 \qquad (4\text{-}14)$$

Thus, L_w can be written as:

$$L_w \approx \frac{\tau_F}{|\gamma|} \qquad (4\text{-}15)$$

When $L < L_w$, frequency doubling of short pulses takes place in the same way as under the condition of phase-velocity matching.

However, in most cases, $L > L_w$, due to the walk-off phenomenon, and the frequency doubling will be accompanied with a strong spreading of the SH pulse[9] and a spectral broadening. The duration of the SH pulse, τ_{SH}, depends on the crystal length, as expressed:

$$\tau_{SH} \approx |\gamma| L \tag{4-16}$$

There are two factors contributing to the spectral broadening. One is due to the phase mismatch, and the other one is the group-velocity walk-off. The overall SH spectral response is proportional to $\sin\left[0.5 L_{eff}\gamma(\omega-\omega_0)\right]/\left[0.5 L_{eff}\gamma(\omega-\omega_0)\right]$, where γ is the group-velocity mismatch factor, given by Eq (4-12), and L_{eff} is an effective crystal length deduced from CW characterization.

For fs SHG at a high fundamental peak intensity, the fundamental beam depletes quickly after a nonlinear interaction length, L_{NL}, which is defined as:

$$L_{NL} = \frac{2 n_F c}{\omega_F d_{eff} |E_F|} \tag{4-17}$$

where ω_0 is the fundamental central frequency and $|E|$ is the field amplitude of the fundamental pulse. At high peak intensity, ($\propto |E_F|^2$), the nonlinear interaction length is getting shorter, which will result in an intensity-dependent broadening of the QPM acceptance bandwidth.

Quantitatively, we have tested the PPKTP crystals for UV generation by frequency doubling of femtosecond pulses. In this experiment, the pump source was a Kerr-lens, mode-locked Ti:Sapphire laser, generating 100-fs long pulses at a 80-MHz repetition rate. The spectral bandwidth of the laser was approximately 10 nm at the fundamental wavelength of 780 nm. The crystal for this experiment has a period of 2.95 μm and a physical length of 9 mm. An effective crystal length of 5.6 mm was determined from the measured wavelength bandwidth of 0.09 nm using a CW Ti:sapphire laser (Paper II).

The characteristic walk-off length was calculated to be shorter than 57 μm. Due to walk-off, the SH pulse width is broadened to about 10 ps, which corresponds to the calculated value obtained from Eq (4-16) when the effective crystal length, instead of physical length is used. Fig. 4.8 shows the measured SH spectrum at two different pump intensities. The fundamental beam was focused to a 50 μm radius in the crystal. The solid curve corresponds to a fundamental peak intensity of 0.93 GW/cm^2. The calculated phasematching bandwidth was 0.18 nm which is very close to the measured figure of 0.2 nm, approximately two times broader than that in the CW case. A much larger bandwidth, 1.44 nm, was obtained at 3 GW/cm^2. At this intensity, the L_{NL} is 605 μm.

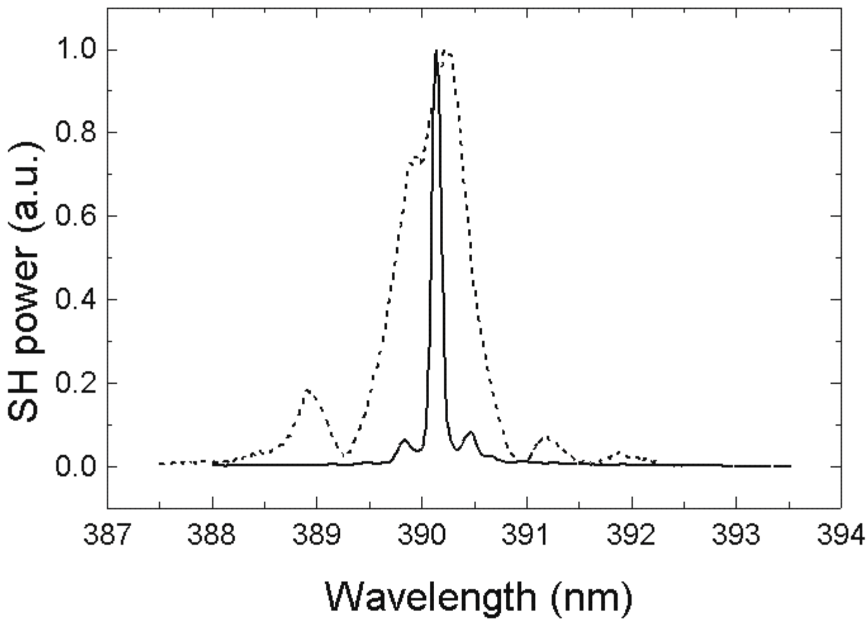

Fig. 4.8 SH spectra obtained by frequency doubling 100-fs optical pulses in PPKTP at two different fundamental intensities: solid curve: 0.93 GW/cm^2, dashed curve: 3 GW/cm^2.

GVD also produces a temporal spreading of the fundamental and the SH pulses due to the chirping of the spectral components. The dispersion length, L_d, is defined as[10]:

$$L_d = \frac{\tau_F^2}{2|k_2|} \tag{4-18}$$

where

$$k_2 = \frac{\partial^2 k}{\partial \omega^2} = \frac{\lambda_F^3}{2\pi c^2}\frac{\partial^2 n_F}{\partial \lambda_F^2} \tag{4-19}$$

It can be shown that the duration of a transform-limited Gaussian pulse in a dispersive medium grows with distance, x, in the following manner:

$$\tau_p = \tau_F\left[1+\left(\frac{x}{2L_d}\right)^2\right]^{1/2} \tag{4-20}$$

If the dispersion length is much longer than the crystal length, the pulse broadening due to dispersion is negligible. Fortunately, this is the case for our experiment described in Paper II.

References of Chapter 4

[1] T. Y. Fan, C. E. Huang, B. Q. Hu, R. C. Eckardt, Y. X. Fan, R. L. Byer and R. S. Feigelson, Appl. Opt. **26**, 2390 (1987).

[2] H. Vanherzeele and J. D. Bierlein, Opt. Lett. **17**, 982 (1992).

[3] M. M. Fejer, G. A. Magel D. H. Jundt and R. L. Byer, IEEE J. Quantum Electron. **28**, 2631 (1992).

[4] J. D. Bierlein and H. Vanherzeele, J. Opt. Soc. Am. B**6**, 622 (1989).

[5] W. Wiechmann, S. Kubota, T. Fukui and K. Masuda, Opt. Lett. **18**, 1208 (1993).

[6] A. Yariv, "Quanttum Electronics", **3rd ed.**, Wiley, New York (1989).

[7] S. D. Butterworth, S. Girard, and D. C. Hanna, J. Opt. Soc. Am. B **12**, 2158 (1995).

[8] S. A. Akhmanov, V. A. Vysloukh, and A. S. Chirkin, "Optics of Femtosecond Laser Pulses", American Institute of Physics, New York (1992).

[9] D. H. Auston and K. B. Eisenthal, "Ultrafast Phenomena IV", Springer, Berlin (1984).

[10] J. Zhang, J. Y. Huang, H. Wang, K. S. Wong and G. K. Wong, J. Opt. Soc. Am. B.**15**, 200 (1998).

5. KTP and Rb-doped KTP

5.1. *Why KTP and its isomorphs?*

In Chapter 4, several experiments on QPM SHG based on flux-grown KTP have been discussed. In this chapter, more of the material characteristics of the KTP-crystal family are given together with the motivation why I have chosen to study these crystals.

Among roughly 20,000 surveyed crystals only a few percent have a combination of an intrinsic nonlinearity and a sufficient birefringence for nonlinear optics[1]. Besides being nonlinear, there are many other requirements that have to be met for a material to be suitable for practical implementations. Some of the more important ones are:

- wide transparency range
- large size with good optical homogeneity
- chemical and mechanical stability
- low cost and easy fabrication

This reduces the number of candidates to only a few tens of crystals. Furthermore, if we look for the generation of visible and near UV radiation and restrict ourself to QPM, then, essentially, only three classes of ferroelectric crystals have been used with promising results. These are:

- **Lithium Niobate ($LiNbO_3$ or LN) and Lithium Tantalate ($LiTaO_3$ or LT)**
- **Potassium Niobate ($KNbO_3$ or KN)**
- **Potassium Titanyl Phosphate ($KTiOPO_4$ or KTP) and its isomorphics**

Let us now look at these in more detail. Congruent LN, (CLN) has been the most frequently studied material. It is transparent from 350 to 5,000 nm. The absorption is relatively weak and the material homogeneity within a given crystal, and between crystal to crystal is generally very good. The nonlinearity is high (d_{33} = 34.1 pm/V)[2], which allows a high conversion efficiency to be obtained. However, LN suffers from photorefractive damage when illuminated with visible radiation, which distorts the beam[3]. In addition, CLN has a coercive field as high as 21 kV/mm and, in practice, this limits the thickness of the samples to approximately 0.5 mm. Congruent LT (CLT) is an attractive one compared to CLN because the absorption edge of CLT extends further into the UV (280 nm). For example, periodically poled CLT with a period of 1.7 µm has been demonstrated for UV generation.[4,5]. However, this crystal also suffers from a high susceptibility to photorefractive damage. Several techniques have been used to improve the properties of CLN and CLT. The first one has been by doping the crystals with magnesium (MgO:CLN, MgO:CLT) where the prime motive is to reduce the photorefraction. The second one is making them lithium-rich, i.e., increase the stoichiometry (SLN, SLT), and the third one is based on a combination of the two, i.e., to make magnesium-doped stoichimetric crystals (MgO:SLN, MgO:SLT). In all cases, a positive aspect of the modification is the substantially reduced coercive field allowing for thicker crystals to be poled. For instance, the coercive fields are about 4.5 kV/mm[6], and 2 kV/mm[7] for MgO:CLN (5 mol%) and for MgO:SLN, respectively. And, similarly, approximately 1.7 kV/mm for both SLT[8] and for MgO:SLT[9]. However, although the photorefractive resistances have been improved dramatically for MgO:CLN[10], MgO:SLN[2,10], SLT and for MgO:SLT[2,11], the photorefractive damage thresholds are still too low for SHG-devices to be operated at room temperature. For pure SLN crystals, it exhibits even lower photorefractive damage resistance[11], than the CLN[10,12].

KN is an attractive crystal for making SHG-devices in the visible spectrum because of its high resistance to photorefractive damage[13] and the large nonlinear optical coefficient[14]. Furthermore, a low coercive field, 300-500 V/mm[13,15], makes it possible to pole rather thick crystals. Some of the problems with this crystal relates to the fabrication. It has been very difficult to grow defect-free single crystals as they often crack during cool-down after the growth. Furthermore, it has been difficult to grow single-domain crystals and it can even happen that samples will self-pole during handling, such as, cutting and polishing as well as during operation at high optical intensities. Altogether, this has somewhat limited the usage of KN in practice.

Let us now look at KTP as an alternative for making QPM devices. Besides its wide transparency, large nonlinear coefficient, low refractive index change with temperature[16], large thermal phasematching bandwidth, and high chemical and mechanical stability, probably the most important property of KTP is it´s orders of magnitude lower sensitivity to photorefractive damage[17] than LN. Furthermore, the coercive field of KTP is about one order of magnitude lower than that of CLN and, therefore, it is rather straightforward to pole thicker crystals, even with dense QPM gratings. Despite all the favourable properties of KTP, we should realize that KTP can suffer from photochromic damage when illuminated with intense visible or UV radiation. However, this effect, usually called grey tracking, does not cause permanent damage to the crystals[18]. Other crystals from the KTP family have very similar properties to those of KTP. The largest difference in this regard is for the arsenates, $RTiOAsO_4$ (RTA) and $KTiOAsO_4$ (KTA), where P has been exchanged with As, which results in a wider transparency limit in the IR.

Today, with the knowledge we have of these materials, it would be too much to say that one material is better than all the other. However, if we want an efficient crystal, for generating moderate power in the visible or the near UV spectrum, then KTP seems like a good candidate to fulfil the task. Hence, I chose KTP and its closest relative, i.e., Rb-doped KTP, RKTP, as the nonlinear optical material for my studies.

5.2. Crystal growth

KTP decomposes on melting at approximately 1,150-1,170 ^{o}C[16,19]. This inhibits the use of convenient melt-growth techniques, such as the Czochralski method, for growth of KTP. Instead, crystals from the KTP family are grown by the hydrothermal method[20] or the flux technique[21,22].

5.2.1. Hydrothermal method

In the hydrothermal process, nutrients and seed crystals are sealed in a platinum autoclave which can withstand high temperature, high pressure as well as being resistant to corrosive solvents. The crystal growth needs a constant pressure (20,000-25,000 psi) and a constant temperature (350 – 600 ^{o}C)[16]. High quality crystals, in terms of uniformity and low conductivity can be obtained with this technique. However, it is an expensive growth technique and it is also difficult to grow large crystals, which have limited the usage of hydrothermal KTP in practice.

5.2.2. Flux-grown method

Flux growth is a high-temperature solution technique to grow larger single crystals. In this procedure, the KTP crystallizes out of a molten flux composition when it is cooled down. For KTP, the growth temperature can be varied between 700 – 1,000 ^{o}C, depending on the flux used. Common fluxes employed are various potassium phosphates, with the K- to P-ratio varying from 1 to 3, and tungstates and halides[16]. If the flux contains only the constituents of the crystals, then, it is called as self-flux. To grow large crystals, a seed is needed. There are two methods to place it. One is called submerged seed solution growth i.e., SSSG, which gives a crystal with 14 growth sectors. The other one is termed top seeded solution growth, i.e., TSSG, which have 10 growth sectors.

Larger alkali ions can be doped into KTP to modify the dielectric property of the crystal. For example, Rb_xK_{1-x}KTP (with $x = 0 \rightarrow \sim 1$), RKTP, crystals could be synthesized in the flux-grown method by adding Rb^+-ions to the growth melt. When the K^+-ions is substituted completely by Rb^+ ($x = 1$), $RbTiOPO_4$ (RTP) is obtained.

An advantage of the flux-grown method is that it is relatively simple and that the process operates at atmospheric pressure without the need for sophisticated pressure equipment and expensive autoclaves, which makes it a more inexpensive technique.

5.3. Crystal structure

The KTP structure was determined by Tordjman *et al* in 1974[23]. It is an orthorhombic crystal and belongs to the acentric mm2 point group and the $Pna2_1$ space group with crystal lattice constants, a = 12.814 Å, b = 6.404 Å and c = 10.616 Å. There are four asymmetric units per unit cell, and two formula units per asymmetric unit, therefore, in the stoichiometric component, each unit has two crystallographically distinct atomic sites for each of the titanium Ti(1), Ti(2), phosphorus P(1), P(2), and potassium K(1), K(2) atoms. Ti atoms are six-coordinated, P atoms are four-coordinated, and K(1) atom is eight-coordinated together with K(2) which is nine–coordinated by O atoms.

The KTP structure is characterized by helical chains of distorted TiO_6 octahedra that are corner-linked and separated by PO_4 tetrahedra. The TiO_6 octahedra along the c-axis bridge the PO_4 tetrahedra to construct a three dimensional framework. This framework forms channels along the polar axis[24]. The K^+ ions are located at structural voids. Each of the TiO_6 groups contains a short Ti-O bond (of approximate length 1.7 Å) and a long Ti-O band (approximately 2.1 Å long)[25]. The difference in bond length makes the TiO_6 highly distorted. It has been suggested that alternating the long and the short Ti-O bonds will result in a net polarization along the polar axis which is the major contributor to the nonlinear optic coefficient for KTP[16,20]. Fig. 5.1 shows the KTP structure with a projection in the (001) direction.

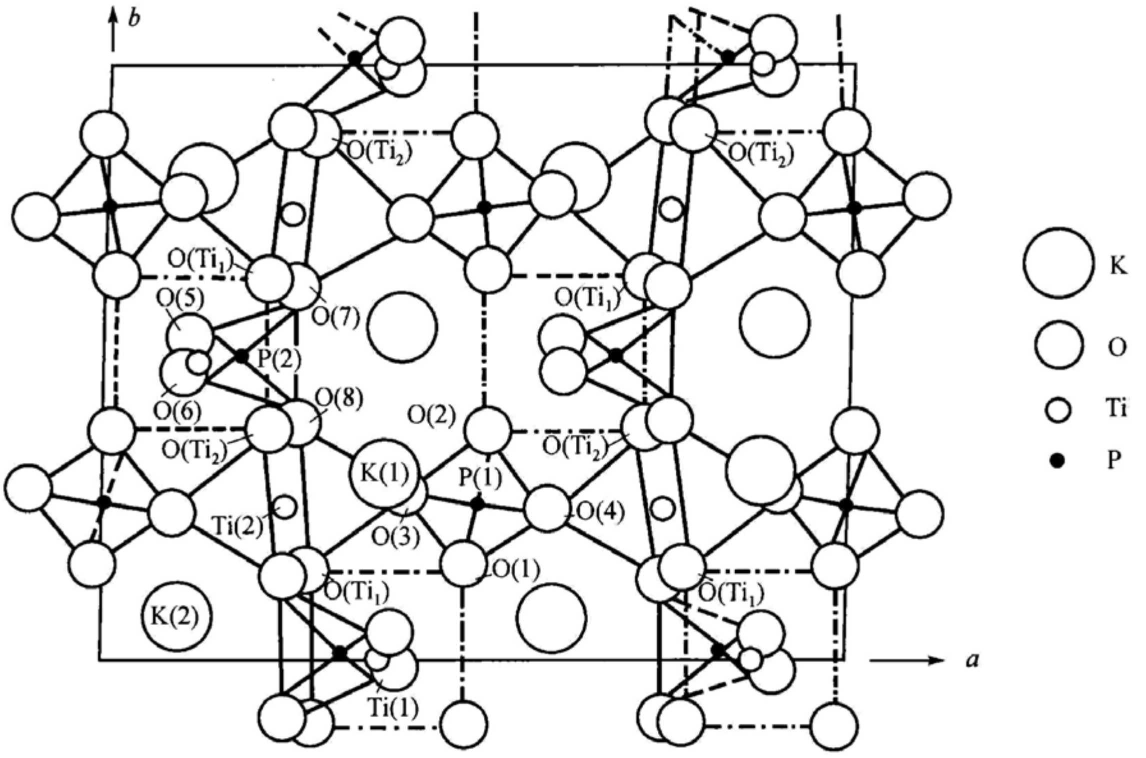

Fig. 5.1 Projection of the KTP crystal structure in the (001) direction[26].

KTP is the key member of the crystal family described by the compound formula $MTiOXO_4$, where the atom M can be K, Rb, Tl, NH_4 or Cs and the X atom can be P or As. By permuting the constituent elements, crystal manufactures have a possibility to synthesize several crystals with slightly different lattice parameters[16], linear optical properties as well as the nonlinearity[27].

In the KTP crystal structure, the K atom can be partially or totally replaced by another element like Rb. In RKTP, it has been demonstrated that rubidium substitutes for potassium only on the larger K(2) site in the lattice when the concentration of rubidium is low[28]. Rb(K) ions are displaced along the polar axis and the Ti atoms are displaced in a way so as to create the chains of alternating long and short Ti-O bonds[20].

5.4. Crystal properties

5.4.1. Ionic conductivity

The ionic conductivity originates from the ion transport in the crystal lattice. As we can see from Fig. 5.1, the open nature of the framework, built-up by the TiO_6 octahedra and the PO_4 tetrahedra, allows for cations to diffuse easily along the polar axis via a vacancy hopping mechanism. Thereby, KTP gets a relative large and highly anisotropic ionic conductivity. The ionic conductivity along the polar axis is typically three to four orders of magnitude larger than that perpendicular to the polar axis[29].

The ionic conductivity of KTP varies depending on the crystal growth process. Typically, the room-temperature ionic conductivity of flux-grown KTP is 10^{-6}S/cm. The high conductivity of flux-grown KTP is primarily attributed to the non-stoichiometry of the crystals, where the K^+-vacancies are built into the structure, which are then available for ionic transport with an applied electric field. Hydrothermally grown KTP, on the other hand, has a higher degree of stoichiometry and is, hence, much less conductive, typically 3 orders of magnitude lower than the flux-grown material[16]. However, as mentioned earlier, this material is much more difficult to grow.

To obtain a flux-grown material with low conductivity for periodic poling, one could utilize crystals with an inherently lower ionic conductivity, such as, RTA and RTP, which have very similar optical properties to KTP. Cheng *et al*[27] have reported that the ionic conductivity of RTP and RTA are 3 - 5 orders of magnitude lower than those of KTP and KTA. However, the usage of these low-conductive isomorphs is limited due to poor availability and the large variations in the crystal quality. The growth control for flux-grown KTP has now been refined and it is a rather mature process compared with the other isomorphs. Based on this, the doping technique was introduced into ordinary flux-grown KTP as an alternative strategy to lower the conductivity of flux-grown KTP. It has been reported that the ionic conductivity of KTP can be reduced by 1.5 to 3 orders of magnitude by introduction of dopants in the growth melt[30]. However, some of the dopants make it difficult to do the periodic poling as they occupy crystal lattice positions that inhibits or hampers the domain reversal. Other dopants, like Ta, and Nb, can be detrimental for the nonlinear properties[31].

KTP doped with Rb is an interesting candidate for periodic poling as we know that both KTP and RTP can be poled with good results and the larger Rb^+-ion reduces the conductivity[32,33] (Paper I). The reduction of the ionic conductivity for RKTP is a result of the higher activation energy for Rb^+ (0.45 eV) than for K, (0.33 eV)[33] in the crystal lattice. This is again attributed to the fact that Rb^+ has a larger atomic radius than K^+, and it is more difficult for the Rb^+ to pass through the bottleneck formed by the oxygen ions[34]. A Rb^+-ion will hence occupy the K(2) site longer time than a K^+-ion would do. This makes the hopping rate of Rb^+ much lower than that of a K^+ ion. The Rb^+-ion also blocks the lattice for the majority of the K^+-ions, which otherwise would like to hop but are unable to as the neighbouring sites are already occupied by Rb^+. The hopping rate of K^+ is then reduced with respect to that of Rb^+ as there are no possibilities to pass the Rb^+ ion for the K^+ ion.

In this work, we show that the dielectric property of flux-grown KTP can be modified substantially by just introducing a low doping level of Rb^+. The ionic conductivity of the resultant RKTP became approximately 2 orders of magnitude lower than that of KTP when two-mole percent of Rb was added to the growth melt (Paper VII).

In this thesis work, for the main part of my studies, flux-grown KTP has been the model material for room-temperature electric-field periodic poling, but, in the end of the work, RKTP came up as a promising alternative. Both the KTP and the RKTP were grown by Bright Crystals Technology, Inc. (Beijing, China), using the top-seeded growth technique.

5.4.2. Ferroelectricity

Ferroelectric crystals are materials with a spontaneous polarization, i.e., an inherent electric dipole moment per unit volume, that can be switched between two or more equilibrium states by an applied electric field. The equilibrium states have the same crystal structure, but differ in the direction of the spontaneous polarization at zero applied electric field. The electric field required to switch the direction of the spontaneous polarization is called the coercive field. In this work, we have measured coercive fields between 1.85 - 3.4 kV/mm for both KTP and RKTP. A ferroelectric domain is defined as a region of the ferroelectric crystal, with a uniform spontaneous polarization. In KTP, the domains have two states, the so-called 180 degree domains oriented either in the c^+ or the c^- direction. The interface between two domains is called the domain wall, so, for KTP, the domain wall is parallel to (100) crystal plane [35].

In ferroelectrics, the domains are stable below the Curie point, T_C. At this temperature, they undergo a structural phase transition from the polar into the paraelectric, non-polar state for which the ferroelectricity has vanished. For KTP, the Curie temperature is $T_c = 936^o C$ [35].

The ferroelectric property is commonly characterized by the ferroelectric hysteresis loop, i.e., a plot of the polarization versus the applied electric field. Unfortunately, it is not quite straightforward to obtain an ideal ferroelectric hysteresis loop for flux-grown KTP at room temperature due to screening from the high ionic conductivity. However, if the conductivity is reduced, it is possible to measure such a curve. Rosenmann *et al*[36] derived a spontaneous polarization value of 23.7 μC/cm^2 for flux-grown KTP at 170 K, where the K^+-ions are frozen into the lattice and the conductivity is reduced by five orders of magnitude down to 10^{-12} S/cm.

All ferroelectric materials are a subset of pyroelctrics, in which, the electric charges will be generated on the crystal surfaces when subject to a varying temperature.

5.4.3. Piezoelectricity

Piezoelectricity is a phenomenon where positive and negative charges are generated on a crystals surface when mechanical stress is imposed. The piezoelectric effect is a reversible electromechanical interaction. The inverse piezoelectricity is the generation of mechanical stress by an applied electric field. The responses are linear with the applied electric field. All ferroelectric crystals are also piezoelectric.

5.4.4. Optical properties

KTP crystals have been widely used for frequency doubling of the near-IR from Nd:YAG lasers into the green and also for near-IR OPOs. Recent development of periodically-poled KTP have provided a wider use of the material through its full transparency region from the UV (Paper II and Paper III), over the visible region (Paper I) to the near-IR spectrum[37,38]. The knowledge of the crystal transmission is thus also important for QPM devices. In general, $MTiOPO_4$ is transparent over a broad wavelength range, i.e., 0.35 - 4.5 μm, whereas the IR transmission extends to approximately 5.2 μm for the $MTiOAsO_4$ compound. So far, the shortest wavelength generated from KTP is 390 nm, by first-order QPM SHG (Paper II).

The optical transmission of KTP and its isomorphs were measured in Paper A. In this experiment, the light was linearly polarized along the z-axis and propagated along the x-axis, as is normally chosen for a QPM interaction. Fig. 5.2 shows the transmission windows for the potassium compounds KTA and KTP.

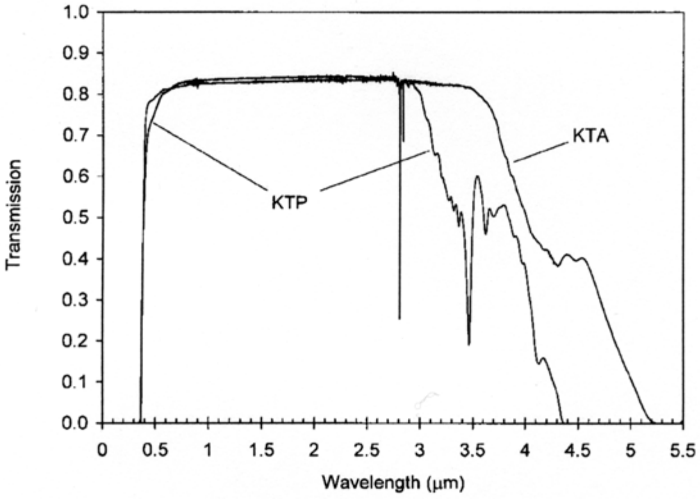

Fig. 5.2 Transmission window for KTP and KTA (Paper A). Crystal lengths are 10.00 mm and 10.05 mm for KTP and KTA, respectively. The Fresnel losses at the facets were not taken into account.

One common feature of these crystals is the strong absorption line at about 2.8 μm. It is caused by OH groups grown into, or trapped in, the crystals during growth. The OH group oscillates as a hydroxyl molecule and forms an OH^- defect in the crystals[39]. The strong absorption at this wavelength does not affect the QPM SHG devices directly, fortunately. The second feature is that the absorption increases in the infrared. This is attributed to the vibrations in the XO_4 tetrahedra[40].

To be able to generate a specific wavelength by the QPM devices, accurate knowledge of the refractive indices is needed. They are normally described by the Sellmeier equations and, hence, used for calculating the grating period. Fan *et al* has improved the Sellmeier equation coefficients of KTP for wavelengths shorter than 1 μm[41]. However, for wavelengths longer than 1 μm, better resultants are obtained by the coefficients reported by Fradkin *et al* [42]. Recently, Fragemann *et al* characterized RTP using periodic poling and published a more accurate Sellmeier equation for the wavelength range between 0.43 and 3.4 μm[32]. Generally, the two-pole Sellmeier equation is written as:

$$n^2 = A + \frac{B}{1 - C\lambda^{-2}} + \frac{D}{1 - E\lambda^{-2}} - F\lambda^2 \tag{5-1}$$

Here, λ is the vacuum wavelength, in micrometer. A, B, C, D, E and F are specific material constants. The coefficients for n_z and n_y for KTP and RTP, respectively, are listed in Table 5.1.

Crystal	**Index**	**A**	**B**	**C (μm^2)**	**D**	**E (μm^2)**	**F (μm^{-2})**
KTP[41]<1μm	n_y	2.19229	0.83547	0.04970	0	0	0.01621
KTP[41]<1μm	n_z	2.25411	1.06543	0.05486	0	0	0.02140
KTP[42]>1μm	n_z	2.12725	1.18431	0.0514852	0.6603	100.00507	0.00968956
RTP[32]	n_z	2.229382	1.230476	0.052475	2.40099	159.4113	0.00131914

Table 5.1 Sellmeier equation coefficients for KTP and RKTP according to the Eq (5-1).

For QPM, temperature tuning is a powerful tool not only for optimisation of the conversion efficiency at a fixed fundamental wavelength, but also for extending the wavelength range of the generated light from a periodic poled material with a specific grating structure. Together with the refractive indices, their temperature dependence, i.e., dn/dT, are very important characteristics for the PP material to predict precisely the phasematching temperature. Data on the temperature dispersion of KTP has been published by several authors. Ghosh's thermooptic coefficients[43] are specified for λ > 1 μm. Wiechmann's data[44] have shown to be more accurate for wavelengths shorter than 1 μm. For the latter one, the temperature dispersion for light polarized along the polar axis is of the form:

$$dn_z/dT = (12.415\lambda^{-3} - 44.414\lambda^{-2} + 59.129\lambda^{-1} - 12.101)(10^{-6}/^{o}C) \qquad (5\text{-}2)$$

where λ is the fundamental wavelength, in micrometer.

When the KTP structure is modified by partial substitution of some of the ions, discussed earlier in this chapter, the microscopic structural modification leads to macroscopic physical changes of the properties of the crystal. In this work, we have investigated experimentally how the optical characteristics vary when KTP was lightly doped with Rb (Paper VII).

In the experiment, we first measured the phasematching wavelength for pairs of PPKTP/PPRKTP with periods of 5.27 μm, 6.095 μm, and 6.81 μm, respectively, in a single-pass SHG set-up, pumped with a CW Ti:sapphire laser. The phasematching wavelength is slightly red-shifted for RKTP relative to that of KTP, but still much shorter than the calculated values for RTP. A comparison of the phasematching wavelengths of KTP, RKTP, and RTP is summarized in Table 5.2. The small shift of the phasematching wavelength of RKTP, with respect to KTP, indicates that the dispersion of n_z is modified only slightly from that of KTP although the ionic conductivity has been reduced substantially.

Crystal	**Phasematching wavelength in (nm) at different periods**		
	Λ =5.27 μm	Λ = 6.095 μm	Λ = 6.81 μm
KTP	908.1	946.3	977.5
RKTP	908.4	946.5	977.7
RTP	919.6	958.5	990.1

Table 5.2 Comparison of phasematching wavelengths for KTP, RKTP, and RTP for three grating periods (PaperVII).

To investigate the wavelength dependence on temperature for PPRKTP relative to PPKTP, we recorded the fundamental peak wavelength for each of the crystals in the temperature range of 20 – 70 °C for all three periods 5.27 μm, 6.095 μm, and 6.91 μm, respectively. As expected, it was found that they all have approximately the same wavelength dependence on the temperature, namely, 0.05 nm/°C. Fig. 5.3 shows the wavelength dependence on the crystal temperature for PPKTP and PPRTP with a period of 5.27 μm. Approximately 2.5 nm wavelength tuning range was achieved when both PPKTP and PPRKTP were temperature tuned over a range of 50°C (20 – 70 °C).

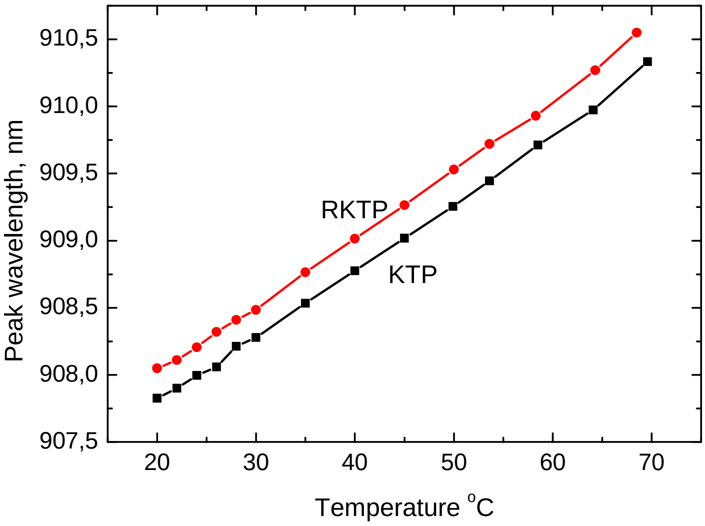

Fig. 5.3 The wavelength dependence on the crystal temperature for PPRKTP and PPKTP with the same period of 5.27 μm (Paper VII).

As we have discussed earlier in this chapter, KTP and its isomorphs belong to the mm2 point group. Crystals with a such symmetry have only 5 non-zero nonlinear coefficients, viz:

$$(d)=\begin{pmatrix} 0 & 0 & 0 & 0 & 0 & d_{15} \\ 0 & 0 & 0 & d_{24} & 0 & 0 \\ d_{31} & d_{32} & d_{33} & 0 & 0 & 0 \end{pmatrix} \qquad (5\text{-}3)$$

The non-zero nonlinear coefficients of KTP reported by Vanherzeele and Bierlein[45] are listed in Table 5.3.

	d_{il} (pm/V) for KTP				
Wavelength	d_{15}	d_{24}	d_{31}	d_{32}	d_{33}
1064 nm	1.91	3.64	2.52	4.35	16.9

Table 5.3 Nonlinear optical coefficients of KTP at $\lambda = 1064\,nm$.

We made an experiment in order to compare the effective nonlinear optical coefficient, d_{eff}, between PPKTP and PPRKTP in a single-pass set-up. The PPRKTPs were 8.5 mm-long with periods of 5.27 μm (sample A), 6.095 μm (sample B), and 6.81 μm (sample C), respectively. The pump power were 230 mW for the first and the second crystal, and 150 mW for the third one. The maximum SHG powers were, respectively, 825 μW, 800 μW, and 280 μW, generated at the fundamental wavelengths of 908.4 nm, 946.5 nm and 977.7 nm, respectively (See Table 5.2). Taking into account the optical losses, the corresponding effective nonlinear coefficients are all around 10.3 pm/V, which is very similar to the corresponding figure from a well-poled KTP and, hence, in good agreement with Vanherzeele's and Bierlein's value of d_{33}. Our results support the proposal by Zumsteg *et al*[20] discussed earlier that the nonlinearities of KTP isomorphs are primarily related to the alternating-length Ti-O bonds and not so strongly influenced by the alkali-ion subsystem.

The electro-optic coefficients and the thermal expansion coefficients of KTP were measured by Bierlein *et al*[16,29] and the figures are listed in Table 5.4.

Electro-optic coefficient[29]		**Thermal expansion coefficient ($^oC^{-1}$)**[16]
r_{ij} (pm/V)	Value	
r_{13}	9.5	$\alpha_1 = 11x10^{-6}$ $\alpha_2 = 9x10^{-6}$ $\alpha_3 = 0.6x10^{-6}$
r_{23}	15.7	
r_{33}	36.3	
r_{51}	7.3	
r_{42}	9.3	

Table 5.4 The electro-optic coefficients and the thermal expansion coefficient of KTP.

References of Chapter 5

[1] P. F. Bordui and M. M. Fejer, Annu. Rev. Mater. Sci. **23**, 321 (1993).

[2] http://www.opt-oxide.com/english/index.html.

[3] A. Rauber, "Current topics in materaials science", ed. E. Kaldis, Amsterdam, North Holland, (1978).

[4] K. Mizuuchi, and K. Yamamoto, Opt. Lett. **21**, 107 (1996).

[5] K. Mizzuchi, K. Yamamoto, M. Kato, Appl. Phys. Lett. **70**, 1201 (1997).

[6] A. Kuroda, S. Kurimura, and Y. Uesu, Appl. Phys. Lett. **69**, 1565 (1996).

[7] Unpublished internal data from Junji Hirohashi.

[8] K. Kitamura, Y. Furukawa, K. Niwa, V. Gopalan and T. E. Mitchell, Appl. Phys. Lett. **73**, 3073 (1998).

[9] Unpublished internal data from Junji Hirohashi.

[10] Y. Furukawa, K. Kitamura, S. Takekawa, A. Miyamoto, M. Terao, and N. Suda, Appl. Phys. Lett. **77**, 2494 (2000).

[11] M. Nakamura, S. Takekawa, K. Terabe, K. Kitamura, T. Usami, K. Nakamura, H. Ito and Y Furukawa, Ferroelectrics **273**, 199 (2002).

[12] N. Iyi, K. Kitamura, Y. Yajima and S. Kimura, J. Solid State. Chemistry **118**, 148 (1995).

[13] J. Hirohashi, K. Yamada, H. Kamio and S. Shichijyo, Jap. J. Appl. Phys. **43**, 559 (2004).

[14] I. Biaggio, P. Kerkok, L. S. Wu, P. Gunter and B. Zysset, J. Opt. Soc. Am B **9**, 507 (1992).

[15] J.-P Meyn, M. E. Klein, D. Woll and R. Wallenstein, Opt. Lett. **24**, 1154 (1999).

[16] J. D. Bierlein, H. Vanherzeele, J. Opt. Soc. Am. B**6**, 622 (1989).

[17] F. Laurell, Optical Materials **11**, 235 (1999).

[18] Y. Wang, V. Petrov, Y. J. Ding, Y. Zheng, J. B. Khurgin, and W. P. Risk, Appl. Phys. Lett. **73**, 873 (1998)

[19] J. C. Jacco, G. M. Loiacono, M. Jaso, G. Mizell, B. Greenberg, J. Cryst. Growth **70**, 484 (1984).

[20] F. C. Zumsteg, J. D. Bierlein, and T. E. Gier, J. Appl. Phys. Lett. **47**, 4980 (1976).

[21] J. C. Jacco, G. M. Loiacono, M. Jaso, G. Mizell and B. Greenberg, J. Crystal Growth **70**, 484 (1984).

[22] K. Iliev, P. Peshev, V. Nikolov and I. Koseva, J. Crystal Growth **100**, 219 (1990).

[23] I. Tordjman, R. Masse, and J. C. Guitel, Z. Kristallogr. **139**, 103 (1974).

[24] J. D. Bierlein, A. Ferretti, L. Brixner, Y. Hsu, Appl. Phys. Lett. **50**, 1216 (1987).

[25] G. D. Stucky, M. L. F. Phillips and T. E. Gier, Chemistry of Materials **1**, 492, (1989).

[26] K. Zhang and X. Wang, Chinese Science Bulletin **46**, 2028 (2001).

[27] L. K Cheng, L. T. Cheng, J. Galperin, P. A. Morris Hotsenpiller, J. D. Bierlein, J. Crystal Growth, **137**, 107 (1994).

[28] P. A. Thomas, R. Duhlev and S. J. Teat, Acta Cryst. **B50**, 538 (1994).

[29] J. D. Bierlein and C. B. Arweiler, Appl. Phys. Lett. **49**, 917 (1986).

[30] P. A. Morris, A. Ferretti, J. D. Bierlein and G. M. Loiacono, J. Crystal. Growth **109**, 367 (1991).

[31] V. Pasiskevicius, H. Karlsson, L. K. Cheng, J. A. Tellefsen, F. Laurell, Technical Digest. Summaries of Papers Presented at the Conference on Lasers and Electro-Optics. Conference Edition. 1998 Technical Digest Series, **6**, (IEEE Cat. No. 98CH36178), 271 (1998).

[32] A. Fragemann, V. Pasiskevicius, J. Nordborg, J. Hellström, H. Karlsson and F. Laurell, Appl. Phys. Lett. **83**, 3090 (2003).

[33] Q. Jiang and P. A. Thomas, J. Appl. Phys. **92**, 2717, (2002).

[34] S. Furusawa, H. Hayasi, Y. ishibashi, A. Miyamoto and T. Sasaki, J. Phys. Soc. Japan **62**, 183 (1993).

[35] J. D. Bierlein and F. Ahmed, Appl. Phys. Lett. **51**, 1322 (1987).

[36] G. Rosenman, A. Shliar, D. Eger, M. Oron and M. Katz, Appl. Phys. Lett. **73**, 3651 (1998)

[37] J. Hellström, V. Pasiskevicius, F. Laurell and H. Karlsson, Opt. Lett. **24**, 1233 (1999).

[38] H. Karlsson, M. Olson, G. Arvidsson, F. Laurell, U. Bäder, A. Borsutzky, R. Wallenstein, S. Wickström and M Gustafsson, Opt. Lett. **24**, 330 (1999).

[39] P. A. Morris, M. K. Crawford and B. Jones, J. Appl. Phys. **72**, 5371 (1992).

[40] J. C. Jacco and G. M. Loiacono, Appl. Phys. Lett. **58**, 560 (1991).

[41] T. Y. Fan, C. E. Huang, B. Q. Hu, R. C. Eckardt, Y. X. Fan, R. L. Byer and R. S. Feigelson, Appl. Opt. **26**, 2390 (1987).

[42] K. Fradkin, A. Arie, A. Skliar and G. Rosenman, App. Phys. Lett. **74**, 914 (1999).

[43] G. Ghosh, IEEE Photonis. Tech. Lett. **7**68 (1995).

[44] W. Wiechmann, S. Kubota, T. Fukui and H. Masuda, Opt. Lett. **18**, 1208 (1993).

[45] H. Vanherzeele and J. D. Bierlein, Opt. Lett **17**, 982 (1992).

6. Fabrication and characterization of PPKTP and PPRKTP

6.1. Introduction

An important contributor to the developments in nonlinear optics is the practical realization of QPM devices for frequency conversion using periodically-poled ferroelectrics. In particular, this has been important for the realization of compact and efficient blue-green sources as well as for UV light generation. However, it is a very challenging task to fabricate high-quality PP structures with fine-pitch domain gratings (3 - 10 μm periods) in large aperture samples (> 0.5 mm) needed for medium and for high-power applications. In this chapter, I will discuss where some of the difficulties lie, both related to the fabrication procedure as such and as regards the basic material. Emphasis will be put on the special problems of crystals made from the KTP family, like the material homogeneity and the conductivities. I will also address ways to improve the fabrication of periodically-poled crystals using pre–poling screening and the use of in-situ SHG monitoring technique during poling. Some novel techniques for evaluating the poled crystals will finally be introduced as well.

6.2. Electric-field poling of KTP and RKTP

6.2.1. Domain switching for the KTP family

The most common method to achieve domain reversal in ferroelectrics is by electric-field poling. The applied electric field should have a strength exceeding the coercive field, in a direction antiparallel to the spontaneous polarization. This allows the ions to overcome the potential energy barrier in order to re-orient towards the opposite dipole position. In the case of KTP and its isomorphs, Stolzenberger *et al*[1] have proposed a model for the reversal. It takes place in the crystal by a shift of the alkali atoms (K, Rb) in the –z direction with only a slight relaxation of the neighbouring oxygen ions. The 9-fold coordinated alkali ion in the pre-poled lattice becomes an 8-fold coordinated ion after poling, and visa versa. In the meantime, the domain reversal is accompanied by a slight rotation of the PO_4 tetrahedra and the TiO_6 octrahedra, as well as a bond exchange between the long and the short Ti-O bounds. For further detail, see Chapter 5.

6.2.2. Sample preparation for poling

The as-purchased, z-cut flux-grown KTP and RKTP wafers have a typical size of $30(x) \times 30(y) \times 1(z)\ mm^3$. Their domain status are first inspected using a d_{33} piezo tester (American Piezo Ceramics, Inc), and, in most cases, they are completely single domain. A pronounced feature for flux-grown KTP and its isomorphs is that they acquire a variation in stoichiometry during growth. This manifests itself as a nonuniform ionic conductivity over the whole wafer, but the ionic conductivity also varies from one boule to the other. It has been found important to obtain the conductivity information on the whole wafer prior to the poling to properly match the poling conditions to the individual sample.

The room-temperature ionic conductivity of a specific wafer along the polar axis can be determined from a simple current measurement. In my investigations, I applied a few ms-long electric pulse over an area A of the c-cut wafer. The ionic conductivity can then be deduced from the following expression:

$$\sigma = \frac{IL}{VA} \tag{6-1}$$

where I is the current through the external circuit, V is the applied voltage across the sample, and L is the thickness of the sample.

To eliminate any risk of bulk poling during the conductivity measurement, the external field has to be applied in parallel to the spontaneous polarization. Specifically in our experiments, the c^- side was probed by a metal tip, with a diameter of 1.5 mm and the opposite side was contacted with a saturated KCL solution. Typically, the ionic conductivity of flux-grown KTP is approximately 10^{-6}/S·cm.

By mapping the ionic current through over the whole wafer, the homogeneity information of the ionic conductivity for a specific wafer is gathered. Fig. 6.1 shows a typical result for KTP. The ionic conductivity is rather constant along the x-axis (crystallographic a-axis) while it has an approximate parabolic profile along the y-axis (crystallographic b-axis). Typically, it is increased by a factor of 2 from the edge to the centre of the wafer. The non-uniformity of the conductivity is attributed to the temperature gradient the crystal experienced during the growth which leads to a spatial stoichiometry variation.

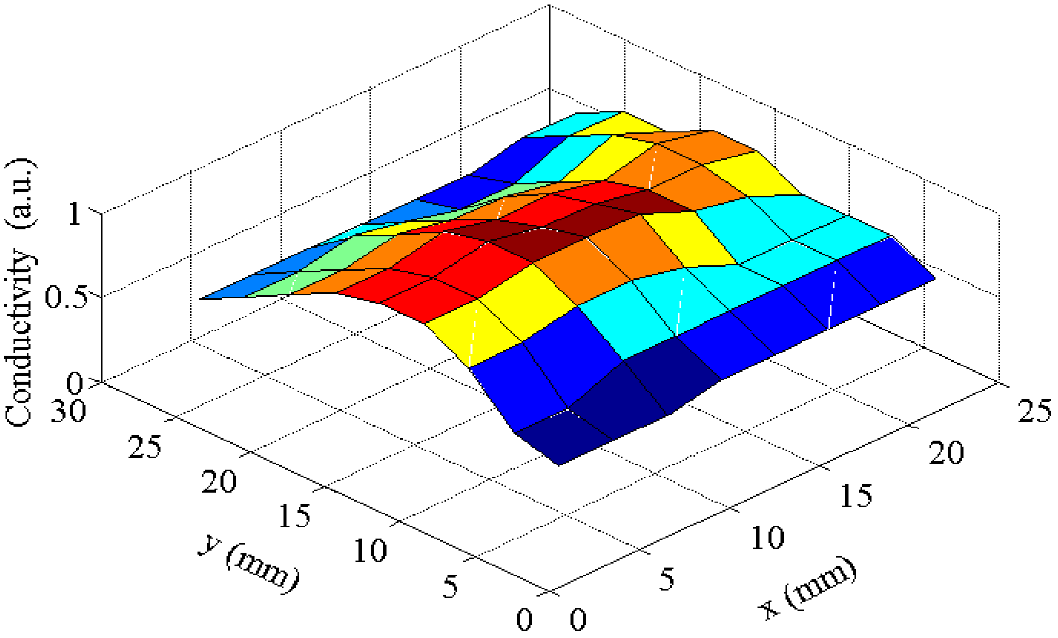

Fig. 6.1 Conductivity map of a flux-grown KTP wafer.

For the RKTP used in this work, the crystals were grown with the same method as the flux-grown KTP crystals. The ionic conductivity was approximate1.5 x 10^{-8}/S·cm, i.e., about 2 orders of magnitude lower than that of the non-doped KTP. This suggests that RKTP might be a better candidate for periodic electric-field poling.

To achieve a higher yield for KTP, the wafer is then cut up into smaller samples. Each sample can then be poled individually. The dimensions of the small samples are chosen to fit the particular applications they are intended to be used for. More importantly, during the whole process, we kept track of all the samples, with respect to their original location on the wafer in order to try to learn more about how the ionic conductivity affects the poling results.

A preferred orientation of the grating vector for PPKTP will depend on the nature of the domain wall formation when the KTP crystals are subject to the poling field. Bierlein *et al*[2] and Miller *et al*[3] discussed this issue by examination of the crystal structure of KTP. According to Bierlein and Ahmed[2], the Ti-O chains oriented along the (011) and the $(0\bar{1}1)$ directions contribute to the z-directed polarization. Domain walls parallel to the (100) planes will be preferred because this plane does not intersect the Ti-O chains. Also, the lattice constant along the a-axis is about two times larger than that of along the b-axis. We could interpret Miller and Weinreich's model[3] in such a way that the domain growth should occur preferably in the direction of the crystallographic b-axis where the nucleation step is minimal. The two models predict that the domain growth in KTP crystals should elongate along the y-axis. Accordingly, the length of the sample should be cut along the x-axis which then is the direction of the QPM grating vector.

The samples were optically polished on the x-face to allow the laser beam to pass through the crystal. Following this, approximately 2 μm-thick photoresist (Shipley Microposit S1818) is spun onto the c^- -face. Then the sample is pre-baked on a hot plate at 105 °C for 90 s to harden the resist. The required grating structures are then transferred to the crystals with standard lithographic technique. Grating periods ranging from 2.95 μm to 35 μm were used for the thesis work reported here.

The last step prior to poling is to deposit a metal layer as an electrode, usually an aluminum film, on the patterned side. A frequently used electrode configuration for electric-field poling of KTP and its isomorphic crystals is showed in Fig. 6.2.

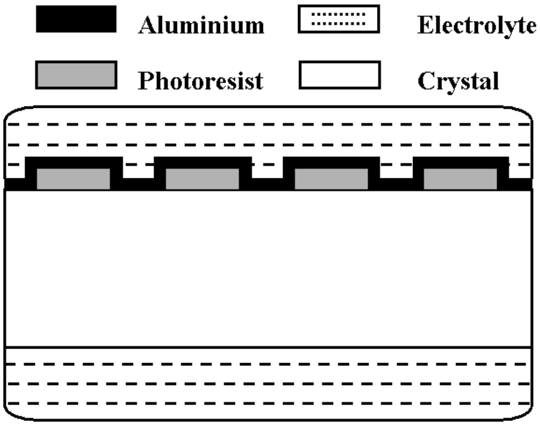

Fig. 6.2 Standard electrode configuration for electric-field poling of KTP.

6.2.3. Basic electric-field poling technique

Energy is needed to change a domain from one state to the other. In electric-field poling, it is in the form of a charge transfer. The necessary charge depends on the material's spontaneous polarization, P_s, and the area of the domain-reversed region, A, and is given by the expression $Q = 2P_s A$. The charge is defined to be the integration of the current, *I*, through the sample over the poling time, τ, i.e., $Q = \int_0^\tau I dt$. For low conductive ferroelectrics, such as $LiNbO_3$, monitoring of the current flowing in the poling circuit is an effective method to determine the progress of the poling and to find the right time for when it is complete. However, flux-grown KTP, as well as its isomorphs, has an ionic conductivity which to a large degree screens the poling current. It is thereby difficult to use the current as a sole monitoring technique.

Rosenman *et al*[4] avoided this difficulty by cooling the KTP to 170 K where the crystals undergo a transition from the superionic to the dielectric state. Thereby, they could control the poling directly by monitoring the switching current. A disadvantage of this method is that the coercive field increases substantially at lower temperature, and a field as high as 12 kV/mm was needed to switch the polarization. In practice, a high poling-field strength does not allow very thick crystals to be poled. Moreover, low-temperature poling requires special means to be taken into account in order to avoid icing of the equipment.

Karlsson and Laurell developed an alternative monitoring technique based on the electro-optic response in order to monitor the poling of KTP at room temperature[5]. In this technique, a He-Ne probe laser beam propagates along the grating vector and is linearly polarized 45^o to the z-axis. When the domains grow through the crystal, the output intensity of polarization the state of the He-Ne beam changes accordingly. This change is then detected by a second polarizer positioned orthogonally to the first one, together with a photodiode, and is displayed on an oscilloscope. Fig. 6.3 illustrates the electro-optic monitoring set-up.

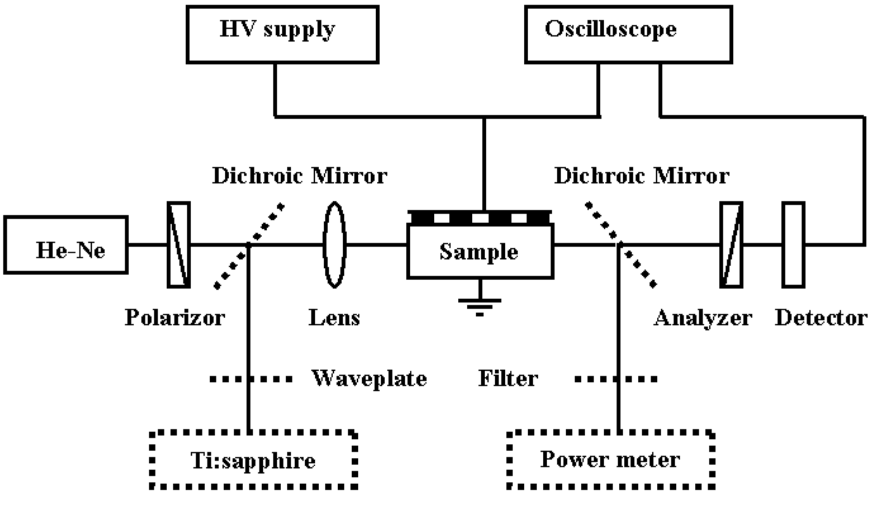

Fig. 6.3 Poling monitoring set-up for KTP and its isomorphic crystals.

In this thesis work, the crystals were poled by applying square-wave pulses, with 6 ms duration. The rise time was less than 0.1 ms and the fall time was about 1 ms. The number of these pulses and the applied field strength varied from sample to sample. For KTP, the poling field varied from 1.85 kV/mm (Paper III) to 2.3 kV/mm (Paper I). In the case of RKTP, the crystals were poled at 3.4 kV/mm (Paper VII).

In my Licentiate thesis work[6], it was found that samples from the edge of the KTP wafers are more suitable for periodic poling than those from the centre, as they have lower conductivity. The edge samples are also poled at a lower field than those at the centre. It is generally accepted that a high stoichiometry gives a low conductivity and also a low poling field. This result, which was obtained for KTP, coincides with the results achieved from studies on $LiNbO_3$ and $LiTaO_3$ crystals in which the coercive fields were substantially reduced in stoichiometric crystals as compared to their nonstoichiometric compositions. For instance, the switching field for SLN and SLT is reduced to about 4 - 5 kV/mm[7] and 1.7 kV/mm[8], respectively, with respect to 21 kV/mm for the congruent crystals.

The ionic conductivity of KTP originates from the vacancy hopping mechanism. Both potassium and oxygen vacancies contribute to the deviation from stoichiometry[9]. A correlation between the vacancies, or rather the potassium content, and the coercive field was, in fact also investigated by Rosenman *et al*[10] where a substantial decrease in the coercive field was observed when the potassium content was increased.

For the case of RKTP, the coercive field increased substantially compared to that of KTP. This can not be explained by the defect mechanism discussed above. Instead, one should consider that the activation energy of Rb^+ (0.45 eV) is larger than that of K^+ (0.33 eV) by an amount of 0.12 eV[11]. It should, hence, be more difficult to shift Rb^+ in the –z direction during the polarization reversal process than to shift the K^+-ion. Consequently, a higher poling field is needed.

The domain evolution of KTP crystals, poled at room temperature, had previously not been documented. For this purpose, then, we studied the domain propagation from PPKTP samples (Paper VI) using a commercial atomic force microscope. 1mm-thick sample used for this experiment has a period of $\Lambda = 26.3\ \mu m$, and was poled by one pulse of 2.1 kV followed by two pulses of 1.75 kV.

Fig. 6.4 displays the images four different positions on the *b*-face of a sample. The top of Figure (a), (b) and (c), correspond to the surface of the c^- patterned side. For clarity, the metal electrodes have been redrawn (black squares). These three scans represent different stages of the development of the domain inversion region under the electrodes. Fig. 6.4(a) shows the domain formations starting at the edges of the metal electrodes and the fast propagation along the polar axis. Fig. 6.4(b) portrays another region of the same sample, showing several independent tips growing between the two electrode edges. This indicates that, in this stage, the domain switching is governed by the nucleation of new domains. The tips growing from the middle of the electrodes do not penetrate as deeply as the ones growing from the edges, since the field in this position is not as high as that at the edge of the finger electrode. Fig.6.4(c) displays a third position in the same sample. Here, the nucleated domains are in the process of merging or have already merged. It is worth noting that the domain merging occurs much before the tips of the first edge-nucleated domains reach the c^+-face. After the initial domain nucleation at the electrode edges on the patterned surface, the domains rapidly propagate along the polar direction helped, in part, by the electric field enhancement at the tips of the growing domains [see Fig. 6.4(d) which shows the domain tips at a depth of 290 μm, where the domains of Fig. 6.4(a) terminate].

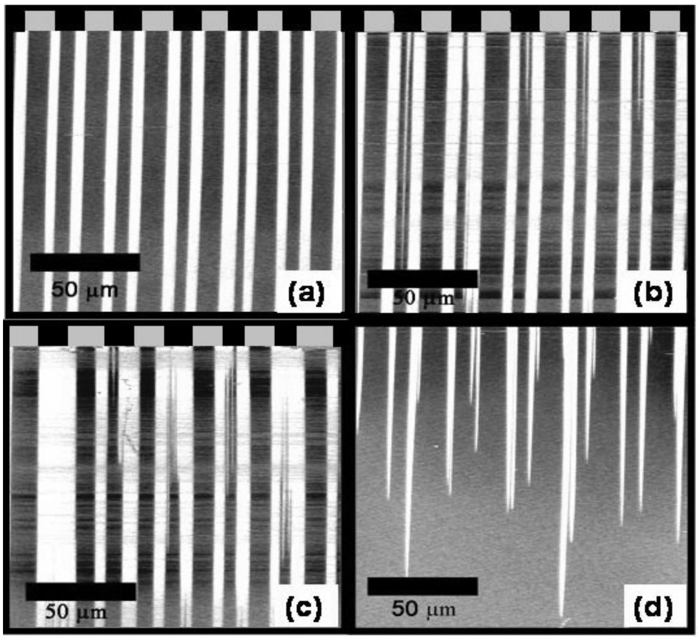

Fig. 6.4 Four different areas of the b-face of a PPKTP with Λ = 26.3 μm are imaged with AFM. The top of figures (a), (b), and (c) is the edge with the patterned electrode. For clarification, the metal electrodes have been drawn in black and the photoresist grating in grey. Figure (d) shows an area where the tips of figure (a) terminate.

In brief, the domain growth for the KTP family is as the follows: the domain nucleation begins at the two edges of each finger electrode where the field is strongest. The domain nuclei rapidly propagate vertically (z-direction) down toward the opposing crystal face, and, in a slower process, merge horizontally under each electrode. Evidently, the domain growth in KTP follows the same model as described for $LiNbO_3$[12].

6.2.4. Improvement of domain engineering in KTP and RKTP

6.2.4.1. In-situ SHG monitoring

The main objective of electric-field periodic poling is to obtain an engineered domain structure in the crystal with high quality. To do this, we need accurate control techniques. The electro-optic monitoring method discussed earlier is simple and practical, but, it gives only integrated information over the local volume illuminated by the He-Ne beam and, hence, only a rather rough quantitative indication of the poling result can be obtained[5]. Therefore, it is important to develop alternative qualitative monitoring methods to be able to improve the homogeneity.

The in-situ SHG technique I have explored relies on a CW Ti:sapphire laser which is loosely focused through the crystal and tuned to the phasematching wavelength. The SHG signal is measured by a power meter. We can thus follow how the signal develops after each poling pulse and stop when we either have reached a known maximum or when the SHG signal saturates. Since the domains nucleate and start to grow from the patterned side, the signal is hence first obtained close to this surface and then, with subsequent pulses, the signal is increasing deeper and deeper down into the sample, showing that the domains propagate towards the opposite side of the sample. If too many pulses are applied, the signal will decrease and we have indications of over-poling. After each pulse, it is possible to obtain information on the homogeneity of the poled sample without removing it from the poling set-up by scanning the beam in the horizontal (width) and vertical (depth) directions. For the case of loose focusing, it is possible to calculate an optimum SHG signal where the poling process should be stopped, using the Boyd-Kleinman equation given in Eq (2-16).

As a Ti:sapphire laser can deliver radiation with wavelengths between 700 nm and 1100 nm, QPM grating periods between approximately 2 - 10 μm for KTP [13] and RTP[14] can be studied using 1st order SHG. For periods longer than 10 μm, higher order SHG could be used, according to the expression:

$$\lambda_F = \frac{2\Lambda(n_{SH} - n_F)}{m} \tag{6-2}$$

where Λ is the grating period, λ_F is the phasematching peak wavelength, and m is the phasematching order. In theory, only odd-order SHG signal should be observed when the crystals are poled with a 50/50 duty cycle. In reality, though, even-order SHG signal can also be seen if an imperfect duty cycle has been obtained.

As an example of how the in-situ technique is used, results from our measurements on RKTP are presented. Four 1mm-thick RKTP samples with periods of 5.27 μm (A), 6.095 μm (B), 6.81 μm (C) and 35 μm (D), were prepared in the way we have discussed above for poling (Paper VII). Aluminium finger electrodes with photoresist isolation were fabricated lithographically on the c^--face with a 40/60 duty cycle. The electric contact was made with a KCl water solution. The in-situ SHG, and the electro-optic response method, were both employed to monitor the domain inversion. In Fig. 6.3, the in-situ monitoring details are shown with dashed lines. The He-Ne and the Ti:sapphire laser beams were collinearly overlapping and loosely focused inside the sample with a 150 mm lens. 6 ms-long, high-voltage pulses were applied to the c^+ side of the crystals while the c^--side was grounded. The SHG signal, the He-Ne and the IR beams were separated by a dichromic mirror and filters, respectively. To determine the poling voltage of the new material, we applied the voltage in incremental steps on a dummy sample until we could detect signals with the two techniques. The spontaneous polarization was not reversed until the voltage over the sample had reached 3.4 kV. Direct current monitoring was not an effective method due to a conductivity which was still too high.

All the RKTP samples were then poled by first applying one 6 ms-long pulse at 3.4 kV. The He-Ne beam modulation indicated that the domain reversal was taking place in the part of the crystals where the He-Ne beam was passing. The Ti-sapphire could then be fine-tuned to the wavelength where the SHG signal appeared strongest, i.e., where the phasematching peak. The signal could then be compared to what was theoretically expected from Eq (2-16). Samples A and B had a signal close to the theoretical maximum. The homogeneity of these samples was then tested by translating them horizontally and vertically. They had a constant SHG signal over the whole aperture of the sample and no further poling was needed. For sample C, the SHG power also reached the theoretical value in the centre, but when it was scanned in the IR beam it was found that only about 70 % of the aperture, primarily in the upper part of the sample, had this value. In the lower part of the sample, the signal was lower and we drew the conclusion that the domains had not yet propagated completely to the opposite side of the crystal. Additional field was therefore needed to drive the domains all the way down to the other side. This had to be done in a very careful way as the driving of the domains takes a much lower electrostatic energy compared to the domain nucleation. In order to homogenize the QPM structure, we applied several pulses at 1 kV over this sample. After 5 additional pulses, the SHG signal had indeed increased to about 90 % of the theoretical value in the area where it previously had been low, while it still was unchanged in the area where the signal was high after the first pulse. When we then applied one more pulse the signal was reduced slightly on the patterned side indicating the start of domain broadening. The poling was then stopped. For sample D, 7th order SHG was used to monitor the poling. In high-order SHG, the output power is strongly dependent on the duty cycle of the electrodes, as we discussed earlier in Chapter 3. It is, therefore, not so useful, or even accurate, to compare the absolute value of the detected SHG signal with the theoretical value. For sample D, two pulses at 3.4 kV were needed to get a good SHG signal and two pulses at 1 kV were further applied to obtain a homogeneous poling over the whole aperture. It should be noted that the quality improvement for samples C and D could only be obtained by utilizing the in-situ SHG monitoring technique.

6.2.4.2. Optimising the duty cycle

The duty cycle of the PP structure plays an important role for the effective nonlinear coefficient as can be seen in Eq (3-4). The uniformity of the duty cycle is also important because it will contribute to the overall conversion efficiency of the QPM device. The ideal duty cycle for first-order QPM is 50 %.

Domain broadening can occur during the poling of flux-grown KTP at room temperature (Paper VI). We have therefore investigated this phenomenon using AFM scans of the polar c-face. Fig 6.5 shows substantial changes of the duty cycle in a 1mm-thick poled sample with a period of 10.6 μm poled with 1 pulse of 2.46 kV, followed by 6 pulses of 1.74 kV. The average inverted domains have a width of 6.5 μm, i.e., 65 % duty cycle compared to the 30 % duty cycle of the electrode (electrode in grey).

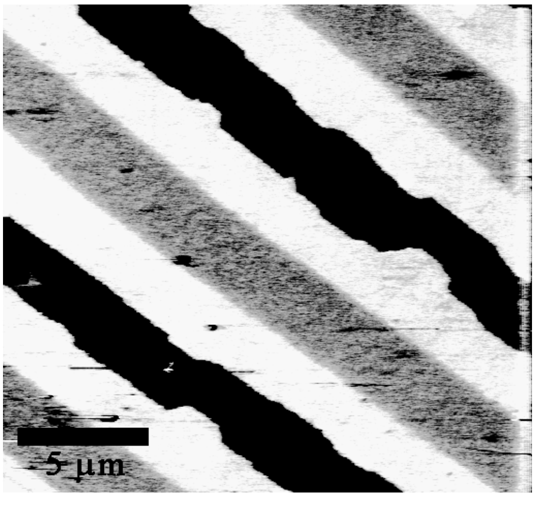

Fig. 6.5 Broadened domain structure on the c^- face of a KTP sample with the topography of the metal electrode (in grey) overimposed.

To investigate how the domain broadening depends on the duty cycle of the electrode, the period and the poling parameters, we inspected another sample. A 60 % of duty cycle of the domain pattern was obtained under the electrodes from a 40 % original electrode duty cycle and a period of $\Lambda = 26.3\mu\text{m}$, poled by one pulse of 2.1 kV followed by two pulses of 1.75 kV.

The origin of the broadening comes from the tangential component of the fringing electric field which is so strong that compensating charges can be injected into the insulated regions to initiate domain nucleation and growth there. To obtain the required mean duty cycle of the device, compensation of the domain broadening has to be considered when one designs the QPM devices. This means that an electrode pattern with a duty cycle smaller than 0.5 should be used. Different duty cycles, ranging from 25 % to 40 % have been tested for optimising the conversion efficiency in this work. Here, one should have in mind, of course, that the relative effect of the domain broadening is much larger for short periods than for long ones.

6.3. Characterization of domain structures

In this section, several evaluation techniques will be compared and discussed.

6.3.1. Piezoelectric probing

Piezoelectric probing is a method in which a needle is probing the surface of the sample by applying an oscillatory force to the crystal. The piezoelectric response is monitored electronically on an oscilloscope. The relative phase difference between the applied force and the piezoelectric response gives information of the orientation of the local domain. For simplicity, a reference sample is used to determine the absolute orientation. In the first stage of an evaluation of a virgin crystal, the negative or the positive sign of piezoelectric response gives us the orientation of the wafer, i.e., the c^--face or the c^+- face. In the set-up we employ the needle has a rather large tip area and it is, hence, probing a relatively large area of the sample. For a periodically poled sample with micrometer-sized domains, with a 50 % duty cycle, the piezoelectric response will be zero due to averaging over both the negative as well as the positive domains. On the other hand, if the samples are not perfectly poled or they are designed with an uneven duty cycle, the piezoelectric response will have a non-zero value.

The advantage of domain surface mapping with this method is that it is fast, simple, and non-destructive. However, one could neither obtain qualitative information on the duty cycle or the uniformity by this technique.

6.3.2. Selective etching

For many ferroelectrics, chemical etchants have been found which will etch the positive and the negative c-faces at different rates. It is, thus, possible to reveal the domain structure for periodically-poled crystals. Early studies with $BaTiO_3$ using HCl as an etchant have been extensively documented[15]. It has also been found that a KOH-based eutectics could selectively etch the faces of KTP[16]. Molten salts containing hydroxide attack the negative face, the c^- face, of KTP, while the positive face is left relatively untouched. This technique can, therefore, be utilized to etch PPKTP. My best results were obtained with a 2:1 mole ratio of a water solution of KOH and KNO_3[17] at about 80 °C with etching times varying from 1 to 5 minutes.

Fig. 6.6 shows the domain structure for a first-order type-I UV crystal (Paper II). The period is 2.95 µm, which is designed to generate radiation at 390 nm. The dark segments seen in the picture are the etched parts. Fig. 6.6(a) shows the etched surface on the patterned side where the resultant duty cycle is close to 50 %. Fig. 6.6(b) shows the opposite surface of the crystal. It is obvious that the duty cycle is less uniform here and that the domains have not grown throughout the whole thickness of the whole crystal.

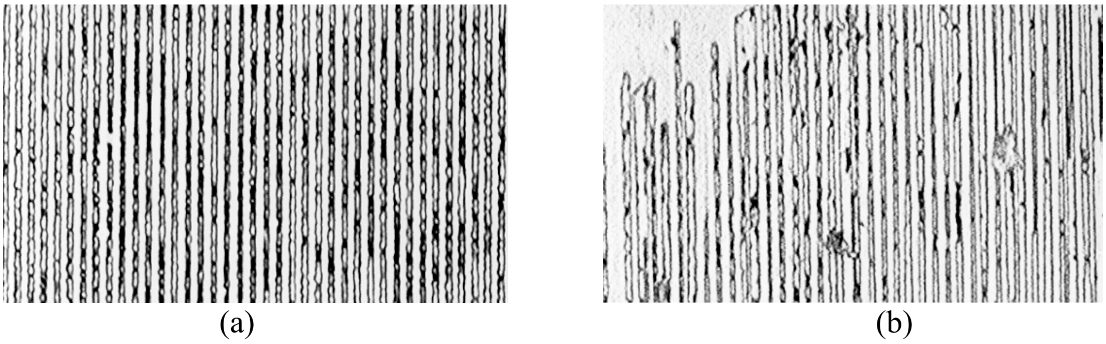
(a) (b)

Fig. 6.6 Microphotograph of an etched PPKTP sample for first-order type-I UV generation. (a): The patterned side; (b): The opposite side.

The selective etching technique is probably the quickest method to reveal if periodic domain reversals have taken place. The etchant does not attack the b-face and the domain growth is, hence, not revealed. To be able to visualize the growth of the domains in the depth of the sample, the sample has to be polished with a wedge relative to the c-face prior to etching. This, however, is inconvenient and complicated and it also destroys the sample.

When one has multiple grating structures on a single substrate, it has been found particularly convenient to use surface etching as an indicator of the poling result. Fig. 6.7 shows a tandem grating of PPKTP poled with two different periods, 6.99 µm and 9.01 µm, respectively. The crystal was used to simultaneously generate 532 nm and 491 nm by SHG (from1064 nm) and SFG (from 914 nm and 1064 nm).

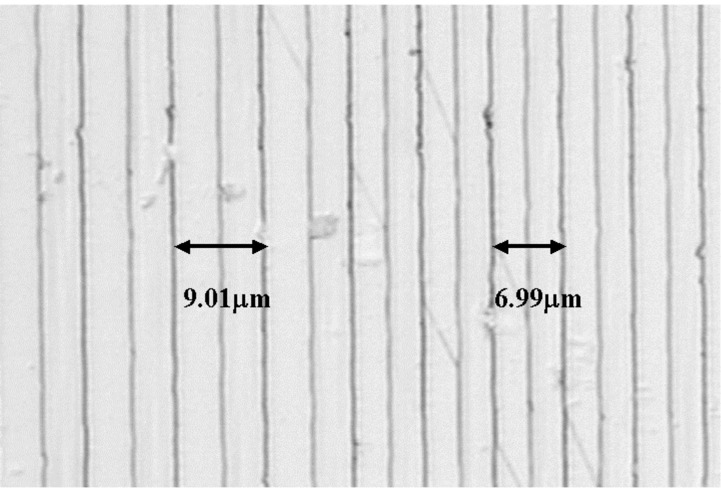

Fig. 6.7 Etched PPKTP with two grating periods, 6.99 µm and 9.01 µm, on a single KTP substrate.

6.3.3. Atomic Force Microscopy

An Atomic Force Microscope (AFM) consists of a very sharp tip mounted on the end of a tiny cantilever spring which is moved by a mechanical scanner over the surface to be observed. When the tip is brought to the surface of the sample, the cantilever will bend or deflect due to the force between the tip and the sample surface. The deflection of the cantilever can be monitored by collecting a laser beam reflected by the end of the cantilever onto a position-sensitive photodetector. By measuring the cantilever deflection during the scanning, a three-dimensional map of the surface topography can be obtained through an electronic feed-back loop. When the distance between the tip and the sample is reduced to shorter than one nanometer, the AFM is operated in a so-called contact mode.

In voltage-modulated AFM, so-called a piezoresponse-AFM, an ac electric field is applied between an Au-coated tip and the sample, such as KTP. The sample surface will oscillate when it is in contact with the tip, due to the inverse piezoelectric effect. The tip will follow the surface oscillations and the amplitude, as well as the phase of these oscillations can be detected using a lock-in amplifier. Recently, the piezoresponse-AFM has been proved to be a powerful technique for investigating the domain structures with high resolution on the polar faces[18], as well as on the non-polar faces[19].

In the case of sample detection on the polar surface, the surface movement, Δz, is governed by the piezoelectric coefficient, d_{33}, according to the expression:

$$\Delta z \propto d_{33}\,\mathrm{sgn}(P_s)V_0\cos(\omega t) \qquad (6\text{-}3)$$

where $\mathrm{sgn}(P_s)$ represents the sign of the polarization P_s, and V_0 and ω are the amplitude and the oscillation frequency of the applied voltage, respectively.

A phase shift of the piezoelectric response at ω, characterizes the sign of the polarization vector. For periodically inverted domains in ferroelectrics, such as PPKTP used in my studies, the phase of the vertical deflection for one domain (with $-P_s$) will be out of phase 180°, respective to the adjacent domain (with $+P_s$).

In the case of sample detection on the non-polar faces, where the polarization vector is perpendicular to the applied electric field, there will be no piezoelectric deformation along the direction of the applied field. However, an in-plane movement can be induced through the shear strain in the KTP crystal, brought about by the nonzero piezoelectric coefficient, d_{24}. Consequently, this in-plane movement results in an oscillating lateral deflection of the cantilever via the fraction force. The size of the lateral deflection, ΔL, is expressed as follows:

$$\Delta L \propto d_{24}\,\mathrm{sgn}(P_s)V_0\cos(\omega t) \qquad (6\text{-}4)$$

The in-plane movement is phase-shifted for the domains with opposite polarization. The phase-shift can also be detected with a lock-in amplifier.

Our studies of domain structure were performed on a commercial AFM. An ac voltage of 20 V at a frequency of 93.2 kHz was applied to the Au-coated tip while it scanned the PPKTP surface in the contact mode. The experiment set-up is show in Fig. 6.8. Fig. 6.8a shows the scanning on the polar face while Fig. 6.8b shows how the measurement is performed for the non-polar surface.

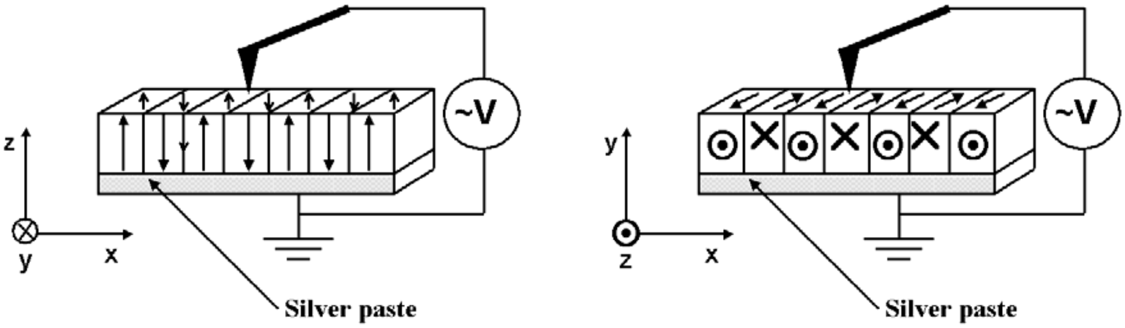

(a) (b)

Fig. 6.8 Experimental set-up for studying the domain structure via the AFM method. An ac voltage is applied to the tip while it scans in contact with (a) the z-face, and (b) the y-face of the crystal.

Using this technique, domain broadening and the related changes of the duty cycle are investigated while scanning on the polar c-face (see Fig 6.5). Domain propagation and the morphology were studied from AFM scans on the non-polar face (see Fig. 6.4).

In conclusion, AFM is a powerful informative tool for investigating the domain reversal processes in a non-destructive way. There is no need for angle polishing in the case of the non-polar face detection. Furthermore, the measurement has a very high accuracy since the spatial resolution is around 1 nm. However, the measurement is time consuming and only a small area is probed at a time which may limit the usage of this technique.

6.3.4. Temperature and wavelength tuning

As we discussed in Chapter 4, the characteristics of the temperature and the wavelength tuning of the SHG process serve as the quality measure of a periodically-poled crystal. A loosely focused fundamental beam should be used when performing the tuning measurements, in order to avoid the influence of beam divergence and, thus, ensuring approximately constant phasematching condition throughout the crystal.

As an example of the bandwidth measurements, in the following I will present the results of the dependence of the phasematching characteristics on the crystal temperature for frequency doubling of a CW Nd:YAG laser at 1064 nm in a single-pass set-up, see Fig. 6.9. The laser beam was focused in the crystal to a spot size of approximately 44 μm. The illustration shows the temperature tuning curve for a PPKTP crystal with a period of 9.01 μm (Paper I). The solid line is a theoretical sinc^2 function, which fits the experimental data well, including the sidelobes. This fit confirms that a high-quality QPM structure was indeed obtained. From the measured temperature bandwidth of 6.1 ^{o}C, we estimated the effective crystal length to be 7.7mm, which is very close to the physical crystal length of 8 mm.

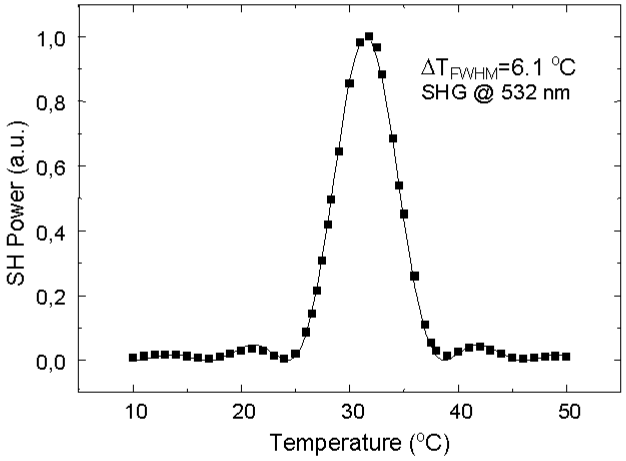

Fig. 6.9 SH power (a.u.) as a function of the temperature of a PPKTP crystal with a period of 9.01μm. The solid line is a sinc^2 fit.

In Paper VII, we also performed a temperature tuning for a PPRKTP crystal with a period of 6.81 μm and for a cyan-colour generation at 488 nm using a CW Ti:sapphire laser. A temperature bandwidth 4 °C gave also here rise to a 7.7 mm effective length, which was close to the physical length of 8.5 mm. For the same effective crystal length, we can thus see that the temperature bandwidth is wider for a longer fundamental wavelength, in a good agreement with theory, as discussed in Chapter 4.

The uniformity of the poled structure can, of course, also be evaluated for a type-II SHG process by either temperature or wavelength tuning in the same way. In Fig. 6.10, we demonstrate the latter type of tuning in an example of a "green" PPKTP crystal with a period of 9.01 μm which was evaluated with a CW Ti-sapphire laser (Paper III). The wavelength bandwidth of the phasematching peak at 797.6 nm was 0.12 nm, corresponding to an effective crystal length of 8 mm which was very close to the physical crystal length of 8.5 mm. Again, this indicates that the poled crystal had an uniform periodicity over the length of the crystal.

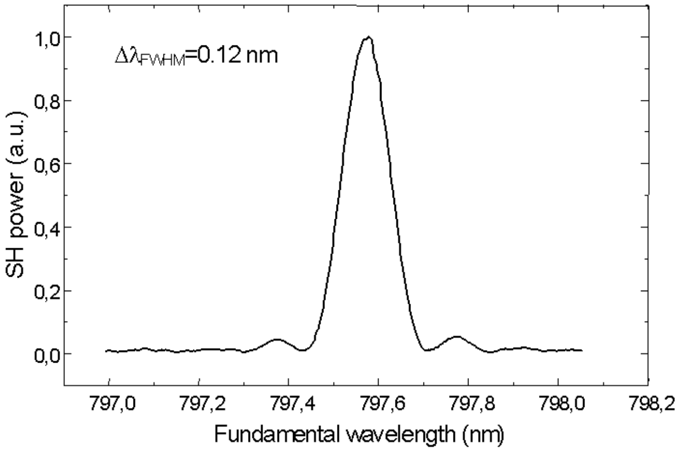

Fig. 6.10 SH power(a.u.) as a function of the fundamental wavelength for first-order type-II UV generation. The wavelength bandwidth is $\Delta\lambda_{FWHM} = 0.12\ nm$.

Temperature and wavelength tuning, as described above, are widely used for characterizing the uniformity of the periodicity of the domains and are considered an adequate methods for determining the phasematching characteristics. However, a single measurement of this kind only provides the uniformity information in a local area where the laser beam passes.

6.3.5. Effective nonlinear coefficient

As was discussed in Chapter 3, in the QPM process, the effective nonlinear coefficient is given by:

$$d_{eff} = \frac{2d_{il}}{m\pi} \tag{6-5}$$

where m is the order number and d_{il} is the appropriate nonlinear coefficient. For KTP crystals, the highest efficiency is obtained when the d_{33} coefficient is utilized. The quality of a poled crystal is known after a comparison is made of the experimentally-obtained efficiency with the theoretical value. In the low-power regime, with confocal focusing, the effective nonlinear coefficient is obtained by reversing Eq (4-9), viz:

$$d_{eff} = \sqrt{\frac{\pi n_F^2 n_{SH} \varepsilon_0 c^3}{2\omega_F^2 k_F L h(B,\xi)} \times \frac{P_{SH}}{P_F^2}} \tag{6-6}$$

For example, in Paper I, several “green” crystals poled from KTP have displayed effective nonlinear coefficients of around 10.5 pm/V, which is very close to the theoretical figure when $d_{33} = 16.9\,pm/V$ [20] is used for the first-order SHG.

The same type of evaluation was also performed for RKTP. In Paper VII, three crystals of length 8.5 mm with periods of 5.27 μm, 6.095 μm, and 6.81 μm, respectively, were investigated. The experimental parameters have been given in Section 5.4. All of these crystals have an effective nonlinear coefficient of approximately 10.3 pm/V, which indicates that these PPRKTP crystals have been poled with very high quality too.

In Paper II, we studied the generation of UV light through a type-I QPM SHG from a 2.95 μm-period PPKTP crystal, pumped by a Ti:sapphire laser at 780 nm. 450 μW of SH power was generated from 270 mW of incident fundamental power. Taking into account the focusing condition, the effective nonlinear coefficient was calculated to be 5.5 pm/V. The smaller figure, compared to those given above, indicates that the sample was poled with non-optimized quality due to either missing domains, merged domains or error in the duty cycle, or all of these reason at the same time.

As a conclusion, we can say that measurements of SH power are an effective way to evaluate the crystal homogeneity over the whole aperture by scanning the pump beam horizontally and vertically. It is, actually, a very useful technique for screening PP samples even in an industrial production line. However, it is worth to note that this method provides information only on the effective nonlinearity integrated along the optical beam. One needs to combine it with selective etching or AFM method in order to obtain the full detailed information on the uniformity we want.

6.3.6. Three-dimensional characterization of the effective nonlinearity

To date, we still have KTP and RKTP materials with some variations in the stoichiometry. This often results in non-uniform poling, such as the local deviation in the duty cycle and/or missing domains. In this case, the local SH efficiency can vary substantially over the length of the crystals. A three-dimension mapping of the nonlinearity by measuring the SH output point by point, will provide additional information on the poled crystal quality. To be able to measure the effective nonlinear coefficient locally with a high longitudinal, spatial resolution, type-II QPM SHG with ultrashort pulses comes into the picture.

In type-II SHG using ultrashort pulses, the two orthogonal fundamental components travel at different group velocities and, therefore, they will separate after a certain distance, i.e., the walk-off length, as we discussed in Section 4.5. The walk-off distance will determine the spatial resolution along the beam propagation.

To measure the effective nonlinear coefficient point by point inside the crystal, we need to properly delay the fast-traveling fundamental component before the beam enters into the crystal in order to generate maximum SHG at each point. The x-coordinate of the measured point inside the crystal, x_c, is a function of the delay length, x_d, given by the expression:

$$x_c = \frac{x_d}{n_g^z - n_g^y} \tag{6-7}$$

where n_g^y and n_g^z are the group indices of the y-and z-polarized fundamental pulse.

The sample which was used to demonstrate this technique, was a 4 mm-long and 1 mm-thick PPKTP crystal with a 9.01 μm period. Fig. 6.11 shows the experimental set-up. A Ti:sapphire laser, generating 80 fs pulses at a repetition rate of 80 MHz, served as the fundamental source. The central fundamental wavelength was set to 795 nm for a first-order type-II SHG utilizing the d_{24}-coefficient. Pre-chirping by double-passing through the prism pair is used to compensate for the pulse broadening induced by the optics before entering the PP sample. By adjusting the distance between the two prisms, the 80 fs pulse duration after Lens 1 was ensured. A λ/2 plate was used to set the polarization of the fundamental wave at 45° relative to the polar axis of the PPKTP. The polarizing beam splitter P1 separates the z- and the y-components. The y-component of the fundamental pulse has a higher group velocity in KTP and, thus, it was the one component which was delayed. The second polarizing beam splitter, P2, was used to recombine the two beams. The recombined beams were weakly focused into the crystal to a 300 μm beam diameter. The generated SH distribution was imaged by Lens 2 onto a CCD camera. 3D-mapping of the effective nonlinearity was then obtained by translating the delay stage and taking subsequent CCD pictures of the 2D SH power distribution. Appropriate filters were used to adjust the SH signal and to avoid saturation of the camera. The background of the non-phasematched type-I SHG was subtracted from the measured total SH power and the square-root of the SH intensity was calculated, which is proportional to the effective nonlinearty, d_{24eff} we are interested in.

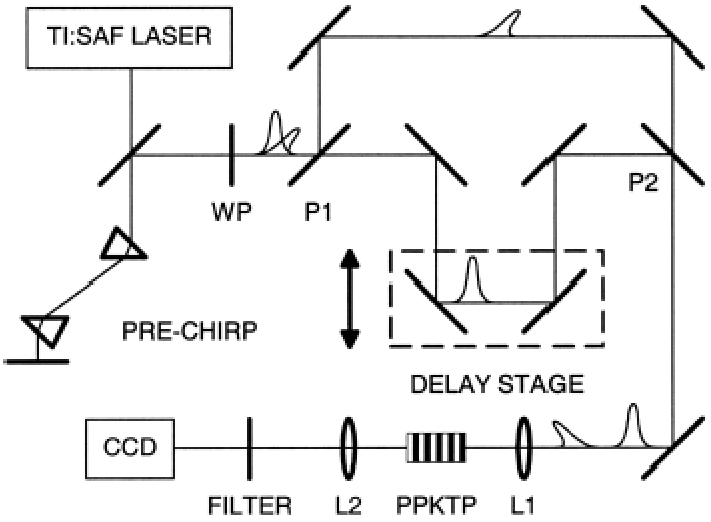

Fig. 6.11 Experimental set-up for measuring the local effective nonlinearity, d_{eff}.

Fig. 6.12 shows four different frames of the nonlinearity distribution taken from the CCD camera. The subsequent frames are separated by 0.75 mm. The grey scale is proportional to the local value of d_{eff}. It is quite clear that the effective nonlinearity varies along the length of the crystal.

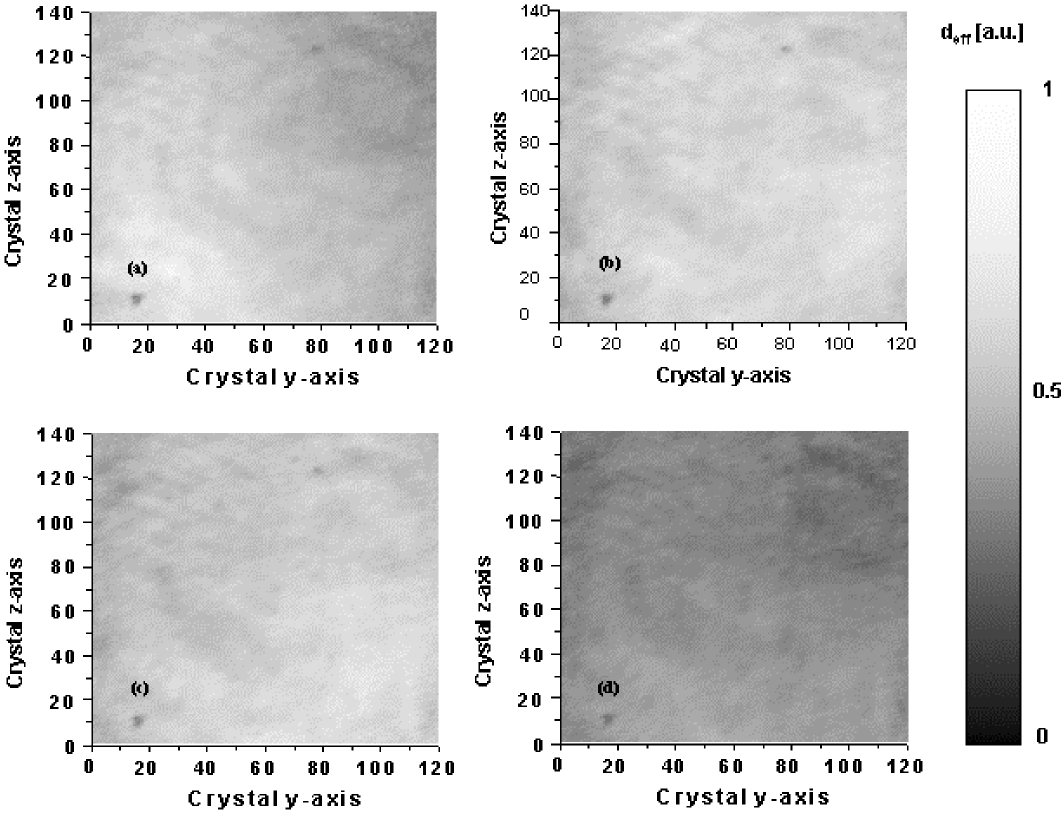

Fig. 6.12 The measured SH distribution converted to the effective nonlinearity, d_{eff}, in PPKTP. The distance between subsequent frames is 0.75 mm along the grating vector of the PPKTP sample.

It is assumed that d_{33eff} will follow the same variation as the one for d_{24eff}. The absolute values of the local effective nonlinear coefficient, $d_{33eff}(x)$, were obtained by calibrating the $d_{24eff}(x)$ dependence to the known value of d_{33eff} figure, as measured from a type-I CW SHG experiment. Fig. 6.13 shows the distribution of the effective nonlinearity, d_{33eff}, along the crystal length obtained in this way.

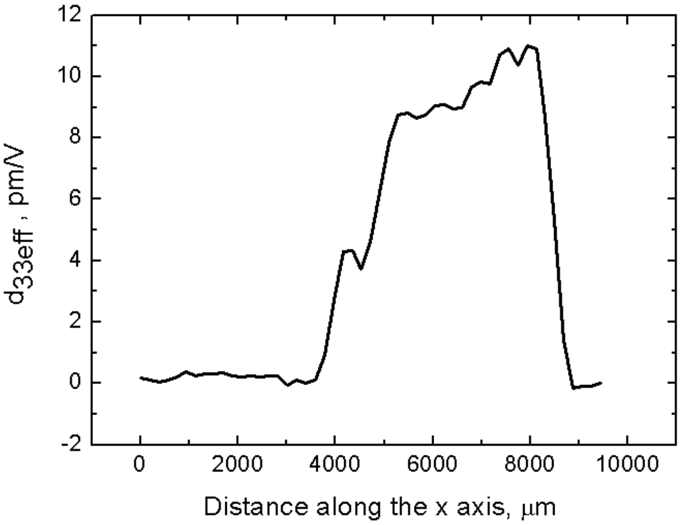

Fig. 6.13 Distribution of the effective nonlinearity d_{33eff}, along the crystal length.

This method can be widely used for any PP material. More importantly, it provides the possibility to characterize the effective nonlinear coefficient for a complicated grating structure, such as a chirped grating or a tandem grating (see, for instance, Fig. 6.7).

References of Chapter 6

[1] R. Stolzenberger and M. Scripsick, Proc. SPIE **3610**, 23 (1999).

[2] J. D. Bierlein and F. Ahmed, Appl. Phys. Lett. **51**, 1322 (1987).

[3] R. Miller and G. Weinreich, Phys. Rev. **111**, 1460 (1960).

[4] G. Rosenman, A. Skliar, and M. Katz, Appl. Phys. Lett. **73**, 3650 (1998).

[5] H. Karlsson, F. Laurell and L. K. Cheng, Appl. Phys. Lett. **74**, 1519 (1999).

[6] S. Wang, Licentiate Thesis, TRITA-FYS 2185, ISSN 0280-316X, (1999).

[7] V. Gopalan, T. E. Mitchell, Y. Furukawa and K. Kitamara, Appl. Phys. Lett. **72**, 1981 (1998).

[8] K. Kitamara, Y. Furukawa, K. Niwa, V. Gopalan and T. E. Mitchell, Appl. Phys. Lett. **72**, 3073 (1998).

[9] P. A. Morris, A. Ferreti, J. D. Bierlein and G. Loiaconno, J. Cryst. Growth **109**, 367 (1990).

[10] G. Rosenman, P. Urenski, A. Arie, M. Roth, N. Angert, A. Skliar and M. Tseitlin, Appl. Phys. Lett. **76**, 3798 (2000).

[11] Q. Jiang and P. A. Thomas, J. Appl. Phys. **92**, 2717 (2002).

[12] V. Shur, E. Rumyantsev, R. Batchko, G. Miller, M. Fejer, R. Byer, Ferroelectrics **221**, 157 (1999).

[13] T. Y. Fan, C. E. Huang, B. Q. Hu, R. C. Eckardt, Y. X .Fan, R. L. Byer, and R. S. Feigelson, Appl. Opt. **26**, 2390 (1987).

[14] A. Fragemann, V. Pasiskevicius, J. Nordborg, J. Hellström, H. Karlsson and F. Laurell, Appl. Phys. Lett. **83**, 3090 (2003).

[15] M. E. Lines and A. M. Glass, “Principles and Applications of Ferroelectrics and Related Materials”, Clarendon Press, Oxford (1997).

[16] F. Laurell, M. G. Roelofs, W. Bindloss, H. Hsiung, A. Suna and J. D. Bierlein, J. Appl. Phys. **71**, 4664 (1992).

[17] W. J. Liu, X. R. Huang, X. B. Hu, and C. Z. Ge, Appl. Phys. Lett. **68**, 25 (1996).

[18] J. Wittborn, C. Canalias, K. V Rao, R. Clemens, H. Karlsson and F. Laurell, Appl. Phys. Lett. **80**, 1622 (2002).

[19] C. Canalias, V. Pasiskevicius, A. Fragemann and F. Laurell, Appl. Phys. Lett. **83**, 734 (2003).

[20] H. Vanherzeele and J. D. Bierlein, Opt. Lett. **17**, 982 (1992).

7. Laser-induced damage in KTP

7.1. *Introduction*

Laser-induced damage in crystals is a detrimental effect for nonlinear frequency converters. Particularly, photorefractive and photochromic effects, like grey tracking and green-induced infrared absorption (GRIIRA), will limit the performance of high-power operating SHG devices in the UV and the visible spectrum. Different materials have different damage thresholds, which are complex functions of wavelength, peak intensity, average power, temperature, exposure duration and processing history of the crystal. Some of these negative effects can be mitigated at elevated temperatures but the lifetime of these materials may still be limited.

7.2. *Photorefractive effect*

Photorefraction is a light-induced change of the refractive index. In a photorefractive material, photocarriers are generated in the irradiated volume. These photocarriers will drift away from the beam volume and thereby generate a space-charge field, which will induce a refractive index change through the electro-optic effect. Consequently, the laser beam experiences a spatial distortion in the crystal. The distortion can manifest itself in various ways like a phase modulation, a beam break-up, and Bragg scattering. Ferroelectrics such as LN, is know to suffer severely from photorefractive damage, particularly at visible wavelengths[1]. To minimize this effect, both experimental and theoretical solutions have been proposed, such as 1) operating the samples at elevated temperature[2]; 2) doping the crystal with magnesium oxide or 3) make the LN more stoichiometric. As we already have discussed in Chapter 5, the increased damage threshold by means of the second and third method is still not high enough to get efficient and stable SHG devices operating at room temperature. Several studies have shown that the periodic poling can reduce the photorefractive effect in LN[3,4]. This might be due to a cancellation effect in the adjacent domains with opposite direction of the spontaneous polarization[5]. On the other hand, the main material type of our own investigation, KTP and its isomorphs, have a low susceptibility to photorefractive damage benefiting mainly from the high ionic conductivity, which will screen any generated bulk field. It has been reported that several watts of frequency doubled visible light can be generated stably in PPKTP operating at room temperature[6,7,8].

7.3. *Photochromic effect*

Although the quality of KTP has been improving, so far, the ordinary flux-grown KTP still faces an aging problem due to photochromic damage, i.e., grey tracking and/or green-induced infrared absorption. A better understanding of the damage mechanisms may lead to a reduction of these effects through a better choice of operating parameters as well as improved crystal growth.

7.3.1. Grey tracking

Grey tracking was initially observed in the experiments with high-efficiency frequency doubling of 1064 nm[9,10,11,12,13,14] and in optical parametric oscillator pumped at 532 nm[15]. Many different types of experiments have been done to study grey tracking. It has been by visual observation of the bulk darkening and beam distortion, spectral transmission and absorption measurements[10,11,12,16] as well as by electron-spin-resonance (EPR) spectra which were measured before and after laser irradiation[17]. The predominant feature of grey tracking has been identified as a reduced optical transmission over the visible range (400 nm – 700 nm). Continued operation after the formation of grey tracks can lead to catastrophic damage of the crystals.

Mechanisms for grey tracking were proposed by Scripsick *et al*[18,19] and Mürk *et al*[20]. We now briefly recaptulate these suggestions and start with Scripsick's model. Laser beam radiation in KTP produces photocarriers in the volume of the beam. Then, the electrons and holes will drift apart and become trapped separately by the defects in the crystal. As a result, the electrons are trapped by the Ti^{4+} ions, located adjacent to oxygen vacancies, and Ti^{3+} centres are created. Impurities, such as Fe^{2+}, will trap the holes and be converted to Fe^{3+}. These new centres give, in turn, rise to broad and partially overlapping absorption bands around 420 nm and 510 nm, respectively. At the same time, a possibility exists for hole capture in the vicinity of the oxygen ion in the perturbed Ti-O-Ti chain, which is stabilized by a potassium vacancy $V(K^+)$. Mürk *et al* suggested that Frenkel defects made from interstitial K^+_i and $V(K^+)$ can capture the free carriers (hole and electrons) and to create colour centres. In KTP, optical creation of potassium interstitials and vacancies, acting as Frenkel defects, has a rather low threshold value due to a relatively low activation energy of 1.4 eV required for their creation and provided by a nonradiative decay of the TiO_6 vibration modes.

The susceptibility to grey tracking depends on the crystal quality and, hence, directly on the crystal growth condition and growth method[11,21]. It has been demonstrated that the damage is stronger when the laser beam has a polarization along the polar axis of KTP[13] and that the magnitude of the damage has a nonlinear dependence on the intensity of the laser beam, which induced the damage[12]. The relaxation of the damage depends on the operating conditions[14,22]. Furthermore, grey tracking is removable by heating the crystals[10,12].

7.3.2. Green-induced infrared absorption

Green-induced infrared absorption is an increase of the infrared absorption in the presence of green light. It is related to colour centre formation, mentioned in the previous section.

7.3.2.1. Technique for GRIIRA measurement

The common-path interferometer is a sensitive technique for measuring absorption in weakly absorbing materials. Variants of this technique have previously been used for high-sensitivity absorption measurement[23,24]. In our study, we employed the collinear configuration to measure the absorption. Fig. 7.1 shows the experimental set-up.

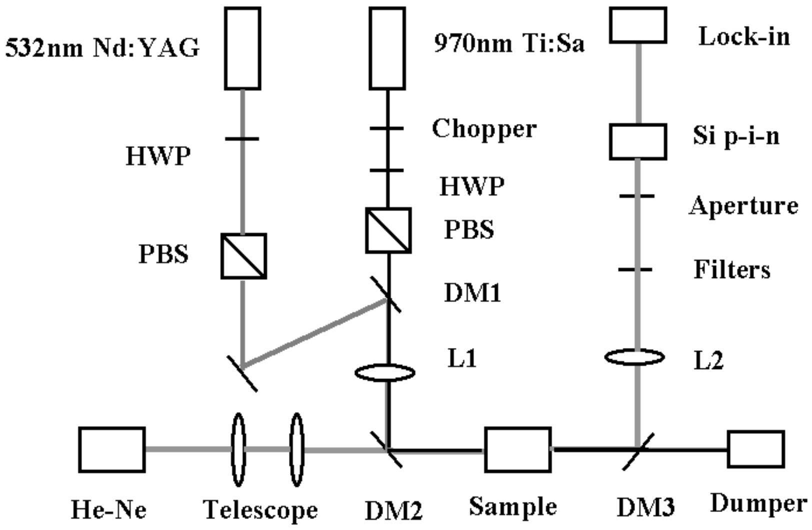

Fig. 7.1 The principle set-up for the common-path interferometer used in the absorption measurement of GRIIRA.

Three laser beams, a probe beam at 633 nm (He-Ne), a pump beam at 970 nm (Ti:Sapphire) and a grey-track inducing beam at 532 nm from a Q-switched and frequency-doubled Nd:YAG (pulse length of 5 ns, repetition rate of 20 Hz), were combined by dichroic mirrors DM1 and DM2 and propagated collinearly into the sample. The pump and the probe beam diameters were 35 µm and 350 µm, respectively. The infrared and the absorption-inducing green beams were polarized parallel to the crystal z-axis. This polarization is the most commonly used in applications with periodically poled KTP. Moreover, it has been reported that grey-tracking is most pronounced for z-polarized green light. The 970 nm pump beam had a power of 800 mW and was mechanically chopped. The thermal lens caused by the absorption of the infrared pump beam causes spatial distortion of the phase front in the co-propagating probe beam. This phase distortion can be transferred into a modulation of the transverse beam intensity in the Fourier plane. A spatial Fourier transform of the probe beam is, hence, obtained by lens L2. The modulation of the probe beam intensity at the chopping frequency of the pump (10 Hz) was detected by a Si p-i-n detector located behind a 90 µm circular aperture placed in the Fourier plane. The dynamic range of the lock-in amplifier (SRS 530) was 40 dB and the pump modulation frequency was chosen low enough for thermal equilibrium to be established in the KTP sample. Also, special care was taken to prevent direct and scattered infrared pump light reaching the detector by using a dichroic mirror, DM3, two BG-18 and one OG-590 glass filters, and by placing the detector into an enclosure.

7.3.2.2. Theoretical analysis of GRIIRA

Here, we start with an analysis to show how the thermal lens relates to the induced absorption. To simplify the analysis, we use a cylindrical geometry with radial coordinate *r* and estimate the temperature distribution in the sample resulting from the absorption of the infrared pump beam which propagates along the x-axis. The temperature distribution, T(r), can be obtained by solving the one-dimensional heat conduction equation:

$$\frac{\partial^2 T}{\partial r^2} + \frac{1}{r}\frac{\partial T}{\partial r} + \frac{Q(r)}{\kappa} = 0 \qquad (7\text{-}1)$$

where $Q(r) \approx \alpha I_0(r)$ is the absorbed power density of the infrared pump with intensity $I_0(r)$, κ is the heat conductivity of the material. (For KTP, $\kappa = 0.13 W/cm/K$)[25] and α is the absorption coefficient of the material. For the boundary conditions at the crystal surfaces, where $r = r_b$, we will assume that the temperature, $T(r_b, x)$ is constant. We then can get the solution for Eq (7-1) as follows[26]:

$$\Delta T(r,x) = \frac{\alpha P \exp(-\alpha x)}{4\pi\kappa}\left[\ln\left(\frac{r_b^2}{r^2}\right) + E_1\left(\frac{2r_b^2}{w_p^2}\right) - E_1\left(\frac{2r^2}{w_p^2}\right)\right] \qquad (7\text{-}2)$$

where $\Delta T(r,x) = T(r,x) - T(r_b,x)$ is the temperature rise at a point $r < r_b$ and P and w_p are the infrared pump power and beam radius, respectively. E_1 represents anexponential integral function. Fig. 7.2 shows the calculated temperature distribution $\Delta T(r,z)$ caused by the absorption (α = 10^{-4} cm^{-1}) of the pump beam along with the probe beam profile. 0.9 W of pump power was used in the calculation.

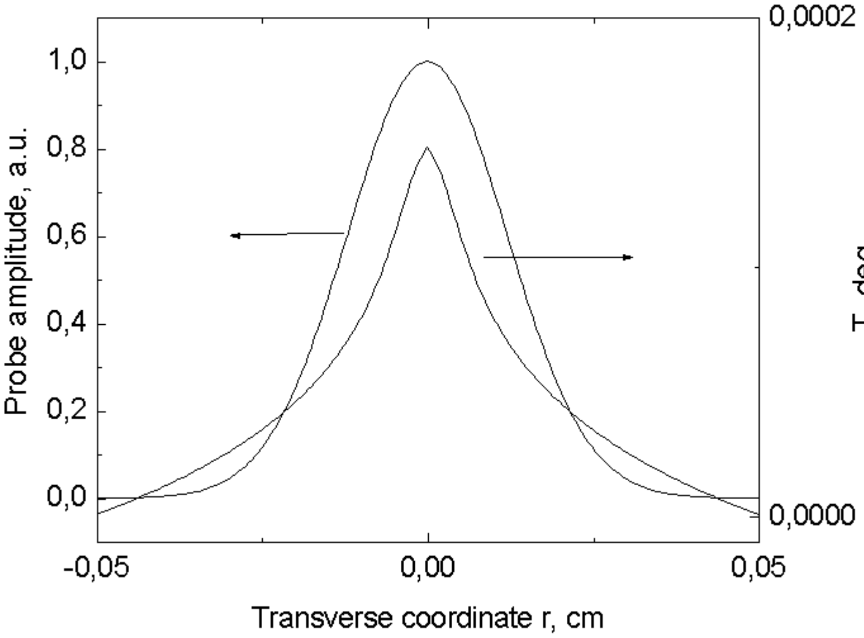

Fig. 7.2 The probe beam amplitude and the simulated temperature distribution in KTP.

The probe beam passing through the crystal at the point acquires a transversal phase profile given by:

$$\Delta\varphi(r) = 2\pi\left[T(r) - T(0)\right]\frac{L}{\lambda}\frac{dn}{dT} \qquad (7\text{-}3)$$

where dn/dT is the temperature dependence of the refractive index.

The spatial distribution of the signal voltage measured by the lock-in amplifier while scanning the aperture in the Fourier plane can be expressed as:

$$U(r) = \left[P_p(r)\Big|_{\Delta\varphi=0} - P_p(r) \right] \eta R \gamma \tag{7-4}$$

where $P_p(r)$ and $P_p(r)\Big|_{\Delta\varphi=0}$ are the probe-beam power distributions in the Fourier plane with the infrared beam open and closed, respectively. The factors η, R, γ are the responsivity of the p-i-n detector (0.6 A/W), lock-in load resistance (100 MΩ), and the probe beam attenuation factor in the optical system (about 0.02), respectively.

When only the infrared beam was used to induce the absorption, we detected a maximum absorption at the outer edge of the aperture while the modulation in the centre was very weak. This rather strange behaviour is due to the fact that the thermal lens is rather weak and the modulation in the centre is completely masked by the noise of the probe beam. To try to explain this, we have performed a simulation of the distribution of the probe beam in the Fourier plane considering the probe laser noise in the calculation. Assuming that the power distribution of the probe laser noise is equal to $\delta P_p(r)\Big|_{\Delta\varphi=0}$, the SNR can be expressed as:

$$SNR(r) = D \frac{U(r)}{\delta P_p(r)\Big|_{\Delta\varphi=0} \eta R \gamma + U_N} \tag{7-5}$$

where D is the dynamic diapason (40 dB) of the lock-in amplifier and U_N is the sum of the electrical noise of the detector and lock-in amplifier. Fig. 7.3 shows the calculated distribution of the SNR for several infrared absorption coefficients given in the figure, by using the experimentally measured values of $\delta = 0.005$ (rms noise of the probe laser) and $U_N = 15$ µV. As can be seen by these results, the maximum of the lock-in signal should be observed on the wings of the distribution.

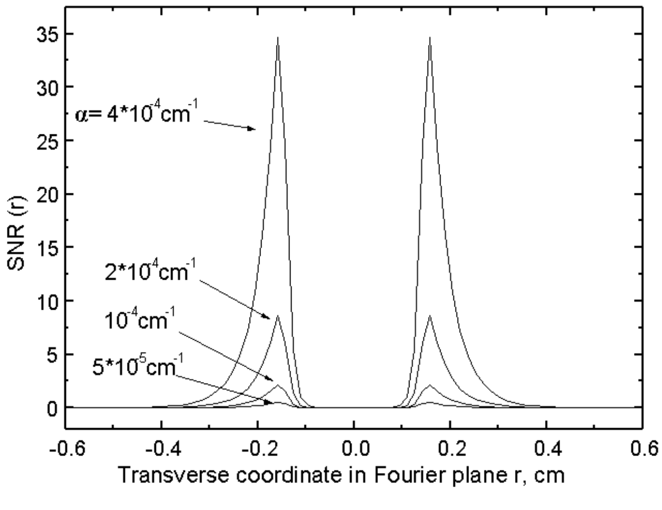

Fig. 7.3 The radial distribution of the signal-to-noise ratio in the Fourier plane for different infrared absorption coefficients, α.

In order to obtain absolute values of the absorption in KTP, we calibrated the set-up by using a 1 cm-long piece of BK7 optical glass (Schott glass BK7 517642) with well-known properties. For the known material parameters, the absorption coefficient for KTP can be calculated from:

$$\alpha_{KTP} = \alpha_{BK7} \sqrt{\frac{S_{KTP}}{S_{BK7}} \frac{(dn/dT)_{BK7} \kappa_{KTP} L_{BK7}}{(dn/dT)_{KTP} \kappa_{BK7} L_{KTP}}} \tag{7-6}$$

where S_{KTP} and S_{BK7} are the maximum lock-in signals as measured in KTP and BK7, with respective lengths, L_{KTP} and L_{BK7}, respectively. κ_{KTP} and κ_{BK7} are the thermal conductivity coefficients of KTP and BK7, respectively. The infrared pump-power was held constant throughout the measurements. From these measurements, we established that the sensitivity limit for the current set-up was about 10^{-5} cm^{-1}, which was adequate for the KTP material used in this work. Higher sensitivity could, of course, be obtained by increasing the infrared pump power.

7.3.2.3. Absorption features of KTP and PPKTP

We have compared the absorption dynamics for KTP and PPKTP. To minimize the wafer variation effects and to obtain comparable results between KTP and PPKTP, both KTP and PPKTP were made on the same substrate. By translating the sample along the y-axis, we can easily switch the position of the beams from the KTP region to the PPKTP region. Fig. 7.4 illustrates the arrangement for both KTP and PPKTP.

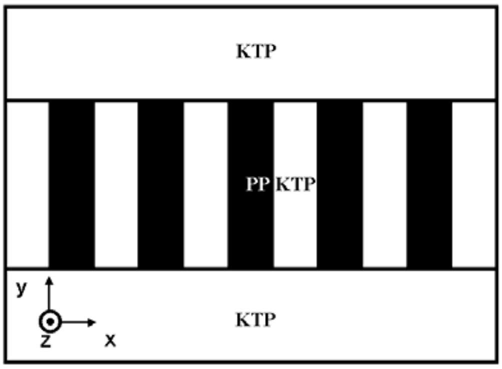

Fig. 7.4 Illustration of how KTP and PPKTP are made on the same substrate.

For PPKTP, the grating periods varied from 6 to 35 µm, which were neither producing QPM interaction for the pump-beam, nor for the colour-centre-induced green beam. Some of these samples had also been used in other unrelated experiments earlier and, thus, we annealed them for several hours at 200^{o}C in air to remove any residual absorption remaining from the earlier treatment. The rest of the samples were as-poled.

Starting with the near-infrared pump absorption only, i.e. without the 532 nm light illumination, the measured absorption coefficients were the same in KTP and in PPKTP (about 2×10^{-4} cm^{-1}), showing that the linear material properties had not been modified by poling. This also indicated that the electric-field poling does not introduce additional absorption centres related either to impurities or to colour centres formed by electrochromic damage.

Secondly, the dynamics of the absorption coefficient in KTP and in PPKTP was recorded during and after illumination of the samples with the colour-centre-inducing 532 nm beam. The maximum peak intensity of this beam was 320 MW/cm^2. The infrared absorption increased exponentially in both KTP and in PPKTP. Fig. 7.5a shows the absorption increase with a time constant of 1.3 s while illuminating samples. It is important to note that the induced absorption was consistently larger by 30 - 50% in the poled regions of the samples.

After the 532 nm beam was blocked off, the GRIIRA relaxation traces were recorded for KTP and for PPKTP as shown in Fig. 7.5b. It can be seen that one of the specific features of PPKTP is that the fast relaxation is absent as compared with KTP. KTP displays a double-exponential decay with a initially fast relaxation with a time constant of 20 s and a slower contribution with a time constant of 130 s, while the GRIIRA relaxation curve of PPKTP follows a single-exponential decay with a time constant of 180 s.

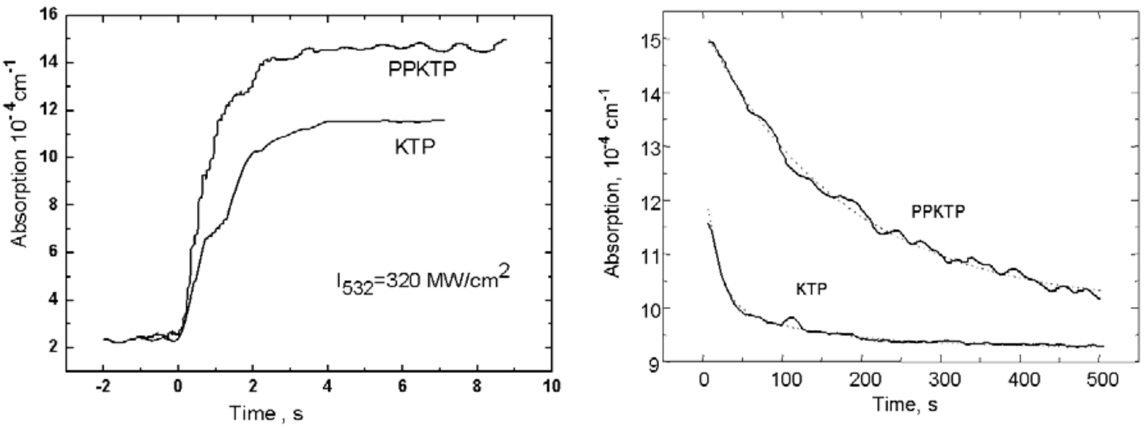

a **b**

Fig. 7.5. Temporal growth and decay of the GRIIRA signal in KTP and in PPKTP. (a):The GRIIRA grew exponentially in KTP and in PPKTP with a time constant of 1.3 s when the sample was illuminated with 320 MW/cm^2. (b):The GRIIRA signal decay on the short time-scale for KTP and PPKTP after the 532 nm beam was blocked.

To explain the difference between the dynamic absorption features of KTP and PPKTP, we need to investigate how the poling process could have contributed to the performance, primarily from a defect point of view.

The poling procedure is associated with the spatial redistribution of the K^+ ions in the lattice due to the vacancy-assisted ionic conductivity. One should expect an increase in the concentration of the native potassium-related defects like $V(K^+)$ and K_i^+. They will act as stabilizing defects for the O^{2-}/O^- hole trap and the Ti^{4+}/Ti^{3+} electron trap, respectively. At least, the latter is reported to have optical transitions in the near infrared[20]. Therefore, there are more possibilities for colour centres to be formed in the poled materials than in the virgin material, which would explain the observed higher amplitude of GRIIRA.

The faster initial relaxation of the infrared absorption induced at higher peak powers of the 532 nm beam in KTP, see Fig. 7.5b, would point to the appearance at higher green-light intensities of new and less stable carrier trapping centres, which therefore relax with a higher rate. One possible candidate here could be a Frenkel-defect pair, K_i^+ - $V(K^+)$, which is characterized by a low activation energy of only 1.4 eV, and might be created during the local heating of the lattice at higher green-light intensities[20]. Each ion in the Frenkel-defect pair can, in turn, stabilize the electron, or the hole trap, forming a new colour centre. Due to localization and the low activation energy of the Frenkel-defect pairs, the related colour centres are expected to decay at high rates. The absence of a correspondingly fast decay for PPKTP can be explained by a higher initial concentration of the slower-relaxing, “stable” trapping centres present in the poled materials.

It was found that the GRIIRA signal decay rates increased strongly for temperature above 85°C. Table 7.1 shows the GRIIRA decay rate at different temperatures. This rapid increase in the relaxation rate with temperature can be associated with a dissociation of the colour centre brought about by the increasing thermal population of the phonons of the TiO_6 group at 270 cm^{-1} at temperatures above 80 °C. This is also evidenced by the decreasing efficiency of the stimulated Raman scattering in KTP at these temperatures[27].

Temperature (°C)	**Relaxation time constant (min)**
85	31
95	17
115	9

Table.7.1 The relaxation time constants as a function of the KTP temperature.

Another striking feature is observed in the as-poled KTP. Fig. 7.6 shows a typical GRIIRA trace in as-poled PPKTP.

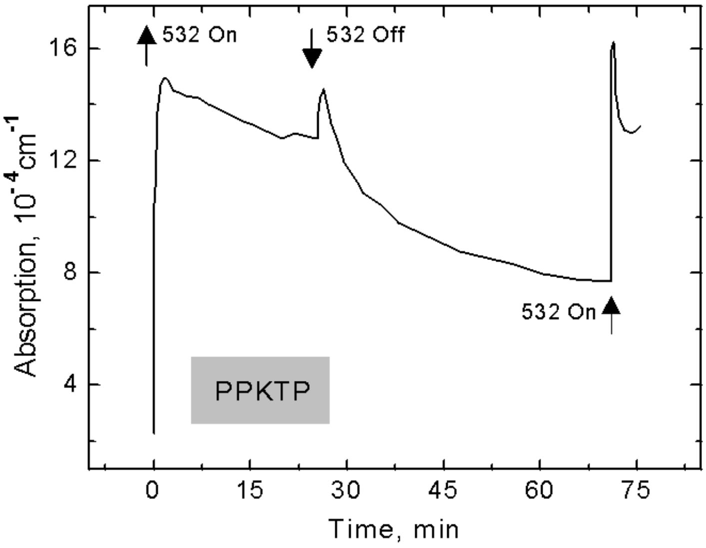

Fig 7.6 The GRIIRA dynamics in an as-poled PPKTP sample. Arrows going up and down mark the moments when the 532 nm beam is opened and closed, respectively.

The infrared absorption shown here shows several characteristic overshoots: first, after switching on the 532 nm beam, the GRIIRA signal rapidly increased before it started decreasing. Then, secondly, after switching off the green light, the GRIIRA signal again first increased quickly and almost reached the maximum absorption value and, then, the familiar exponential relaxation set in again. The cycle could be repeated many times with the same qualitative GRIIRA behaviour. The effect was observed in all as-poled PPKTP samples.

We tentatively attribute the special overshoot features to the presence of remnant stress in the as-poled PPKTP. The built-in piezoelectric field due to the stress could be compensated for in the PPKTP, and most probably, this is achieved by a net displacement of K_i^+ and $V(K^+)$. This displacement will have the same effect on the induced absorption as the ion displacement caused by the compensation of the depolarization field during the poling, i.e., by stabilizing electron and hole traps and, thus, increasing the concentration of the induced colour centres. Recharging those centres with the captured charge carriers should produce transient electric fields, which would induce a phase distortion of the probe beam via the electro-optic effect.

An interesting observation was that, upon annealing the as-poled crystals (PPKTP) in air at a temperature of 200 ºC for one hour, the peculiar dynamic features showed in Fig. 7.6 were completely eliminated. The samples again displayed the conventional dynamics as seen in Fig. 7.5, but with a peak induced-absorption of about 50 % lower level than the peak observed in the as-poled samples.

7.3.2.4. Measurement of small absorption from QPM SHG

The GRIIRA set-up allows for simultaneous and sensitive absorption measurements to be performed in PPKTP with two separate wavelengths. It would be of particular interest to measure the absorption at the phasematching condition. To do that, we studied continuous wave blue light of 473 nm, generated by quasi-phasematched frequency doubling in a 17 mm long PPKTP sample with a domain periodicity of 6.09 µm. By measuring the signal of the thermal lens dependencies on the near-infrared pump power for the infrared wavelength being tuned to the phasematching, and then, away from it again, then, by subtracting and properly normalizing those dependencies as described in Section 7.3.2.2, we have obtained the dependence of the absorption coefficient on the near infrared power as shown in Fig. 7.7.

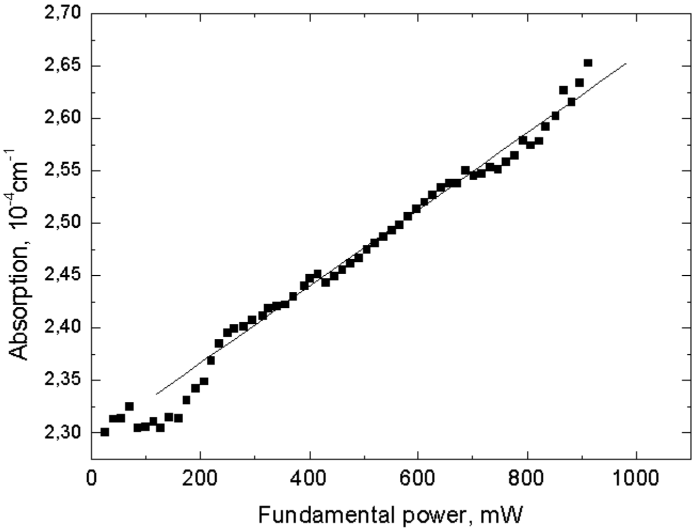

Fig. 7.7 The growth of the absorption with the fundamental power in PPKTP used for quasi-phasematched, second-harmonic generation at 473 nm.

The observed dependence, in fact, represents both the near-infrared absorption and the generated blue-light absorption in the same beam channel, therefore, the apparent dependence can be expressed as follows:

$$\alpha(P_{IR}) \approx \alpha_{NIR} + 0.5\alpha_{SH}\eta L_{KTP} P_{IR} \tag{7-7}$$

where the subscripts NIR and SH designate the near-infrared and the second-harmonic, respectively, P_{IR} is the infrared power, and η is the second-harmonic generation efficiency in units of $W^{-1}cm^{-1}$. The linear growth of the absorption with the infrared power seen in Fig. 7.7 arises from the absorption of the second-harmonic wave and this dependence can be used to estimate the small-signal absorption at the second-harmonic wavelength. With 900 mW of the near-infrared pump power, the PPKTP crystal generated 8.8 mW of second-harmonic power which gives a conversion efficiency of $\eta = 0.64 \times 10^{-2}$ $W^{-1}cm^{-1}$. From Eq (7-7), the small-signal absorption coefficient is found to be $\alpha_{SH} = 1.2 \times 10^{-2}$ cm^{-1} at 473 nm.

7.4. Material breakdown

In many cases, the nonlinear devices were pumped at high intensity in order to obtain high conversion efficiency. However, the risk of material breakdown increases with increasing the pump intensity, particularly for high-intensity, visible light generation. In general, the mechanism which will cause damage is dependent on the wavelength, the peak intensity, the pulse length and the thermal loading of the crystal. For high-energy, ns-long visible pulses, the absorbed energy is large enough to lead to an increasing thermal loading in the QPM structure, which can result in thermal gradients and phase-mismatch, as well as a thermal shock. For mode-locked, high-average power visible ps pulse trains, although the pulse energy may be relative low compared to the ns pulses, still, the thermal gradients can cause severe stress, and will eventually lead to catastrophic damage.

The damage thresholds of PPKTP materials were measured during frequency doubling at the condition of phasematching, with the single-pass SHG set-up shown in Fig. 4.4, and by increasing the fundamental power very carefully. Several pump lasers, with different operating parameters, were used in our investigation. The highest fundamental peak intensity and the type of the damage observed in PPKTP are summarized in Table 7.2.

Laser	**Parameters of the fundamental beam**			**Fundamental Peak intensity** (MW/cm^2)	**Type of damage**
	Wavelength (nm)	**Pulse length**	**Repetition rate**		
Nd:YAG	1064	5 ns	Single pulse	800	None
Nd:YAG	1064	5 ns	20 Hz	700	None
Nd:YAG	1064	100 ps	100 MHz	31	Scattering
Nd:YAG	1064	220 ns	1.2 kHz	71	Breakdown
Nd: YLF[28]	1053	80 ns	5 kHz	52.5	Breakdown
Nd: YLF[28]	1053	120 ns	8 kHz	29.9	Breakdown
Nd: YLF[28]	1053	150 ns	10 kHz	24.5	Breakdown
Nd: YLF[28]	1053	220 ns	15 kHz	16.4	Breakdown

Table 7.2 The highest peak intensity and other relevant parameters used in the damage threshold measurements during frequency doubling at phasematching.

Fig. 7.8 shows the damage morphology at breakdown in a PPKTP crystal at phasematching during green-light generation with a fundamental intensity of 71 MW/cm^2 using 220 ns pulses at 1064 nm[29]. The beam was impinging from the left and formed a filament. The damage propagates to the right, in the end, it creates a larger circular damage area probably due to a thermal shock.

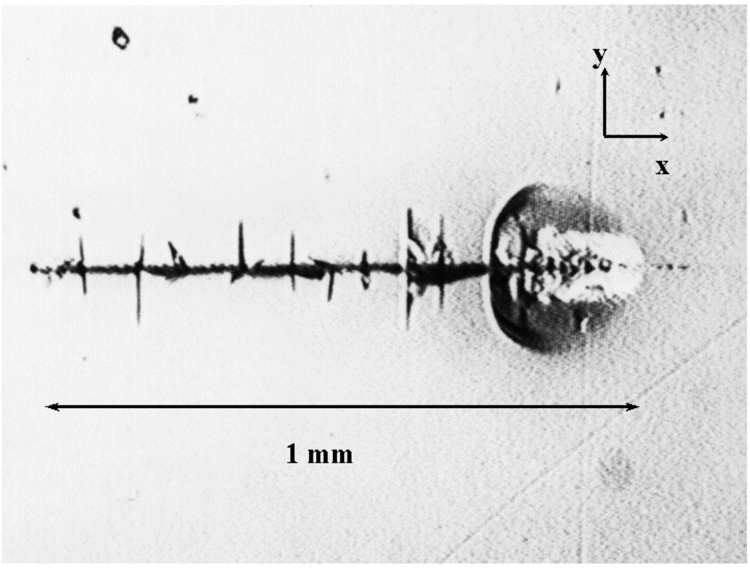

Fig. 7.8. Bulk damage on a flux-grown PPKTP crystal pumped by a Q-switched Nd:YAG laser with 1.2 kHz repetition rate and a 220 ns pulse length.

To determine the dependence of the damage threshold on the laser repetition rate for ns-long pulses, I have analysed the fundamental peak intensities of a Nd:YLF laser experiment where the damages occurred in KTP. Fig. 7.9 displays that the damage threshold decreases exponentially with the repetition rate. The full line is an exponential fit to the observation.

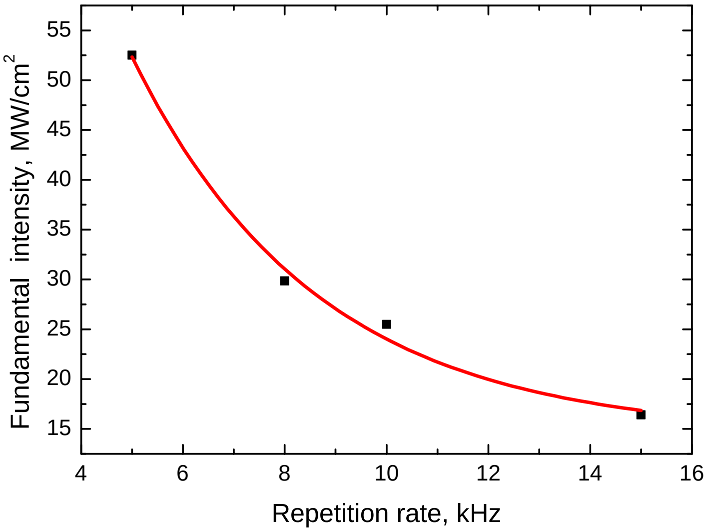

Fig. 7.9 The fundamental intensity for breaking down the material decreases exponentially with the repetition rate of the ns pump laser. The full line is a single exponential fit.

References of Chapter 7

[1] A. Ashkin, G. D. Boyd, J. M. Dziedzik, R. G. Smith, A. A. Ballman, J. J. Levinstein and K. Nassau, Appl. Phys. Lett. **9**, 72 (1966).

[2] G. W. Ross, M. Pollnau, P. G. R. Smith, W. A. Clarkson, P. E. Britton and D. C. Hanna, Opt. Lett. **23**, 171 (1998).

[3] G. A. Magel, M. M. Fejer, R. L. Byer, Appl. Phys. Lett. **56**, 108 (1990).

[4] V. Pruneri, P. G. Kazansky, J. Webjörn, P. St. J. Russell, D. C. Hanna, Appl. Phys. Lett. **67**, 1957 (1995).

[5] M. Taya, M. C. Bashaw and M. M. Fejer, Opt. Lett. **21**, 857 (1996).

[6] P. A. Champert, S. V. Popov and J. R. Taylor, Electron. Lett. **37**, 1127 (2001).

[7] P. A. Champert, S. V. Popov and J. R. Taylor, Appl. Phys. Lett. **78**, 2420 (2001).

[8] M. Tsunekane, N. Tachuch1, and H. Inaba, Opt. Lett. **22**, 1000 (1997).

[9] J. K. Tyminski, J. Appl. Phys. **70**, 5570 (1991).

[10] J. C. Jacco, D. R. Rockafello and E. A. Teppo, Opt. Lett. **16**, 1307 (1991).

[11] G. M. Loiacono, D. N. Loiacono, T. McGee, M. Babb, J. Appl. Phys. **72**, 2705 (1992).

[12] R. Blachman, P. F. Bordui and M. M. Fejer, Appl. Phys. Lett. **64**, 1318 (1994).

[13] B. Boulanger, I. Rousseau, J. P. Fève, M. Maglione, B. Ménaert, and G. Marnier, IEEE J. Quantum Electron. **35**, 281 (1999).

[14] J. P. Feve, B. Boulanger, G. Marnier and H. Albrecht, Appl. Phys. Lett. **70**, 1 (1997).

[15] W. R. Boserberg and D. R. Guyer, Appl. Phys. Lett. **61**, 387 (1992).

[16] V. N. Voitsekhovii, V. E. Yakobson, A. G. Kalintsev and S. V. Kaminskii, J. Opt. Technol. **62**, 777 (1995).

[17] M. J. Martin, C. Zaldo, F. Diaz, R. Sole, D. Bravo and F. J. Lopez, Radiat. Eff. Defects Solids **136**, 243 (1995).

[18] M. P. Scripsick, D. N. Lolacono, J. Rotterberg, S. H. Goellner, L. E. Halliburton and F. K. Hopkins, Appl. Phys. Lett. **66**, 3428 (1995).

[19] G. J. Edwards, M. P. Scripsick and L. E. Halliburton, Phys. Rev. B**48**, 6884 (1993).

[20] V. Mürk, V. Denks, A. Dudelzak, P.-P. Proulx, and V. Vassilitsenko, Nuclear Instrum. Methods. Phys. Res. B**141**, 472 (1998).

[21] A. Alexandrovski, M. M. Fejer, G. Mitchell, Post Conference Edition. CLEO '99. Conference on Lasers and Electro-Optics (IEEE Cat. No.99CH37013), 531 (1999).

[22] B. Boulanger, M. M. Fejer, R. Blachman and P. F. Bordui, Appl Phys. Lett. **65**, 2401 (1994).

[23] A. Marcano, O. C. Loper, and N. Melikechi, Appl. Phys. Lett. **78**, 3415 (2001).

[24] M. Roth, N. Angert, M. Tseitlin, and A. Alexandrovski, Optical Mater. **16**, 131 (2001).

[25] http://www.casix.com/product/NLO_KTP.htm.

[26] M. E. Innocenzi, H. T. Yura, C. L. Fincher, and R. A. Fields, Appl. Phys. Lett. **56**, 1831 (1990).

[27] V. Pasiskevicius, A. Fragemann, F. Laurell, R. Butkus, V. Smilgevicius, and A. Piskarskas, Appl. Phys. Lett. **82**, 325 (2003).

[28] Unpublished data from my experiment.

[29] S. Wang, Licentiate Thesis, TRITA-FYS 2185, ISSN 0280-316X, (1999).

8. Description of included papers and the contribution by the candidate

Paper I: Efficient Nd:YAG laser frequency doubling with periodically poled KTP

V. Pasiskevicius, S. Wang, J. A. Tellefsen, F. Laurell and H. Karlsson

Frequency doubling of low and medium-power Nd:YAG lasers via the quasi-phasematching technique provides the possibility of obtaining compact, all-solid-state green laser sources. The purpose of this paper was to demonstrate high-efficiency, extra-cavity frequency doublers based on PPKTP, with different types of Nd:YAG lasers. In this paper, firstly, the QPM crystal fabrication technique was introduced. The periodicity of the grating was chosen so as to phasematch the second-harmonic generation employing the d_{33} nonlinear coefficient at a fundamental wavelength of 1064 nm. 1.34 W of average SH power was generated from 2.2 W of mode-locked 100 ps pulses, while a conversion efficiency of 65 % was obtained in Q-switched operation for 220 ns pulses at a 1.2 kHz repetition rate. As a comparison, only 38% was obtained using conventional birefringence, type-II phasematched KTP. The calculations showed that, at high fundamental intensity, the fundamental power depletion is not the only factor that saturates the conversion efficiency, but, also, a thermally-induced phase-mismatch plays an important role.

Contribution by the candidate: I fabricated the PPKTP crystals, participated in designing and performing the experiment and in the calculation, discussion and writing of the paper.

Paper II: Ultraviolet generation by first-order frequency doubling in periodically poled $KTiOPO_4$

S. Wang, V. Pasiskevicius, F. Laurell and H. Karlsson

The purpose of this paper was to demonstrate the generation of UV light by frequency doubling in PPKTP. A 2.95 μm-period, first-order QPM grating was fabricated using standard lithography and electric-field poling techniques for frequency-doubling of 780 nm fundamental light, employing the largest nonlinear coefficient, d_{33}. With 270 mW of CW incident fundamental power from a Ti:Sapphire laser, 450 μW of UV power was generated in a single-pass configuration. Frequency doubling of short pulses was also investigated in order to explore the applicability of PPKTP with femtosecond lasers. For more than six years, this was the finest-pitch grating fabricated in a 1 mm-thick ferroelectric crystal.

Contribution by the candidate: I fabricated the PPKTP crystal, participated in designing and performing the experiment, in the calculations, discussions and writing of the paper.

Paper III: First-order type II quasi-phase-matched UV generation in periodically poled KTP

S. Wang, V. Pasiskevicius, J. Hellström, F. Laurell and H. Karlsson

One of the main hindrance for quasi-phasematched UV-radiation generation is the difficulty to fabricate first-order QPM gratings, due to the large material dispersion and the very short period thereby required. In this work, we investigated type-II quasi-phasematched second-harmonic generation for the first time. We relied on the material PPKTP and used the d_{24} nonlinear coefficient. By the use of a type-II interaction, instead of a type-I, a 3 times longer grating pitch could be used. 440 µW of UV-radiation was generated from 780 mW of fundamental power, corresponding to a normalized conversion efficiency of 0.09 %/W·cm.

Contribution by the candidate: I fabricated the PPKTP samples, performed the experiment, and participated in the calculation, the discussion and writing of the paper.

Paper IV: Three-dimensional characterization of the effective second-order nonlinearity in periodically poled crystals

S. J. Holmgren, V. Pasiskevicius, S. Wang and F. Laurell

The effective nonlinearity of periodically-poled crystals can vary over the volume of the QPM structure due to material and poling nonuniformities. The purpose of this work was to demonstrate a novel technique to map the effective nonlinearity in 3D. It utilizes group-velocity walk-off between femtosecond pulses at the fundamental frequency in a type-II SHG configuration to achieve three-dimensional resolution of the effective nonlinearity. The technique is especially useful for characterizing quasi-phasematched nonlinear crystals, having a sophisticated grating structure.

Contribution by the candidate: I fabricated the PPKTP sample, participated in the experiment and the discussions related to the paper writing.

Paper V: Dynamics of green light-induced infrared absorption in $KTiOPO_4$ and periodically poled $KTiOPO_4$

S. Wang, V. Pasiskevicius and F. Laurell

For this work, we built a high-sensitivity, induced thermal-lens spectroscopic instrument with a common-path interferometer to investigate the green-light induced absorption dynamics in single-domain and periodically-poled $KTiOPO_4$. The experimental results showed that the absorption by the induced colour centers is more severe in the poled material although the linear infrared absorption in both materials is the same. Initial relaxation of the induced absorption was also different in these materials indicating that the poled structures contain higher concentration of stoichiometric or interstitial defects. It is shown that an annealing step after poling can improve the quality of the crystal, in terms of a reduction of the amplitude of the induced absorption, as well as the eliminating stress in the domain walls. The sensitivity of the technique is demonstrated by the measurement of the small-signal absorption in the blue spectral region arising during continuous wave quasi-phasematched second-harmonic generation in periodically poled KTP.

Contribution by the candidate: I fabricated the PPKTP samples, performed the experiment, and participated in the discussion and the writing of the paper.

Paper VI: Nucleation and growth of periodic domains during electric field poling in flux-grown $KTiOPO_4$ observed by atomic force microscopy

C. Canalias, S. Wang, V. Pasiskevicius and F. Laurell

In order to get a deeper understanding of the mechanisms of the domain nucleation and growth in flux-grown KTP during electric-field poling, we have studied the domain structure of PPKTP on both the polar and nonpolar faces utilizing AFM. Distinct characteristics of the poling behaviours, depending on the magnitude of the applied electric field, have been identified.

Contribution by the candidate: I participated in the AFM measurements, as well as in discussion and the writing of the paper.

Paper VII: High efficiency periodically poled Rb-doped $KTiOPO_4$ using in-situ monitoring

S. Wang, V. Pasiskevicius and F. Laurell

Flux-grown KTP has a relatively high ionic conductivity and a substantial variability of the conductivity over the wafer, which significantly complicates electric-field periodic poling. In this work, we investigated flux-grown Rb-doped KTP (RKTP), which has almost 2 orders of magnitude lower ionic conductivity than undoped KTP crystals. This material proved to be a good candidate for periodic poling and high quality PPRKTP crystals for second-harmonic generation and optical parametric oscillation were demonstrated. The polarization was periodically switched at room-temperature with a coercive field of 3.4 kV, which is 50 % higher than for KTP. The dispersion and the effective nonlinearity of lightly-doped RKTP did not show any significant difference from non-doped KTP. We also demonstrated that in-situ, second-harmonic generation is a practical and useful monitoring method consistently allowing high quality periodically-poled crystals to be made.

Contribution by the candidate: I fabricated the PRKTP samples, made the measurements and participated in the discussion and the writing of the paper.

9. Conclusions

This work deals with the fabrication and the characterization of periodically-poled KTP and RKTP. In this context, there are several contributions to the field of nonlinear optical technology, namely: (1) The development of techniques for fabrication and evaluation of QPM structures have been carried out; (2) Careful investigations of the performance of second-harmonic generation frequency converters in the visible and the UV spectral ranges have been performed. Some of the potentials and the current limitations of these materials are revealed. For instance, by appropriate doping, like Rb for KTP, some of the limitations might be overcome; (3) Systematic investigations of the optical damages in KTP and PPKTP and their physical mechanisms related to high-intensity visible and UV light generation have been undertaken. The conclusions drawn from these studies are:

Although the quality of KTP wafers in terms of ionic conductivity and domain structure still remains a technological issue, our results clearly demonstrate that highly-efficient frequency converters can be fabricated from commercially available KTP material by carefully choosing the processing strategies. Particularly, in-situ SHG is a reliable monitoring method for providing real-time information of the poling process over the whole crystal aperture, resulting in high yield of efficient samples with good homogeneity.

Flux-grown RKTP is a good candidate for electric-field poling at room temperature as it has approximately two orders of magnitude lower ionic conductivity compared to undoped KTP. Furthermore, a light doping of KTP with Rb results in only a minor change of the material dispersion and the effective nonlinear coefficients in PPRKTP are approximately the same as for PPKTP.

The characterization techniques we have developed, have allowed us to obtain information regarding the QPM homogeneity, the local periodicity and the local effective nonlinearity of the structures, which are the most important parameters for successful device applications of these engineered ferroelectrics.

We have been able to fabricate very dense domain gratings in PPKTP ($\Lambda < 3$ μm) in 1 mm thick sample for first-order frequency doubling down to the UV region where the fundamental absorption edge of KTP is located. SHG efficiency as high as 74% has been obtained for green-light generation, which is probably the highest one for PPKTP at present. Type-II phasematching has been demonstrated in PPKTP with relaxed fabrication requirements for generation of blue/UV radiation by taking advantage of the lower dispersion for this polarization arrangement. Although the nonlinear coefficient in type-II interactions is lower than that in the corresponding type-I case, the higher grating reproducibility of the QPM structure and the broader wavelength acceptance bandwidth can often compensate for these shortcomings in many cases. Moreover, the type-II QPM process can be advantageous for nonlinear interactions with short pulses, where the lower effective nonlinearity is not as critically important as in CW case.

High-sensitivity, thermal-lens spectroscopy proved to be a very useful technique for quantifying the infrared absorption present in our nonlinear optical materials brought about by excitation by intense green light. The saturated green-light-induced infrared absorption was consistently larger in the periodically-poled crystals, which was attributed to an increase in the concentration of the native defects, hence, more possibilities for colour-center formation in the PP materials. Subsequent annealing process reduced the amplitude of the induced absorption and should be considered as a necessary post-poling processing step.

High-intensity, visible-light generation, leading to the observed induced colour-center formation and associated absorption provides an increased thermal loading in the QPM structure material, resulting in unwanted temperature gradients and phase-mismatch. Moreover, the thermal load introduces stress, eventually producing catastrophic damage in the end. This thermally-induced damage mechanism is very important for ns high-energy, visible and UV laser pulses, as well as for high-repetition rate pulse trains down to at least 100 ps.

Future work along the lines in the present thesis should be focused on investigating the absorption dynamics of RKTP and PPRKTP as well as the influence of the doping rate on the electric-field poling.

Acknowledgements

This work has been funded by generous grants from Carl Tryggers Stiftelse, Göran Gustafssons Stiftelse and Vetetenskapsrådet and has been carried out in the Division of Laser Physics, Department of Physics at the Royal Institute of Technology (KTH). I wish to express my sincere gratitude to all the people that have helped me during my Ph.D. studies and in the writing of this thesis in one way or another. In particular, I would like to thank:

Professor Fredrik Laurell, my supervisor, for introducing me to the field of nonlinear optics, for your excellent scientific guidance and never-ending enthusiasm and confidence in my work. You have shared with me your knowledge and your thoughts, not only on research, but also on the daily life. Thank you also for creating such a great group for any student to grow up as a scientist and as a person.

Docent Valdas Pasiskevicius, for always being there for me, for extraordinary enthusiasm and full of great ideas on how to make my research better and better and improving the manuscripts. It is always a pleasure to have interesting scientific discussion with you because you have such great knowledge in the field of nonlinear optics, and you have the unique ability to simplify things, making them logical, and at the end of the day, this look "easy".

Professor Dwayne Miller, at the University of Toronto, for providing me with a wonderful stay in your group to accomplish the experiments for this thesis. I would also like to thank **Dr. Yan Liao** and **Dr. Jiaren Liu,** for introducing me to thin-disk, high-power lasers and to have shared with me your vast knowledge in laser physics.

Associate professor emeritus Jens A. Tellefsen, for constant enthusiasm of my work, for helping me to correct the grammatical errors of this thesis in your spare time, and I appreciate this very much.

Other members of Fredrik's group: **Carlota Canalias**, **Stefan Holmgren**, not only for the fruitful collaborations, but also for nice discussions on how to make a better style for the thesis; **Junji Hirohashi**, for sharing your knowledge in nonlinear optical material; **Anna Fragemann, Mikael Tiihonen**, my office-mates, for sharing the office and nice chats; **Jonas Hellström** and **Pär Jelger,** for solving computer problems; and the rest of the group, for the fun we have had together.

Agneta Falk, for always being helpful and all kinds of assistance. **Rune Persson** for excellent technical assistance.

It was not easy to always deliver the PPKTP crystals in time, a key component for Cobolt's laser production and to work on the Ph.D. thesis, simultaneously. Fortunately, a good team at Cobolt made my tasks fulfilled without too much difficulty. Thank you **all my colleagues at Cobolt**.

All my Chinese friends in Sweden, in Canada, and in China, for your friendship and sharing the good times together.

My family in China, for your love and encouragement, for all your support and help over the years.

My husband Zhenlei, thank you for all your love, understanding, supporting and care. It has been a long journey since I started my Ph.D. program and I would not have made it through without you. I also want to thank our lovely son, **Daniel**, for bringing me enormous joys and for reminding me that there still are things in life, which are even much more important than KTP and domain engineering.